University of California

Los Angeles

Optimization of muon timing and searches for heavy long-lived charged particles with the Compact Muon Solenoid detector at the Large Hadron Collider

A dissertation submitted in partial satisfaction
of the requirements for the degree
Doctor of Philosophy in Physics and Astronomy

by

Christopher Patrick Farrell

2013

The dissertation of Christopher Patrick Farrell is approved.

_____

Peter Felker

_____

Michael Gutperle

_____

David Saltzberg

_____

Jay Hauser, Committee Chair

University of California, Los Angeles

2013

To my parents who have always been supportive of me

TABLE OF CONTENTS

List of Figures

Acknowledgments

 I want to say thank you to my advisor Jay Hauser whose teaching and advice allowed me to grow into a contributing member of the scientific community. Jay has always been available to aid in my understanding of problems and to give ideas when I was unsure of what to do going forward. I could not have completed this work without him.

My development as a physicist has been shaped by discussions and guidance by my colleagues on CMS. The list includes but is not limited to Greg Rakness, Amanda Deisher, Mikhael Ignatenko, Chad Jarvis, Loic Quertenmont, and Todd Adams.

I am also grateful to David Saltzberg, Michael Gutperle, and Peter Felker for being willing to be on my committee and review my dissertation.

Finally I want to thank my family for their constant support. Especially, I want to thank my parents who have always worked to make my life as happy and fulfilling as possible.

<div align="center">Vita</div>

1985   Born, New Jersey, USA.

2008   B.S. Physics, University of Florida.

2008–present   Research Assistant, University of California, Los Angeles.

<div align="center">PUBLICATIONS</div>

S. Chatrchyan *et al.* [CMS Collaboration], "Search for heavy long-lived charged particles in *pp* collisions at $\sqrt{s} = 7$ TeV." *Phys.Lett.*, B713:408–433, 2012.

The CMS Collaboration. "Performance of CMS muon reconstruction in pp collision events at $\sqrt{s} = 7$ TeV." *Journal of Instrumentation*, 7:2P, October 2012.

Abstract of the Dissertation

Optimization of muon timing and searches for heavy long-lived charged particles with the Compact Muon Solenoid detector at the Large Hadron Collider

by

Christopher Patrick Farrell

Doctor of Philosophy in Physics and Astronomy

University of California, Los Angeles, 2013

Professor Jay Hauser, Chair

Proton–proton collisions at the Large Hadron Collider at $\sqrt{s} = 7$ and 8 TeV are studied using the Compact Muon Solenoid (CMS) detector. The measurement and improvements to the arrival time of particles to the muon system of CMS is detailed. The timing is used to associate the particle with the correct proton–proton crossing and to classify the particle. Additionally, four analyses are presented that use timing and ionization energy loss to search for the production of long-lived charged particles predicted in many theories of new physics. The searches are sensitive to a variety of signatures, including the possibility that the particles will only be detectable during part of their passage through the CMS detector. Limits are placed on the production of long-lived gluinos, stops, staus, and multiply charged particles. The limits are the most stringent in the world to date.

CHAPTER 1

Introduction

Particle physics is concerned with studying what matter is made of and how it interacts at a fundamental level. The desire to understand nature at its most basic level has long been of interest to humankind, dating back to at least the ancient Greek philosophers. The field of particle physics began to come into its own beginning with the discovery of the electron in 1897 by J.J. Thompson [1]. In the more than a century since that discovery, the field has been revolutionized many times. Whenever it seemed that the final piece of the puzzle was within reach, a surprising result would be found: fundamental particles shown to be composites, inviolate symmetries found to be broken, or a universe with accelerating expansion.

The current state of knowledge in particle physics is contained in the standard model (SM) of particle physics. The SM contains all of the known particles and the way that they interact with one another. The SM has been developed over the last forty years and has proven to be a very successful theory. Numerous experiments have validated the theory with the discovery of predicted particles or agreement of parameter values.

The last particle to be found that is predicted by the SM is the Higgs Boson. The discovery of the Higgs Boson is one of the reasons the Large Hadron Collider (LHC) was built outside of Geneva, Switzerland. The LHC collides protons at an energy higher than any previous experiment at an extremely high rate [2]

producing many particles in the collisions. Surrounding the points where the LHC brings the protons to a collision are experiments designed to measure and reconstruct the particles emanating from the collisions. Two of these experiments, CMS and ATLAS, announced in June of 2012 the discovery of a new particle with properties like that of the SM Higgs Boson [3, 4].

Throughout the history of particle physics, just when the theory looks to be the most stable can be when a discovery revolutionizes the field. There are many models which predict physics beyond the SM [5, 6] that would be produced by the LHC and could be detected by the LHC experiments. One of the most popular models is supersymmetry (SUSY) where all of the SM particles are given a superpartner with spin different by one half. Some of these models predict the production of new heavy (meta-)stable charged particles (HSCP) which would directly interact with the LHC experiments. All of the long-lived SM particles produced by the LHC have a small mass, meaning that a discovery of an HSCP would be a clear indication that a new theory must be developed to explain these particles.

There are numerous different types of HSCP predicted in the models of new physics, and the different types can leave exotic signatures in the LHC detectors. Some types of HSCPs would form composite objects with SM particles and undergo nuclear interactions with the detector material that change the SM particles in the composite particles. This could lead to the HSCP changing its electric charge during its propagation through the detector. Other HSCP could be produced with electric charge not equal to e, the charge of an electron, unlike almost all electrically charged particles expected to be produced at the LHC.

Multiple complementary searches for HSCP produced at the LHC were carried out using data collected by the CMS experiment and are presented in this work.

Each of the searches is designed to be sensitive to different signatures that HSCP could have in CMS but many of the tools and techniques used are common between searches. The searches exploit the experimental signatures of HSCP that allow them to be separated from the very large background of SM particles. Requirements are placed on these characteristics and the residual background due to SM particles is evaluated. The data are then checked to see whether the observation is consistent with this background. If it is not consistent, then this indicates the presence of a new particle beyond the SM while if it is consistent then this places limits on models of physics beyond the SM.

HSCP produced at the LHC are expected to have high momentum, likely more than 100 GeV/c. Even at this high momentum, HSCP would be traveling at a speed appreciably slower than the speed of light due to their large mass. All of the long-lived SM particles produced at the LHC would be traveling at very nearly the speed of light, c, even at a momentum of 10 GeV/c. The slow speed of the HSCP means that it would arrive to the outer portion of CMS later than SM particles would. To observe this, it must be possible to measure the arrival time of hits in the outer portions of CMS. This time measurement is important not only for HSCP but also for SM particles to associate them with the correct LHC beam collision and to separate out SM particles not coming from LHC collisions, such as from cosmic rays.

Chapter 2 of this work discusses the SM and a few models of physics beyond the SM. An emphasis is placed on theories which include new long-lived charged particles. In Chapter 3, the experimental apparatus used in this work is presented. This includes the LHC and CMS, in particular parts of the apparatus especially important for searches for long-lived charged particles are given extra detail. Chapter 4 discusses the measurement of the arrival time of hits in the outer

portion of CMS. Chapter 5 details four complementary searches for new heavy long-lived charged particles. Concluding remarks on the presented work are given in Chapter 6.

CHAPTER 2

Relevant Theoretical Issues

2.1   Introduction

Our understanding of particles and how they interact is constantly evolving through new experimental results and theoretical breakthroughs. In this chapter, the current theoretical framework in particle physics is briefly described. Also, theories of physics beyond this framework are introduced, with a focus on theories which predict the existence of new long-lived charged particles.

2.2   Standard Model

The Standard Model (SM) of particle physics is a framework for describing fundamental and composite particles and the forces that govern how they interact. More information about the Standard Model can be found in [1, 7].

Particles in the SM are split into two types: bosons, which have integer spin, and fermions, which have half integer spin. The bosons are the carriers of the forces of the SM while the fermions act as the matter fields.

Formally, the SM is described according to the symmetry group

$$SU(3)_C \times SU(2)_L \times U(1)_Y \qquad (2.1)$$

where SU(N) denotes special unitary groups of dimension N. Reading from left

to right the groups represent color, weak isospin, and hypercharge. The color symmetry group is responsible for the strong force which is carried by the gluon. A mixture of the weak isospin and hypercharge groups are responsible for the weak and electromagnetic forces. Left-handed fermions are doublets of the isospin group while the right handed fermions are singlets as they do not interact with the raising and lowering operators of the SU(2) group. The weak force is carried by the W and Z bosons while the electromagnetic force is carried by the photon.

The last of the bosons in the SM to be discovered is the Higgs Boson. The Higgs Boson is a scalar which allows it to have a non-zero vacuum expectation value (VEV). This non-zero VEV breaks the electroweak symmetry and results in the W and Z bosons acquiring mass while the photon remains massless. The Higgs Boson's non-zero VEV also gives mass to the fermions by allowing for a coupling between the singlet right handed fermions and doublet left handed fermions which is otherwise not allowed. In July 2012, the CMS and ATLAS experiments at the Large Hadron Collider (see Ch. 3) announced the discovery of a new particle with properties similar to the Higgs Boson [8, 4].

The fermions in the standard model are split between quarks and leptons. Both the quarks and leptons are arranged into three families, with each family containing two quarks and two leptons. The first family contains the up and down quarks, the electron, and the electron neutrino. The second family has the strange and charm quarks, the muon, and the muon neutrino. The third family contains the bottom and top quarks, the tau, and the tau neutrino. The down, strange, and bottom quarks have charge -1e/3 while the up, charm, and top quarks have charge +2e/3. The electron, muon, and tau have charge -1e, and all of the neutrinos are electrically neutral. All of the electrically charged particles in the SM have an antiparticle with the opposite charge.

The quarks and gluons have color charge and interact through the strong force. There are three copies of each quark for each of the three different color charges. The strength of the strong force increases with distance leading to color confinement where no free particles can exist with color charge. Thus all quarks and gluons will form composite particles that are color neutral, called hadrons. There are two types of hadrons that have experimentally observed. The first is a quark and an anti-quark referred to as mesons such as a charged pion which is made of an up quark and and down antiquark. The second is three quarks (or anti-quarks) referred to as baryons and includes the proton and neutron. Mesons and baryons can be either electrically charged or neutral. Other combinations of quarks and gluons would be color neutral but have not been observed in nature. One example is a pair of gluons that would always be electrically neutral.

When quarks and gluons are produced at high energies, the binding of the strong force normally results in numerous secondary quarks and antiquarks being produced. These quarks and antiquarks will then form hadrons in a process called hadronization. All of the hadrons will be traveling in roughly the same direction resulting in a stream of collinear particles from the production point. This beam of particles is referred to as a jet.

Most SM particles produced at the LHC, both fundamental and composite, have very short lifetimes preventing them from being directly detected. The only stable SM particles at the LHC are the electron, proton, photon, and the neutrinos. Additionally, a free neutron has a lifetime of eight minutes but it may be stable inside a nucleus. A few other particles have lifetimes long enough to be detected before decaying including the muon, pion, and kaon.

The proton-proton collisions at the LHC will create vast numbers of these SM particles. As the strong force has the largest coupling, a large majority of the

events will be the production of light quarks and gluons. A small fraction of the events (though a large total number given the very high rate of collisions at the LHC) will produce particles such as W and Z bosons, top quarks, and the Higgs Boson. These particles will quickly decay into other SM particles like muons, electrons, and b quarks. This production of stable and long lived SM particles, particularly muons, form part of the background for the search for HSCP detailed in Chapter 5.

The production of SM particles proceeds not only in the proton-proton collisions at the LHC but also through astrophysical processes. The earth is constantly being bombarded with high-momentum protons from astronomical sources. These protons interact with the earth's atmosphere predominantly resulting in the production of numerous charged and neutral pions. Charged pions will then decay into high momentum muons. As the muons will have a large relativistic boost, they will be able to reach the earth before decaying. Muons lose only a small amount of energy in interactions with matter, allowing the highest-energy cosmic-ray muons to penetrate through large amounts of earth. This allows cosmic-ray muons to pass through CMS potentially creating a background for searches for new physics.

2.3 Beyond Standard Model Theories and Heavy Stable Charged Particles

More information about theories beyond the SM and heavy stable charged particles can be found in [5, 6, 9].

While the SM has proven to be a very robust theory, there are reasons to believe it is not complete. These include runaway radiative corrections to the

Higgs mass and an inability to explain the astronomically observed dark matter. At a minimum, the theory must be replaced at the Planck energy scale (10^{18} GeV) where the gravitational force becomes as strong as the other forces. To address issues like these numerous theories have been put forth for physics beyond the SM (BSM). If these BSM theories are accurate, evidence of them could very well be present in the high energy collisions produced at the LHC. Some of these BSM theories predict the existence of heavy meta-stable charged particles (HSCP) with lifetimes greater than a few nanoseconds, long enough to traverse the length of typical particle detectors.

One of the most popular BSM theories is supersymmetry (SUSY). A new symmetry is added that gives each SM particle a superpartner particle with spin different by one half. The SUSY particles interact with the same coupling as their SM particles. The names of the SUSY particles are generally found by prepending an s (for scalar) to the SUSY partners of spin 1/2 particles; so the SUSY partner of the electron is the selectron. The names of other particles is found by adding –ino to the end of their names, so the higgs SUSY partner is the higgsino. As no SUSY particles have yet been discovered the symmetry must be broken at some scale giving the SUSY particles masses larger than SM particles. In order to address the unresolved issues in the SM, this mass gap is expected to be no larger than about 1 TeV. In addition to adding a new symmetry, most versions of SUSY have a new multiplicatively conserved quantity called R-parity which is added to prevent rapid proton decay. SUSY particles have an R-parity value of -1 while SM particles have a value of 1. This implies that the lightest SUSY particle (LSP) will be stable and in most SUSY theories it is taken to be electrically and color neutral so as to be the astronomically observed dark matter.

Other SUSY particles besides the LSP could have a long lifetime in certain

areas of SUSY parameter space. In the minimal supersymmetric standard model (MSSM) the LSP is the neutralino (superpartner of a neutrino) in most cases. The next lightest SUSY particle (NLSP) can be long-lived if the mass splitting between the NLSP and the LSP is small. This can happen for various particles as the NLSP. For example, non-universal squark masses can be used to make the mass difference between the stop and the neutralino too small for the stop decay to a neutralino and a bottom quark to be kinematically allowed. Then the stop decay happens via the radiative decay to a charm quark and neutralino making the stop very long-lived.

Another variant of supersymmetry is split SUSY. In split SUSY, scalar SUSY particles have very large masses while other particles remain at the TeV scale. The gluino $\tilde{g}$ (superpartner of the gluon) decay through virtual squarks is suppressed by a factor of $\tilde{m}^{-2}$ allowing for the gluino to be quite long-lived.

Gluinos and stops have color charge and as such will form composite hadrons with SM quarks and gluons after production, referred to as R–hadrons. These R–hadrons can be R–mesons, R–baryons, or, for gluinos, a glueball made of a gluino and a SM gluon. R–hadrons can be electrically neutral or have charge Q, taken here and everywhere else in this paper unless otherwise stated as the absolute value of the charge, of $1e$ or $2e$, where e is the charge of the electron. For gluinos, the fraction of gluinos forming glueballs, which are always electrically neutral, is a free parameter in the theory. If the fraction is 100%, then all gluino R–hadrons will be produced electrically neutral. The mass spectrum of the R-hadrons is not well known. If there are mass gaps between the R–hadrons larger than the pion mass, the heavier R–hadron would decay to the lighter R–hadron via the weak force. It has historically been taken that all R–hadrons containing only up and down quarks are stable. Recently, theories have been put forth [10]

that only one R–baryon will be stable and the other R–baryons will decay to it. The fraction of the R–hadrons electrically charged would depend on the charge of that R–baryon.

After the R–hadrons are produced at the LHC, they will propagate out to and interact with CMS. In nuclear interactions with the detector, it is possible for the R–hadron to exchange quarks with the nucleons of the detector. This can cause the electrical charge of the R–hadron to change, possibly going from neutral to charged or from charged to neutral. Along with the electric charge, the baryon number of the R–hadron can change with R–mesons converting into R–baryons. The reverse process is unlikely to occur due to the lack of pions in the detector material and limited phase space. If the mass spectrum is as in [10], then this would result in all R–hadrons becoming the charge of the lightest R–baryon in the model after a few interactions. If this R–baryon is neutral, then essentially all R–hadrons will be neutral after passing through the calorimeter of CMS (see Sec. 3.3.1).

To cover all of the possible signatures that R–hadrons could have, two different modelings of nuclear interactions between R–hadrons and the CMS detector are considered. The first is the model presented in [11, 12] which is referred to as the cloud model and results in a mixture of charged and neutral R–hadrons after a nuclear interaction. The second model, referred to as charge-suppressed, makes all R–hadrons neutral after a nuclear interaction. This is a slightly more pessimistic model than the one discussed in [10]

A third possible type of HSCP in SUSY is the production of long-lived staus $\tilde{\tau}$ in gauge mediated symmetry breaking (GMSB) [13]. In GMSB, the gravitino is very light and almost always the LSP. GMSB models are characterized by six parameters which determine the mass hierarchy and decays of SUSY particles.

One of these parameters is the number N of SU(5) chiral multiplets added to the model which act as "messengers". As long as N is not too small the NLSP is likely to be the stau. Another one of the parameters is c_{Grav} which relates to how the SUSY breaking is transmitted to the messengers. If the communication is done perturbatively, then c_{Grav} will be very large. The large value of c_{Grav} results in the stau having a long lifetime.

Other BSM theories besides SUSY can also contain HSCPs. An interesting scenario for HSCP is the production of particles with charge not equal to $1e$. One model that includes non-unit charged HSCP is the production of particles that are neutral under $SU(3)_C$ and $SU(2)_L$ but have electric charge meaning they only couple to the photon and Z boson through $U(1)_Y$ interactions [14]. The HSCP could be produced with fractional charge ($< 1e$) or multiple charge ($> 1e$).

CHAPTER 3

Experimental Apparatus

3.1 Introduction

The apparatus used for this paper is a combination of a large particle accelerator complex and a detector used to measure the results of particle collisions. Protons are accelerated and brought to a collision by the Large Hadron Collider (LHC) located outside Geneva, Switzerland spanning the Swiss-French border. The protons are accelerated in smaller linear and cyclical accelerators before being injected into the LHC. The protons are brought to a collision at four spots along the LHC. Surrounding one of these spots is the Compact Muon Solenoid (CMS) detector. The CMS detector consists of multiple subsystems which work together to identify signatures of different types of particles.

3.2 Large Hadron Collider

A full description of the LHC can be found in [2]; a short summary is included here. The LHC is a two-ring superconducting synchrotron designed to collide particles at high energy and high luminosity. It sits in a 26.7 km tunnel located 45–170 m underneath the Swiss-French countryside outside of Geneva, Switzerland. The LHC can create collisions with either protons or heavier ions. This leads to three possible operational modes, proton-proton, ion-ion, and proton-ion.

Only in proton-proton operational mode is there a possibility to discover HSCPs and it is the only mode discussed in this paper.

The LHC was designed to accelerate protons to an energy of seven TeV and collide them at a center of mass energy($\sqrt{s}$) of fourteen TeV. The protons are brought to a collision at four points along the LHC beam line. Surrounding two of these interaction points sit the general purpose detectors of CMS and ATLAS. These detectors are designed to receive the highest instantaneous luminosity the LHC can supply of 10^{34} cm^{-2} s^{-1}. The other interaction points are surrounded by the special purpose detectors LHCb and ALICE and are designed to have instantaneous luminosities of 2×10^{29} cm^{-2} s^{-1} and 10^{27} cm^{-2} s^{-1}, respectively. This paper considers data collected by the CMS detector.

The acceleration of protons to their final energy of 7 TeV is done in series of steps employing smaller accelerators located on the CERN campus. The protons originate in the linear accelerator Linac2 which accelerates them to an energy of 50 GeV. From there, they are passed through a series of synchrotron accelerators: the Proton Synchrotron Booster, the Proton Synchrotron, and the Super Proton Synchrotron, with their energy raised to 1.4 GeV, 25 GeV, and 450 GeV, respectively. After passing through the Super Proton Synchrotron the protons are passed into the LHC. The design specification then have the LHC accelerating the protons to their final design energy of 7 TeV, however only an energy of 3.5 TeV has been achieved as yet.

The beams are designed to contain proton bunches spaced such that collisions at the interaction points occur every 25 ns. The LHC can hold a total of 2,808 bunches; in some places it is designed to have gaps larger than 25 ns between bunches to allow for dumping of the beam without harming the LHC. Each 25 ns time window is referred to as a bunch crossing window, whether there are proton

bunches colliding in CMS or not. Each collision between the proton bunches can result in more than one proton-proton collision. This results in CMS and ATLAS seeing numerous proton-proton collisions overlaid on one another. At collision, the bunches have a longitudinal length of 9 cm and radius of 20 μm [15], both numbers are RMS values. This results in the collisions in a bunch crossing being spread over a time period of a few tenths of a nanosecond.

The commissioning of the LHC saw it run at progressively higher energies building towards the design energy. In 2008, the LHC ran at $\sqrt{s} = 900$ GeV and for a short period at 2.36 TeV. Then after further work on the LHC, the center of mass energy was raised to 7 TeV for both 2010 and 2011 and then to 8 TeV in 2012. This paper only covers the data collected at 7 and 8 TeV in 2011 and 2012. It is planned to raise the center of mass energy to its design goal of 14 TeV through additional work on the LHC and the injector system.

Similarly, the instantaneous luminosity was ramped up during the commissioning phase. In 2010, the maximum instantaneous luminosity achieved [16] was 2.1×10^{32} cm^{-2} s^{-1} and in 2011 it was 3.5×10^{33} cm^{-2} s^{-1} During the 2012 running, the maximum instantaneous luminosity reached was 7.7×10^{33} cm^{-2} s^{-1}. The spacing between the collisions in CMS and ATLAS has continually between shortened down to 50 ns in 2012. It is planned to run with 25 ns bunch spacing in future LHC running.

3.3   Compact Muon Solenoid

The CMS detector is built around one of the interaction points of the LHC. A full description of CMS be found in references [17, 18].

CMS was designed to be a general purpose detector that would have sensitivity

to a wide range of physics. This is important for a search for HSCP as the detector is used in ways not typically done in most CMS analyses. The central feature of CMS is a superconducting solenoid magnet with a 6 m diameter and 13 m length that provides a 3.8 T magnetic field. The return field from the solenoid is powerful enough to saturate 1.5 m of steel, which allows for a strong magnetic field to be present outside of the solenoid. CMS has a cylindrical shape with an onion like design where inner subdetectors are nested inside of outer ones. From inside out, these subdetectors are an all silicon tracker, an electromagnetic calorimeter, a hadronic calorimeter, the magnet, and finally the muon system. Figure 3.1 shows a cross-sectional quarter view of the CMS detector. The signatures of SM particles in CMS is shown in Fig. 3.2.

CMS employs a right handed coordinate system with the x-axis pointing to the center of the LHC ring, the y-axis pointing vertically upward, and thus making the z-axis be along the beam line pointing in the counter-clockwise direction if looking at the LHC from above. The azimuthal angle, θ, is defined relative to the z-axis. The variable pseudorapidity, η, is defined as $\eta = -\ln\left[\tan\left(\theta/2\right)\right]$. The polar angle, ϕ, is defined relative to the x-axis, meaning that vertically upward (downward) has a ϕ value of $\pi/2$ $(-\pi/2)$.

The possibility that a particle containing an HSCP can interact with the detector and change its charge means that it may not have a signature like any of the particles in Fig. 3.2. The particle may be neutral after production and only gain charge as it passes through the calorimeter. The only record of its hits will be in the muon system giving the signature shown in Figure 3.3. In addition, the particle may be produced charged but then become neutral after interacting with CMS, giving the signature shown in Figure 3.4. To discover HSCP with these exotic signatures it is necessary to conduct dedicated searches. Searches of this

Figure 3.1: Cross-sectional view of a quarter of the CMS detector. Protons enter CMS along the bottom of the figure and are brought to a collision in the bottom right corner. The inner silicon tracker is in the bottom right in green. The electromagnetic calorimeter and hadronic calorimeter are outside of the silicon tracker in light gray and yellow, respectively. The muon detectors are located on the outside of the detector and are in blue.

Figure 3.2: A drawing of a cross section of CMS along with the expected interactions of SM particles as they propagate through CMS. Shown are a muon as solid line in light blue, an electron as solid line in red, a charged hadron as a solid line in green, a neutral hadron as a dashed green line, and a photon as a dashed line in dark blue.

--- HSCP (neutral in tracker)
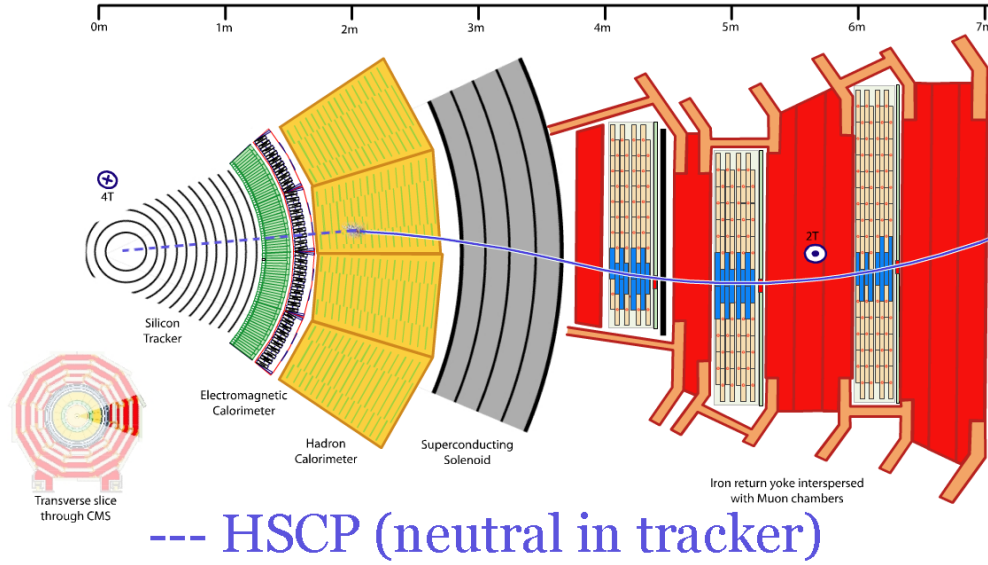
Figure 3.3: An example of an HSCP produced neutral and only becoming charged after interacting with the CMS detector. The HSCP is neutral when the line is dashed and charged when it is solid. Drawing courtesy of Loic Quertenmont.

type are presented in Chapter 5.

3.3.1 Subdetectors

The innermost part of CMS is an all silicon tracker. Closest to the interaction point are pixel detectors with three barrel layers and two endcap disks, totaling 1,440 modules. Outside of this are strip detectors with ten barrel layers and twelve endcap disks. The tracker extends up to a pseudorapidity range of 2.5 with the resolution on track p_T being approximately 1.5% for a 100 GeV/c particle at $|\eta| = 1.6$ and growing larger at high $|\eta|$ due to the decreased lever arm. Both the strips and the pixels have an analog readout of the deposited charge with a maximum readout of roughly three times the charge expected to be deposited
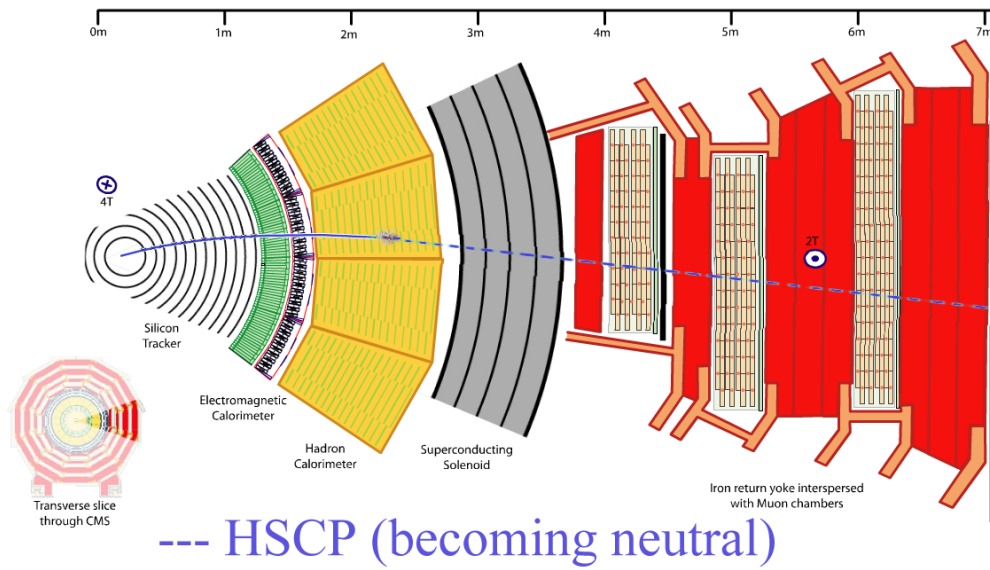
Figure 3.4: An example of an HSCP produced charged and only becoming neutral after interacting with the CMS detector. The HSCP is neutral when the line is dashed and charged when it is solid. Drawing courtesy of Loic Quertenmont.

by a muon. Charge from particles traversing the inner tracker is expected to be spread out among multiple modules in the same layer for both the pixels and the strips allowing the position of the particle to be calculated more precisely than simply the center of the module. The charge sharing also allows the possibility to identify hits where two particles have overlapped.

Outside of the inner tracker is the calorimeter. The purpose of the calorimeter is to measure the energy of particles and aid in their identification by stopping particles at different points in the calorimeter. The calorimeter is split into an inner electromagnetic calorimeter (ECAL) and an outer hadronic calorimeter (HCAL). The ECAL is made of 75,848 lead tungstate ($PbWO_4$) crystals split between the barrel and endcap. As particles lose energy in the ECAL the crystals emit scintillation light which is collected by photodetectors. The HCAL consists of plates of brass absorbers interleaved with scintillator detectors. Electrons and photons are likely to stop in the ECAL where they deposit all of their energies. Hadrons, electrically charged or neutral, will deposit some energy in the ECAL but will deposit most in the HCAL where they are very likely to come to a rest. Muons will deposit of the order of two GeV of energy in the calorimeter and are generally the only charged SM particles that are able to exit the calorimeter.

The outermost part of the detector is the muon system which is split into three parts, Cathode Strip Chambers (CSC), Drift Tubes (DT), and Resistive Plate Chambers (RPC). The CSC cover the forward part of the detector with $|\eta| > 0.9$ while the DT and the RPC cover the barrel portion extending up to $|\eta|$ of 1.2 and 1.6, respectively. The muon system is consists of four stations of chambers with the steel for the magnet return yoke located between the stations. The magnet return yoke provides a magnetic field in the muon system.

The CSC chambers have a trapezoidal shape with six layers of cathode strips

and anode wires arranged in a nearly orthogonal pattern. The strips run radially away from the beam line and measure the ϕ of hits while the wires measure the radial position of hits. The cathode strips are segmented so that charge that collects on them will be spread over multiple strips. The amount of charge on the strips is read out every 50 ns. A precise position measurement of the ϕ location of the hit can be made by charge interpolation of adjacent strips. Charge collected on the wires is passed to a constant fraction discriminator which outputs a 40 ns pulse. The pulse is sampled every 25 ns and this sampling is readout. The CSCs are laid out with four stations with increasing z from the interaction point and rings of increasing radial distance from the beam line.

The DT chambers have two or three superlayers which themselves are composed of four layers of drift cells which are staggered by half a cell. All of the DT chambers have two superlayers oriented parallel to the beam line, these superlayers measure the position of particles in the $r - \phi$ plane. The three inner stations additionally have a superlayer running perpendicular to the beam line to measure the position of particles in the $r - z$ plane.

The RPC chambers are gaseous parallel plate detectors that can provide a time resolution of 2 ns, which is much smaller than the design LHC bunch spacing of 25 ns allowing for a very high efficiency to correctly tag hits with the correct bunch crossing. The spatial resolution is sufficient to be able to associate RPC hits with hits from the other muon subdetectors.

3.3.2 Trigger and Computing

The rate of bunch crossings, or events, inside of CMS is too large for all of them to be readout and stored offline. To deal with this, CMS employs a two level trigger that selects interesting events online. The level one (L1) trigger must reduce

the rate of events readout to less than 100 kHz in less than 3.2 μs requiring a completely electronics based approach. Events are selected by a variety of algorithms but most of them look for a high momentum track in the muon system, large amount of energy in the ECAL or HCAL, or a combination of these. Signals from these systems trigger the readout of the rest of detector through the data acquisition system.

As the LHC was designed to operate with 25 ns bunch spacing, many of the subsystems, the tracker especially, only readout the data in the 25 ns window associated with the event. This means that triggers that pre- or post-fire will not contain much of the data from the event. This can be an issue for HSCP that are traveling so slowly that they reach the muon system in the time window associated with the next bunch crossing window. The muon system selects events with a high momentum track by looking for a coincidence of signals found in multiple muon stations coincident in time and consistent with the passage of a high momentum particle. A slow moving HSCP may have the signals from some stations associated with the correct bunch crossing window and others with the following one. This leads to a potential loss in efficiency to trigger events containing an HSCP due to the mismatched time windows. However, a special configuration of the RPC trigger exploits the fact that current running of the LHC has been done with at least 50ns spacing.

All hits in the RPC are sent to the trigger electronics twice, once for the bunch crossing window they are associated with and also for the one proceeding it. From there, the trigger electronics treat the time advanced RPC hits in the same manner as they do all other hits. This allows the RPCs to trigger the readout of the event preceding the arrival of the particle in the RPCs. This means that HSCP which arrive to the muon system up to 37.5ns after a muon is

expected to, could still trigger the readout of the correct data in the rest of the detector.

To ensure collision muons still maintain the correct behavior, accept signals sent for the bunch crossing window immediately preceding a bunch crossing window with protons passing through CMS are rejected. So signals from collision muons will attempt to pre-trigger but this will be vetoed and the following event will be correctly readout. This configuration is only possible when collisions are spaced by at least 50ns so that accept signals from successive 25ns bunch crossing windows can be unambiguously classified.

Once the data are readout by the data acquisition system after a L1 trigger, it is passed to a computing farm located above CMS. The next step in the trigger, the High Level Trigger (HLT), then runs on the computing farm. The HLT must reduce the number of events to a few hundred Hertz on the order of a second. The HLT is split into two different phases, Level 2 (L2), and Level 3 (L3). The L2 step is mostly concerned with confirming the L1 decision using more robust algorithms and reducing the rate so that more complex and time consuming reconstruction can be performed in the L3 step within the time restrictions. The L3 step will reconstruct tracks in the inner silicon tracker and match them to objects in other parts of the detector, such as tracks found in the muon system. The momentum resolution of tracks reconstructed in both the muon system and silicon tracker is much better than those reconstructed only in the muon system. The relative uncertainty on the momentum of muon tracks reconstructed in both systems is approximately 2% in the central region of CMS and up to 6% in the forward region [19]. For muons reconstructed only in the muon system the resolution is approximately 8% in the central region and up to 27% in the forward region. The precise tracking used in the L3 step greatly helps to identify events that

are desired for offline study. A wide variety of different signatures are searched for; if any are found, the data are passed to computers located at CERN and throughout the world for storage and further analysis.

CMS maintains a software package, CMSSW, which is responsible for taking the raw data readout from CMS and reconstructing what was happening in the event. This includes applying calibration constants, finding tracks, and identifying particles. After this reconstruction, the data size is at the scale of petabytes which is too large for offline analyzers to run over frequently. To deal with this copies of the data are produced dropping lower level quantities and selecting only events that a particular analysis is interested in studying.

CMSSW is also tasked with simulating how particles, coming from both SM processes and new physics, would interact with the detector so that this can be used to compare against data. A few steps are performed before the simulation has the same format as data readout from the detector, at that point it follows the same chain as data. The first step is the simulation of the proton-proton collision and the particles that are created from it; the detector is not used at all in this step. The simulation is done by separate event generators, such as PYTHIA or ISAJET, which then provide a list of final-state particles to be used in the next step. The simulation of how these particles will interact as they pass through CMS is handled by the GEANT. Finally the behavior of the detector electronics, including the L1 trigger, is handled by CMSSW. After this point, the simulation is handled the same as data.

CHAPTER 4

Muon System Timing

4.1   Foreword

This chapter details the measurement of the arrival time of particles in the muon system of CMS. A particular focus is put on the measurement in the CSC subsystem with a description of the measurements in the whole of the muon system given at the end.

4.2   Introduction

Particles that are produced at high momentum, greater than at least 10 GeV/c, by the LHC are of interest as they can be an indicator of physics beyond the SM. Muons have a mass of only 106 MeV/c^2 which means that even at a momentum of 10 GeV/c, muons will be traveling at a speed higher than 0.9999 times the speed of light. The difference between this speed and the speed of light is much too small to be detected by CMS, so it can be taken that all high momentum muons have the same time of flight (TOF) from their production at the center of CMS to a given point in the muon system. This time ranges from 20-40 ns depending on where in the muon system is being considered. An HSCP on the other hand, will still have a speed appreciably less than the speed of light even with a momentum of several hundred GeV/c. For example, an HSCP with a mass

of 300 GeV/c and momentum of 500 GeV/c will have a speed of 0.86 times the speed of light, an experimentally observable difference from the speed of light. Thus, a measurement of timing in the muon system can be used to separate HSCP from SM muons.

Additionally, as described in Section 3.3.2, one of the main responsibilities of the muon system is to trigger the readout of the data in the detector when a high momentum track is found. The muon system must be able to associate the tracks with a given bunch crossing to make sure the correct data are readout from CMS. The method to determine the timing synchronization of the CSC subsystem is described below.

The commissioning of the muon system timing was done during 2010 and early 2011 running at a center–of–mass energy of 7 TeV. In Chapter 5, searches for HSCP are presented which use timing measurements to identify HSCP based on data taken in 2012 at 8 TeV. To cover this whole period of time, multiple different data samples are used in this chapter. They were collected during different time periods of CMS running from 2010–2012, both before and after commissioning. All of the samples were collected by triggers looking for high momentum muons. A comparison with events collected by random sampling showed there to be no bias in the timing variables investigated due to the use of muon triggered events. The muons in the events are required to pass tight selection criteria which are determined by the Muon Physics Object Group (POG) inside of the CMS collaboration. The tight selection criteria results in a very pure collection of muons from the LHC collisions. Additionally, the muons are required to have a high momentum. The momentum threshold was continually raised from 2010–2012 due to higher trigger thresholds necessitated by the increasing instantaneous luminosity of the LHC. However the threshold was always at least 20 GeV, which

is high enough to ensure all muons are very relativistic.

4.3   CSC Hit Timing

Hits in the CSCs are found from a combination of signals from the anode wires and cathode strips. Both of the signals can be used to estimate the time of the hits.

As stated in Section 3.3.1, the charge on cathode strips is sampled every 50ns. The time of the hits is estimated with a fit to the charge distribution. Calibration constants are subtracted from the times during reconstruction to center the times at zero. The constants are found for each chamber and are derived from times associated with high-quality, high-momentum muons. Cathode times have an RMS of approximately 7.0ns.

Signals from the anode wires are passed to a constant fraction discriminator which outputs a 40ns pulse that is then digitized every 25ns. Depending on when the pulse starts, the hit can have either one or two sequential time bits being high. Given the same first high bit, it can be inferred that hits with the next bit low arrived earlier than hits with the next bit high. Hits with only one high bit are estimated to have arrived at the time of that bit while those with two high are estimated to be from the average of the two bits, i.e. 12.5 ns later. Thus, it is possible to estimate the time of anode hits with a 12.5 ns quantization. The anode times are calibrated to have a mean of zero in the same method as per the cathode times. The resolution of the anode hit timing is approximately 8.6 ns.

The distribution of the time of anode and cathode hits in data is shown in Fig 4.1. The data sample used was collected at 7 TeV center–of–mass energy after the full commissioning of the timing measurement and has a p_T threshold
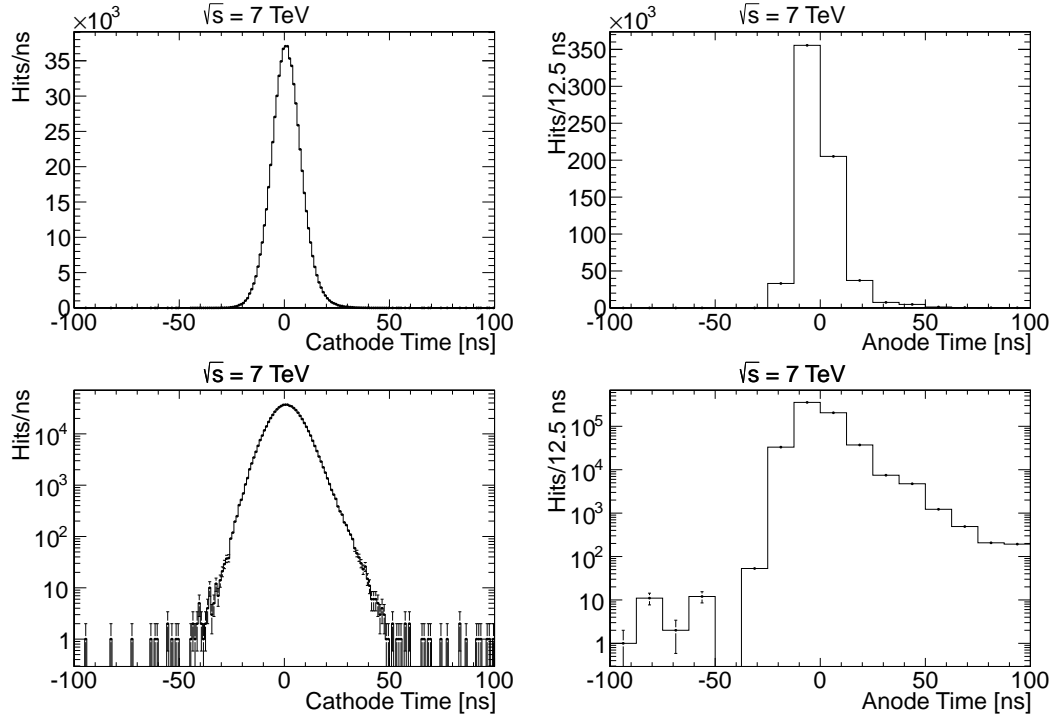
Figure 4.1: Distribution of time measured from cathode (left) and anode (right) hits. The top row shows the times with a linear y-axis scale and the bottom is with log scale.

of 20 GeV. As can be seen in the right plot the anode time has a large tail of positive times. The source of this tail is not currently well understood.

The anode and cathode hits in a chamber are used to reconstruct a segment which is meant to represent the trajectory of the particle through the chamber. A time is found for each segment by averaging the anode and cathode times associated with the segment. To remove the large tail in the anode time measurement, a cleaning procedure is applied to the anode times to remove outlier hits. The procedure calculates the average time of the segment and finds the anode hit with the largest difference with the average. If the difference is larger than 26 ns,
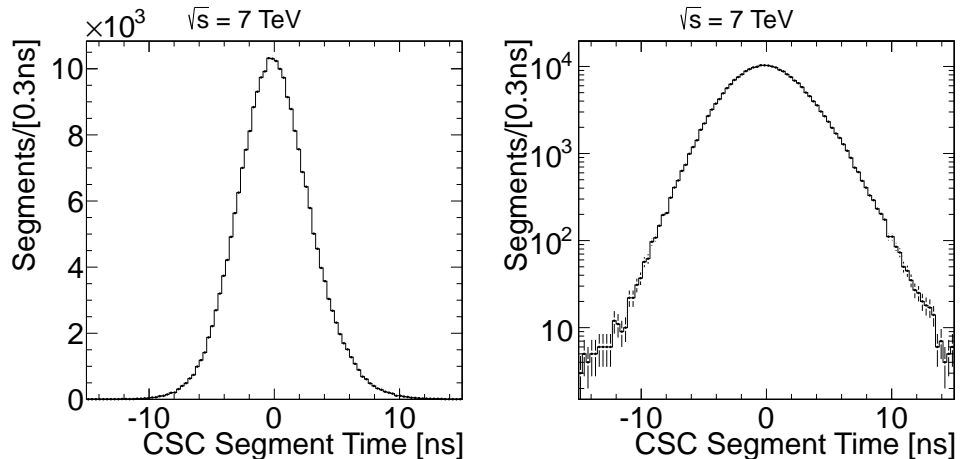
Figure 4.2: Times of segments associated with high-quality muons. Left with linear y-axis scale, right with log scale.

equal to three times the resolution, that hit is removed from the average. The process is then repeated until the anode hit with the largest difference is less than 26 ns. The distribution of the times of segments in data is shown in Fig. 4.2. The data sample used was collected at 7 TeV center–of–mass energy after the full commissioning of the timing measurement and has a p_T threshold of 20 GeV. The resolution on the segment times is 3.0ns.

4.4   CSC Trigger Timing

The CSCs are a key component of the L1 trigger system and it is important that they associate tracks in the system with the correct LHC bunch crossing window. The CSCs build tracks for the L1 trigger with the CSC Track Finder (CSCTF) [20] by combining track stubs coming from the CSC chambers. The stubs are associated with a particular bunch crossing window and the CSCTF uses majority logic of the stubs used to build the track to associate the track with

a bunch crossing window. In cases where there are an equal number of stubs from different bunch crossing windows, say two track stubs coming from adjacent bunch crossing windows, the CSCTF preferentially selects the later bunch crossing window.

As mentioned in Section 3.3.1, there are six layers of cathode strips and anode wires in a CSC chamber. Electronics on the chamber collect hits from the cathode strips and anode wires and separately create trigger primitives called Cathode Local Charged Track (CLCT) and Anode Local Charged Track (ALCT), respectively. The two separate trigger primitives are then combined to form a Local Charged Track (LCT). The ALCT and CLCT trigger primitives must be associated with events within three bunch crossing windows of one another to be combined. The bunch crossing window that the LCT is associated with is set by the ALCT.

The timing of the ALCT is determined by the timing of the third anode hit to arrive to the ALCT circuit board. A common offset per chamber can be applied to the anode hits to give the best timing synchronization of the ALCTs. To determine the offset, the arrival time of the anode hits is studied offline. The average time of the anode hits from a chamber can be correlated with the probability that the same chamber will produce an ALCT in the bunch crossing window before it should (pre-trigger) and after it should (post-trigger). This can be seen in Fig 4.3 (left), which shows the probabilities for each chamber to pre-trigger and post-trigger as a function of the average anode time of each chamber. The data used in the plot was collected in 2010 before the full commissioning of the trigger timing was complete. The offsets for each chamber can be tuned to give an expected pre-trigger and post-trigger probability. The chambers are split into three categories depending on which station and ring they belong to. One

31

category is chambers in the first ring and station, another the chambers in the first ring not in the first station, and the last those not in the first ring. The design of these chambers are all slightly different so it is allowed for them to have different optimal times.

However, the CSCTF logic means that simply setting the offset to give an equal probability to pre-trigger and post-trigger is not optimal. This can be seen by looking at the case where the CSCTF only receives two track stubs; this is also the case where the CSCTF is most sensitive to the offset. If the CSCTF receives one LCT in the bunch crossing window before the collision and one in the correct bunch crossing window, it will preferentially choose the later LCT and associate the combined track with the correct bunch crossing window. In order to pre-trigger the readout of the event, more than one LCT must arrive early. On the other hand, if it receives one LCT in the correct bunch crossing window and one in the proceeding bunch crossing window, the track will be associated with the bunch crossing window following the collision. Thus, the probability to pre-trigger the event can be written as P_-^2 while the post-trigger probability can be written as $2 \times P_+ - P_+^2$ where P_- is the probability to pre-trigger and P_+ is the probability to post-trigger. Figure 4.3 (right) shows the expected probability to pre-trigger and post-trigger at the CSCTF assuming it receives two track stubs versus the average anode time of a chamber.

From these plots an optimal value of 204 ns is chosen for the chambers in the first ring not in the first station and 205 ns for all other chambers. The plot of the pre-triggering and post-triggering at the CSCTF somewhat suggests earlier times would be better but these are not used for two reasons. The first is that pre-triggering at the CSCTF grows as the square of the LCT pre-triggering probability and since, as described below, the offsets can not be set exactly,
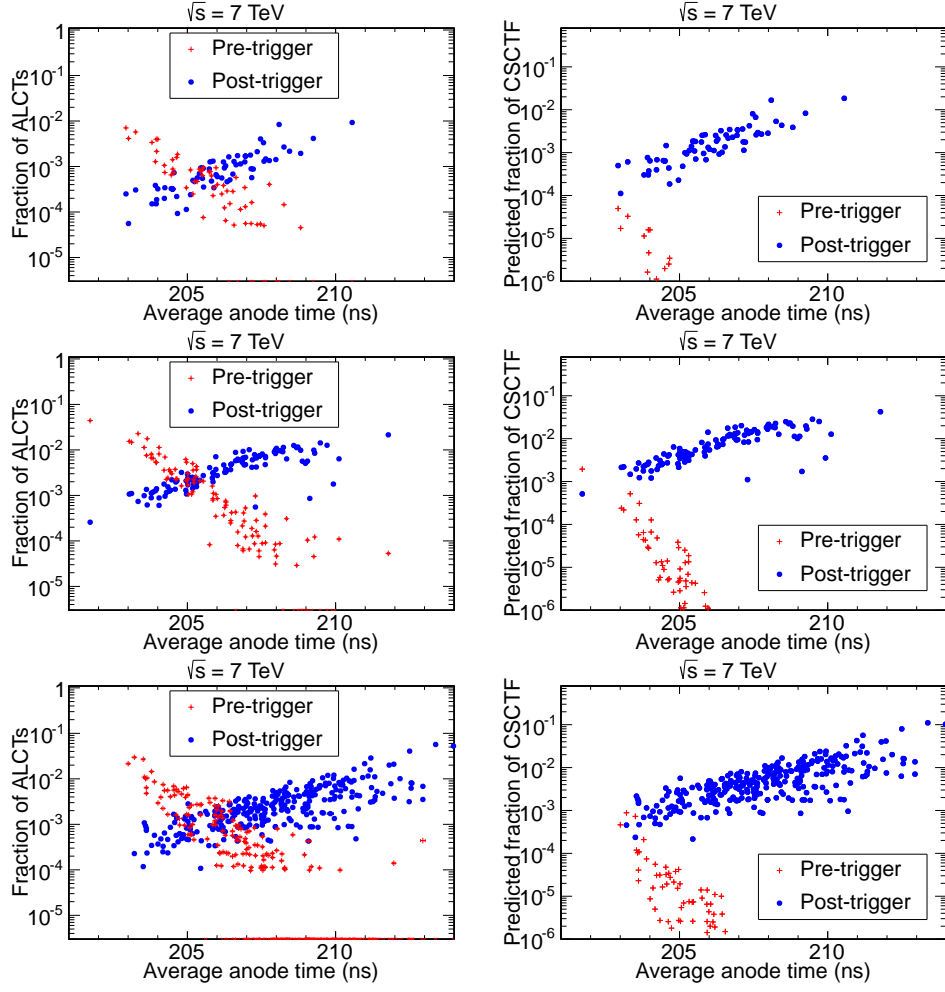
Figure 4.3: Pre-triggering and post-triggering probability versus average anode time. Left column shows the pre-triggering and post-triggering for LCTs. Right column shows what would be expected at the CSCTF when only two track stubs are found. Top row for chambers in the innermost ring and station. Middle row is for all other chambers in the innermost ring. Last row is for all other chambers.

√s = 7 TeV
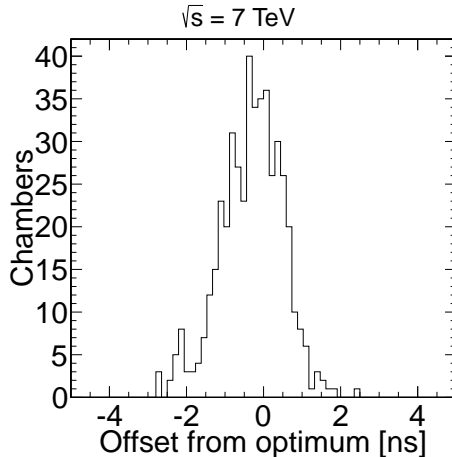
Figure 4.4: Average anode time of chambers relative to optimal values.

chambers that are slightly below optimal could lead to significant pre-triggering in those chambers. Second, pre-triggering prevents the readout of the collision event even if a different part of CMS finds a signature that would normally trigger the readout of the detector as CMS can not readout two consecutive events. Post-triggering does not have this issue as the post-triggered signal would be the one that is blocked. For these reasons slightly later times that still have very low post-triggering probability are used.

The offsets can be moved in roughly 2 ns steps in the chamber electronics with the actual number possibly being different chamber to chamber. Shifting the offsets is a somewhat complicated procedure and carries the risk of accidentally shifting the timing of a chamber by a large amount. Thus, the offsets are changed only when deemed necessary and iterations to get a perfect synchronization are minimized. The synchronization with respect to the optimal values for all chambers is shown in Fig. 4.4 in data taken in 2010 after the offsets had been adjusted. Most of the chambers are within one ns of the optimal time with none more than three ns off.
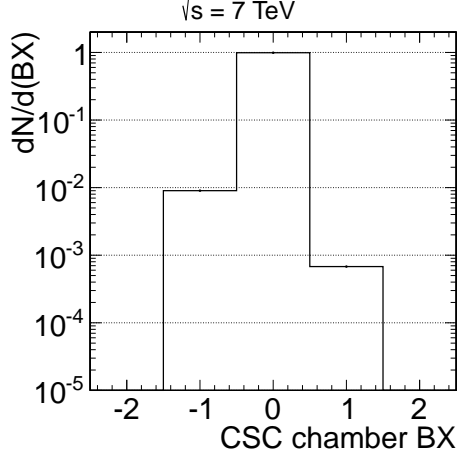
Figure 4.5: Fraction of LCTs versus LCT bunch cross assignment relative to collision event

After this synchronization procedure is performed the timing of the LCTs is very good. This can be seen in Fig. 4.5 which shows the bunch crossing window assigned to LCTs matched to high-quality muons. The distribution is purposefully made asymmetric to account for the CSCTF logic used further downstream. The efficiency to associate the LCT with the correct bunch crossing is 99%, better than the 92% design requirement from [17].

4.5 DT Timing

A complete description of the DT timing measurement can be found in [21], a short summary is given here. Tubes in consecutive layers of a DT chamber are staggered by half a tube, a particle will typical pass alternatively to the left and to the right of the sensitive wires in consecutive layers. The position of hits is inferred from the drift time of the ionization electrons assuming the hits come from a prompt muon. For a late arriving HSCP, the delay will result in a longer

35

drift time being attributed, so hits drifting left will be to the right of their true position while hits drifting right will be to the left. The DT time measurement then comes from the residuals of a straight line fit to the hits in the chamber. The use of residuals means the uncertainty on DT time measurements decreases with more hits in a chamber as the trajectory of the particle in the chamber becomes more well known. Only measurements from the $r - \phi$ superlayers are used in the time calculation as there are eight $r - \phi$ superlayers per chamber while there are only four $r - z$ superlayers. Additionally, the measurements from the $r - \phi$ superlayers have been observed to be more uniform and precise than those from the $r - z$ superlayers.

4.6   Offline Muon Track Timing

Tracks, meant to represent muons or other particles passing through the detector, are built in the muon system connecting together the hits in the different chambers of the CSCs, DTs, and RPCs. The time measurements from the hits on the track can be used to estimate the speed of the particle and the time it left the interaction point. Only time measurements from the CSCs and DTs are used to calculate the timing quantities.

A particle of speed v traveling from the interaction point will arrive at a location d in the muon system at

$$t = d/v + t_0 \tag{4.1}$$

where t_0 is an overall offset. When the local timing variables were defined, they were calibrated such that a speed of light particle would have an average time of zero. Thus d/c has already been subtracted from the times so the same quantity must be subtracted from the right hand side of 4.1. Additionally it is easier to

work with β^{-1} ($\equiv c/v$) instead of v. With these two ideas taken into mind Eq. 4.1 now becomes

$$t = d/v - d/c + t_0 = (d/c) \times (\beta^{-1} - 1) + t_0 \qquad (4.2)$$

Different assumptions can be taken on how the β^{-1} and t_0 parameters are fixed, producing two different variables. The formula has two pieces of input datum: time and distance. The distance from the interaction point to the hit location is known to a much better degree than the time of the hit so the uncertainty on the variables is assumed to come entirely from the time measurement.

The first variable is the speed of the particle assuming it left the origin at $t_0 = 0$ reducing Eq. 4.2 to $\beta^{-1} = tc/d+1$. The measurement of β^{-1} comes from the weighted average of this quantity for all the CSC and DT timing measurements associated with the track. The weight w for CSC measurements is

$$w = \left(\frac{d}{\sigma c} \right)^2 \qquad (4.3)$$

where d is the distance from the hit location to the interaction point and σ is the time resolution of the hit, 7.0 ns for cathode measurements and 8.6 ns for anode measurements as described above. The weight for DT measurements is

$$w = \frac{(n-2)}{n} \left(\frac{d}{\sigma c} \right)^2 \qquad (4.4)$$

where n is the number of ϕ projection measurements found in the chamber from which the measurement comes and the resolution σ is three ns. The factor $(n-2)/n$ accounts for the fact that residuals are computed using two parameters of a straight line determined from the same n measurements (the minimum number of hits in a DT chamber needed for a residual calculation is $n = 3$). Outlier times from anode hits are again cleaned in the same manner as per the segment times. A track will normally have two measurements for each CSC layer

allowing for up to twelve measurements in a CSC chamber, all of which are independent. Each DT ϕ layer can provide a measurement but the times are not independent, the number of degrees of freedom in a DT chamber is two less than the number of ϕ layers hit in the chamber.

The motivation for using β^{-1} now becomes clear; the β^{-1} measurement is linear with t, the source of its uncertainty. This means that β^{-1} will have a much more normal shape than β which would be skewed. An important point here is that the distribution will be close to symmetrical for near speed-of-light muons coming from the LHC.

The uncertainty on β^{-1} can be calculated according to the formula

$$\sigma_{1/\beta} = \sqrt{\sum_{i=1}^{N} \frac{(1/\beta_i - \overline{1/\beta})^2 \times w_i}{N-1}}, \tag{4.5}$$

where $\overline{1/\beta}$ is the average β^{-1} of the track, w_i is the weight of the ith hit, and N is the number of measurements associated with the track.

The speed of the particle is very useful in separating SM muons from HSCP produced in new physics as is shown in Chapter 5. Figure 4.6 shows the β^{-1} measurement, its uncertainty, and the number of degrees of freedom (d.o.f.) for the measurement for: data collected in 2012 at 8 TeV, dominated by collision muons; muons from the simulated Drell-Yan production of Z bosons and photons at 8 TeV; cosmic-ray muons, the sample is defined in Section 5.3; and HSCPs, again the sample is defined in Section 5.3. All of the samples are required to pass the tight requirements on track quality as defined by the Muon POG except for the cosmic-ray muon sample for which the only requirement is that the track be reconstructed in the muon system. It can be seen that the β^{-1} measurement for data and SM MC are strongly peaked at one, the cosmic-ray muons are roughly flat, while the HSCP have β^{-1} greater than one, indicating they are traveling

slowly. The β^{-1} measurement is slightly asymmetric about one for data and SM MC due to the production of delta rays in the muon system which result in early timing measurements in the DTs. The shape of the distribution for cosmic-ray muons is caused by them passing through both the top and bottom halves of CMS and possibly having tracks be reconstructed in both halves. The timing of hits from the two tracks will be separated by approximately 40–80 ns. One of the tracks will trigger the readout of CMS and thus will have β^{-1} roughly around one, these tracks form the plateau in the cosmic-ray muon β^{-1} distribution between zero and two. If the other track is also reconstructed its hits will have timing before zero, if the bottom track triggered the readout of CMS, or after zero, if the top track triggered the readout of CMS. These two possibilities cause the adjacent plateaus at low and high β^{-1} values.

The tails in the β^{-1} distribution for collision muons can be greatly reduced by applying minimal quality requirements on the measurement. This can be seen in Fig. 4.7 (top row) which shows the β^{-1} distribution for the same four samples after requiring the uncertainty on the β^{-1} measurement to be less than 0.07 and for the measurement to have at least eight degrees of freedom.

The average β^{-1} value as a function of η and p_T is shown in Fig. 4.7 (bottom row) for the same data sample described above with the quality requirements on the β^{-1} measurement applied. The average can be seen to have small fluctuations versus η over most of the η range with a larger deviation at the most extreme $|\eta|$ values. The average is almost completely flat against the reconstructed p_T of the muon.

The second variable, vertex time, is the estimated time the particle left the interaction point assuming it traveled at the speed of light. This means setting β^{-1} to one in Eq. 4.2 reducing the equation to simply $t_0 = t$. For muons with
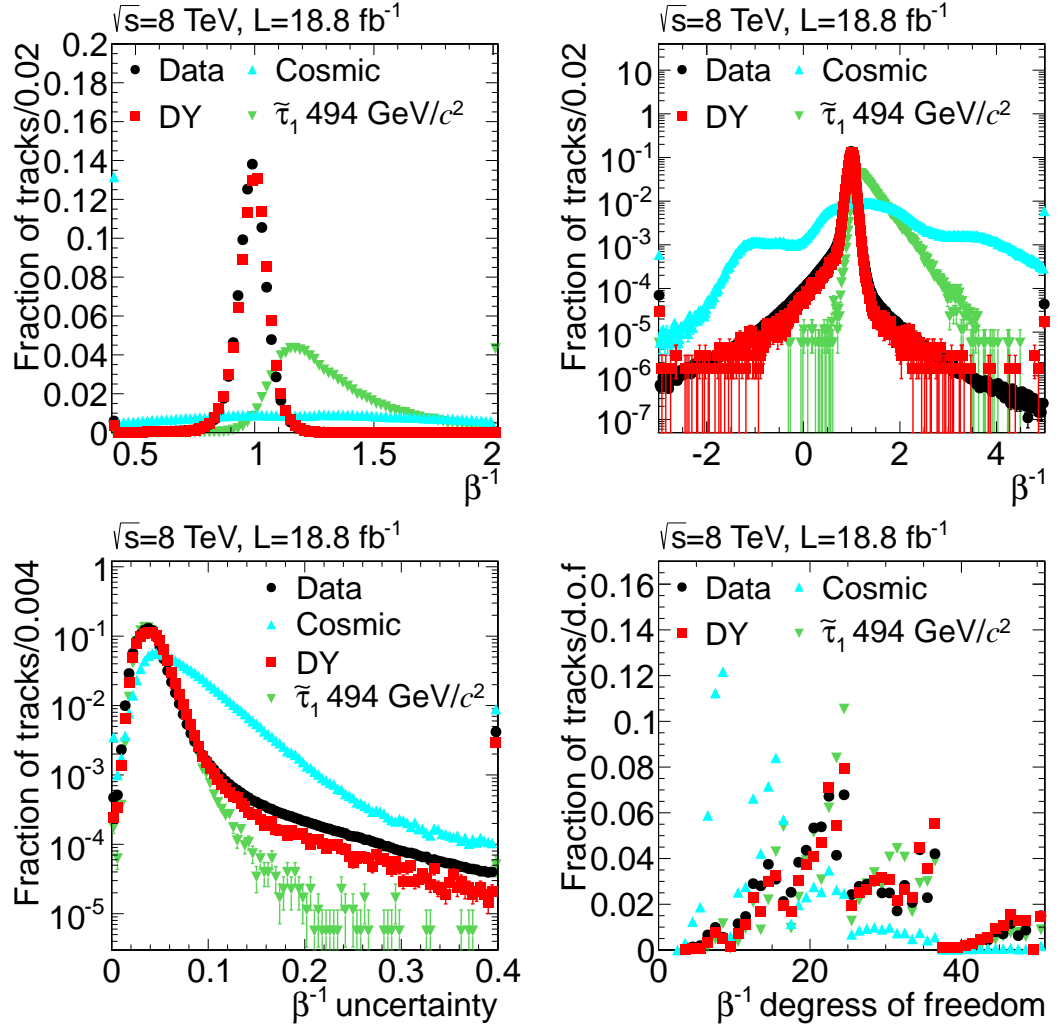
Figure 4.6: Distribution of β^{-1} and associated quantities for data, simulated Drell-Yan production of photons and Z bosons decaying to muons (DY), muons from cosmic-rays, and simulated HSCPs. The top row is the β^{-1} measurement with linear y-axis scale (left) and log scale (right). The bottom row is the uncertainty on the β^{-1} measurement (left) and the number of degrees of freedom for the measurement (right). For all plots the leftmost and rightmost bins contain the underflow and overflow, respectively.
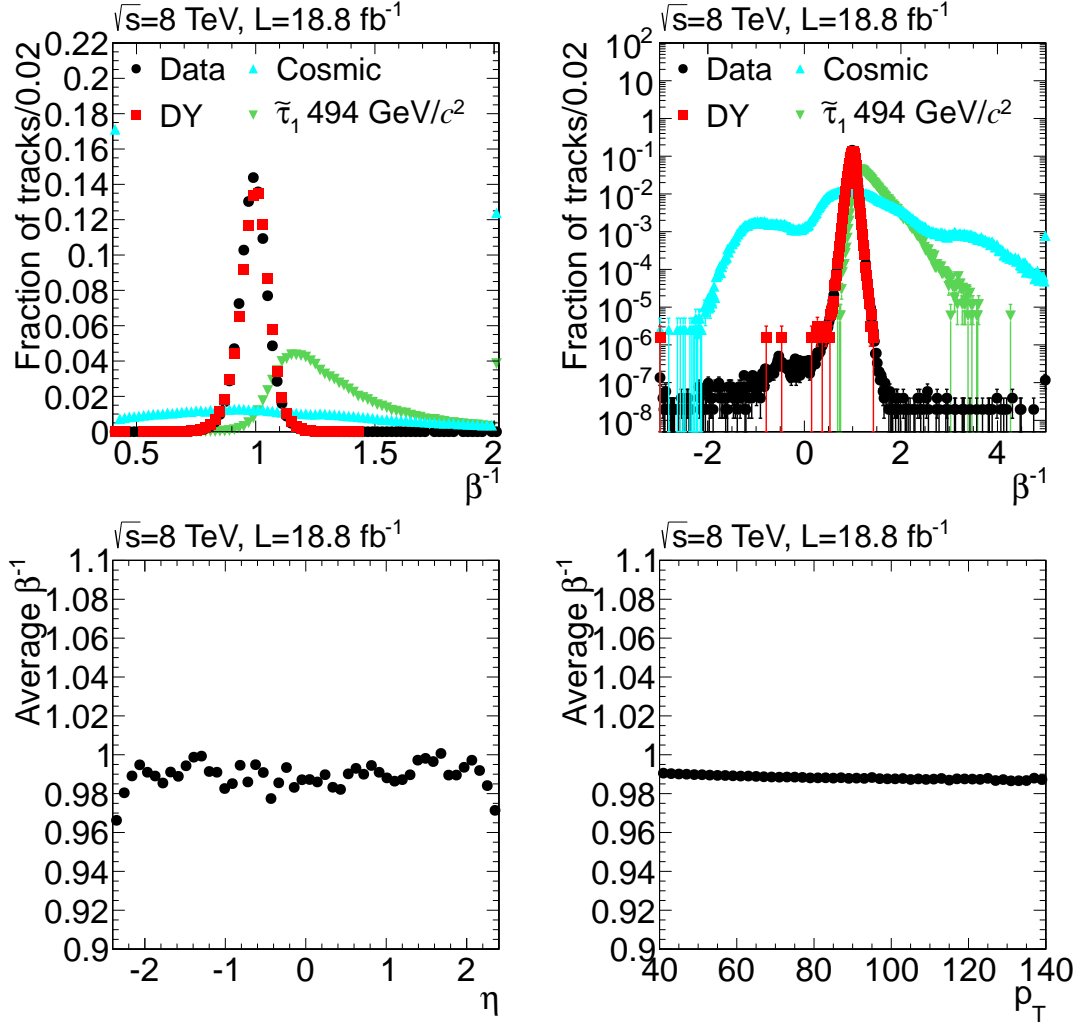
Figure 4.7: Distribution of β^{-1} and associated quantities after applying quality requirements. The top row is the β^{-1} measurement with linear y-axis scale (left) and log scale (right) for data, simulated Drell-Yan production of photons and Z bosons decaying to muons (DY), muons from cosmic-rays, and simulated HSCPs. Both plots have the underflow and overflow included in the leftmost and rightmost bins, respectively. The bottom row is the average β^{-1} measurement versus η (left) and p_T (right).

at least a modest amount of p_T that are produced in a collision in the triggered bunch crossing window this assumption is valid and thus the value should be centered at zero. Figure 4.8 shows the vertex time, its uncertainty, and number of degrees of freedom for the same four samples as in Fig. 4.6. It can be seen that collision muons are tightly centered around zero while the cosmic-ray muons are much more spread out Thus the timing measurement can be used to greatly reduce backgrounds from cosmic-ray muons.

In future operation of the LHC, it is planned to have smaller spacing between proton bunches and more collisions per bunch crossing window. This could potentially lead to muons from bunch crossings adjacent to the crossing triggered for readout being reconstructed in the event. Timing in the muon system could be used to identify and remove these muons.

The question may be asked why not to make a measurement without making any assumptions on t_0 or β^{-1}. This was checked but it was found to have resolution worse by more than an order of magnitude and very little discriminatory power. This is because the assumptions in the previous measurements allowed both of them to use information related to the beam spot, which is approximately three times as far away from the innermost part of the muon system as the outermost part is to the innermost part. The vertex time measurement assumed an error-free propagation of the time in the muon system to the interaction point while the β^{-1} measurement added a new measurement at the interaction point with $t = 0$. This assumption-free measurement is not used for any purpose in CMS.
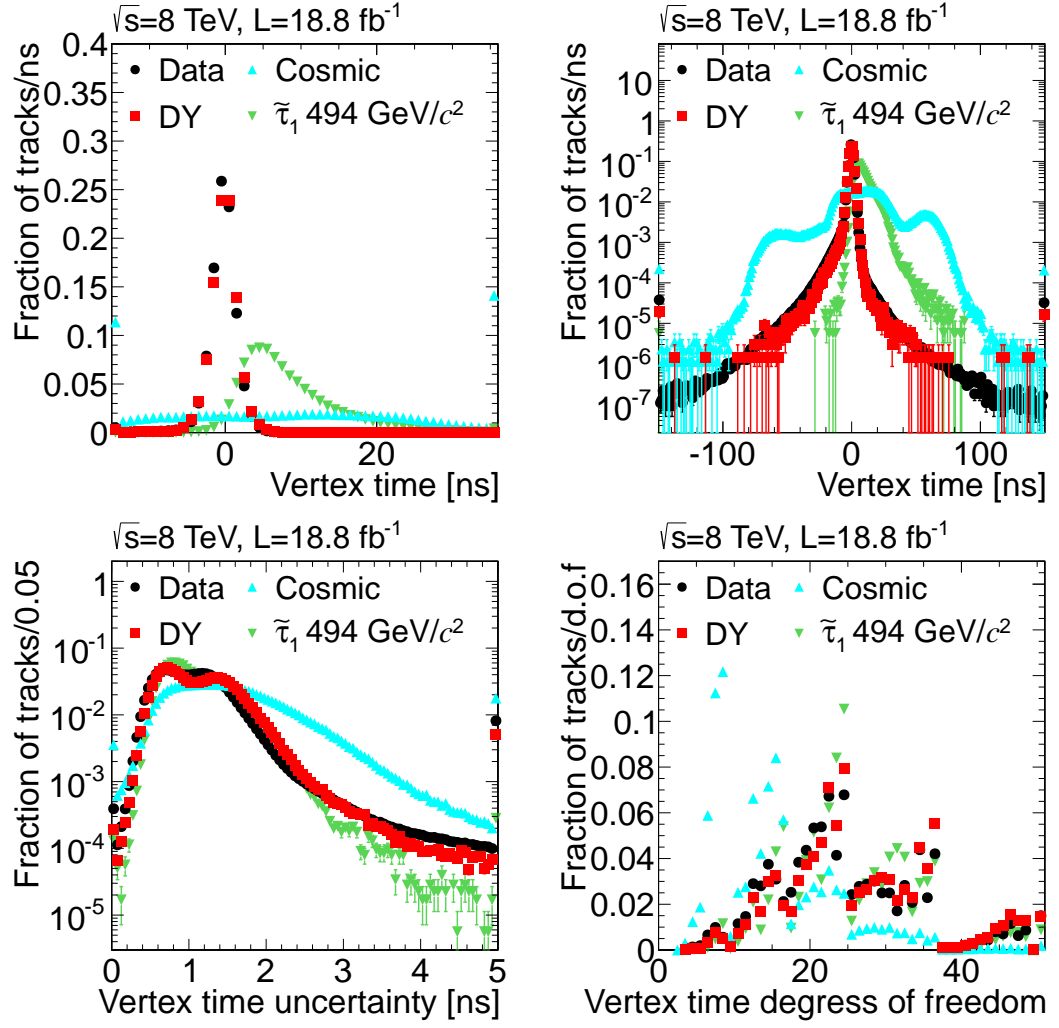
Figure 4.8: Distribution of vertex time and associated quantities for data, simulated Drell-Yan production of photons and Z bosons decaying to muons (DY), muons from cosmic-rays, and simulated HSCPs. The top row is the vertex time measurement with linear y-axis scale (left) and log scale (right). The bottom row is the uncertainty on the vertex time measurement (left) and the number of degrees of freedom for the measurement (right). For all plots the leftmost and rightmost bins contain the underflow and overflow, respectively.

CHAPTER 5

Searches for Heavy Stable Charged Particles

5.1 Foreword

The contents of this chapter are included in a paper authored by the CMS collaboration that is currently in the process of being submitted to a journal. The work was done in a small group within the CMS collaboration with myself being one of the central analyzers. Other major contributors to the work were Loic Quertenmont, Todd Adams, and Venkatesh Veeraraghavan. The paper includes five searches for HSCPs in data collected by CMS during 2011 running at $\sqrt{s}$ = 7 TeV and 2012 running at 8 TeV. Each search is designed to have sensitivity for various different signatures of HSCP. The five searches are all done in the same framework so most of my work was applied to all five analyses. The five searches are labelled *muon only*, *muon+track*, *track only*, *multiple charge*, and *fractional charge*.

For parts of the searches that were different between the five searches, I was essentially the only person to work on the *muon only* analysis and contributed largely to the *muon+track* analysis. I worked on the *track only* and *multiple charge* searches to a slightly smaller degree. My work on the *fractional charge* search was mostly limited to work that was applied across all five searches. Therefore this chapter mostly focuses on the *muon only* and *muon+track* searches, while the *track only* and *multiple charge* searches are presented with the specific parts

that I worked on highlighted. The *fractional charge* search is not presented here.

The journal paper includes both the 2011 and 2012 data taking periods for all the analyses except for the *muon only* analysis which uses the 2012 data only. As the *muon only* analysis is the major focus of this chapter, it was decided to focus on the data collected in 2012 for this chapter. Additionally, the 2012 dataset was taken at a higher energy and includes approximately four times the integrated luminosity as the 2011 dataset, making the sensitivity of the searches determined to a large degree by the data collected in 2012. The procedure for analyzing the data from the two periods is identical. A statistical combination of the 2011 and 2012 dataset for all the analyses except for *muon only* is presented at the end of the chapter.

5.2 Introduction

As discussed in section 2.3, new heavy long-lived charged particles are predicted in many extensions to the SM. HSCPs with lifetimes $\gtrsim 40$ ns are likely to traverse the entire CMS detector before decaying and will thus be directly detectable. Some of the HSCP combine with SM particles to form composite objects that can be electrically charged or neutral. Interactions with the CMS detector may change the SM constituents of the particles and through this their electric charge. The HSCPs will be produced with high momentum but their large mass means that a majority will have a velocity, $\beta \equiv v/c$, less than 0.9. As no heavy long-lived SM particles are expected to be produced at the LHC, HSCPs would be the only high momentum particles with β not very close to one. Detector signatures unique to slow moving particles are exploited to search for HSCP. The backgrounds to the searches are SM particles with detector mismeasurement and in some cases muons coming from cosmic rays.

Previous collider searches for HSCPs have been performed at LEP [22, 23, 24, 25], HERA [26], the Tevatron [27, 28, 29, 30], and the LHC [31, 32, 33, 34, 35, 36, 37, 38]. The results from such searches have placed important bounds on BSM theories [39, 40], such as lower limits on the mass of gluinos, stops, and staus at 1098, 737, and 223 GeV/c^2, respectively.

Four different searches are presented here. The *muon only* analysis requires only that a track be found in the muon system. This analysis is expected to still have sensitivity when all particles are produced electrically neutral. The *muon+track* analysis requires that the muon system track be matched to a track in the inner tracker. This analysis is especially powerful for lepton-like HSCP. The third analysis is the *track only* analysis that only requires a track be found in the inner tracker so that it can be sensitive to particles becoming neutral in the calorimeter and leaving no hits in the muon system. The *multiple charge* analysis looks for particles with $Q > 1e$ and reconstructed like in the *muon+track* analysis.

For all plots in this chapter, the first and last bins contain the underflow and overflow, respectively.

5.3 Samples

Data collected with the CMS detector during 2012 running at an energy of $\sqrt{s} = 8$ TeV are searched. The data collection was split into four periods labeled A, B, C, and D. All data collected by CMS undergo a prompt reconstruction as described in section 3.3.2. The first two run periods, A and B, underwent an additional re-reconstruction so as to have the latest reconstruction improvements and calibration constants. The re-reconstructed samples are used for the A and B periods while the promptly reconstructed samples are used for the C and D

periods.

CMS has a Data Certification team which checks all data collected and certifies the data as good for analysis. The certification requires all detector subsystems to be operating at full ability, or at least close enough to full ability to not have a detrimental effect on offline analyses. Additionally, higher level objects such as muons and electrons are checked to make sure the data are good for physics analyses. For this particular analysis, the RPC trigger plays an important role, as discussed in section 5.4, and so the RPC is required to be included in the L1 trigger for all data searched. This leads to the searches using slightly less data than most other CMS analyses on 2012 data. The data sample used by this analysis corresponds to 18.8 fb^{-1}.

Multiple different signal Monte Carlo (MC) simulation samples are produced to account for the different signatures an HSCP could have; more detail on the signal models can be found in Sec. 2.3.

Pair production of strongly–interacting gluino and stop samples are produced with masses in the range 300–1500 GeV/c^2 and 100–1000 GeV/c^2, respectively. The gluinos are generated in the split SUSY scenario [41, 42]. under the assumption of high squark masses of 10 TeV. The samples are generated using PYTHIAv8.153 [43] Samples are produced with the fraction f of gluinos forming neutral glueball $R - hadrons$ set to $f = 1.0$, 0.5, and 0.1. The samples are also produced with two different modelings of the nuclear interaction of R-hadrons with matter: the cloud interaction and charge suppressed models. The charge suppressed model results in all $R - hadrons$ being neutral after a nuclear interaction. The cloud interaction model should be assumed for samples unless explicitly stated otherwise. Most HSCP will not have a nuclear interaction while passing through the CMS tracker, however almost all of them will have such an

interaction in the calorimeter.

The above effects can lead to many interesting signatures in the CMS detector. R-hadrons neutral after hadronization will generally remain neutral through the tracker but may gain charge in the calorimeter under the cloud model and leave hits in the muon system. If the glueball fraction is 1.0, then this would be the only way to detect gluino HSCP. The *muon only* analysis is designed to have sensitivity to HSCP of this type. On the other hand HSCP produced charged under the charge suppression model will likely be charged in the tracker but always neutral in the muon system. The *track only* analysis is designed to be sensitive to HSCP of this type. A third signature is an HSCP charged in both the muon and tracker systems which would have a signature similar to a muon. HSCP produced neutral under the charge suppression model would never be charged during their passage through CMS and thus are outside the scope of an HSCP search.

The p_T, η, and β distributions of gluino and stop particles at generation are shown in Figs. 5.1 and 5.2, respectively.

Additional samples are produced creating lepton-like HSCP. Stau pair samples are produced under the minimal gauge-mediated supersymmetry breaking (mGMSB) scenario [13] using the SPS7 slope [44]. The ISASUGRA version 7.69 [45] program is used to set the particle mass scale and decay chains by specifying six parameters. The number of messenger particles is set to three; the ratio of the mass of the messenger particles to the effective SUSY breaking mass scale is set to two; $tan\beta = 10$, this β being the ratio of the vacuum expectation values of the neutral Higgses; the sign of the supersymmetric Higgs mass parameter is made greater than zero; and c_{Grav} is greater than 10000. The low number of messenger particles results in the stau being the NLSP. The high value of C_{Grav} results in the stau being long-lived while varying Λ from 31 to 180 TeV gives
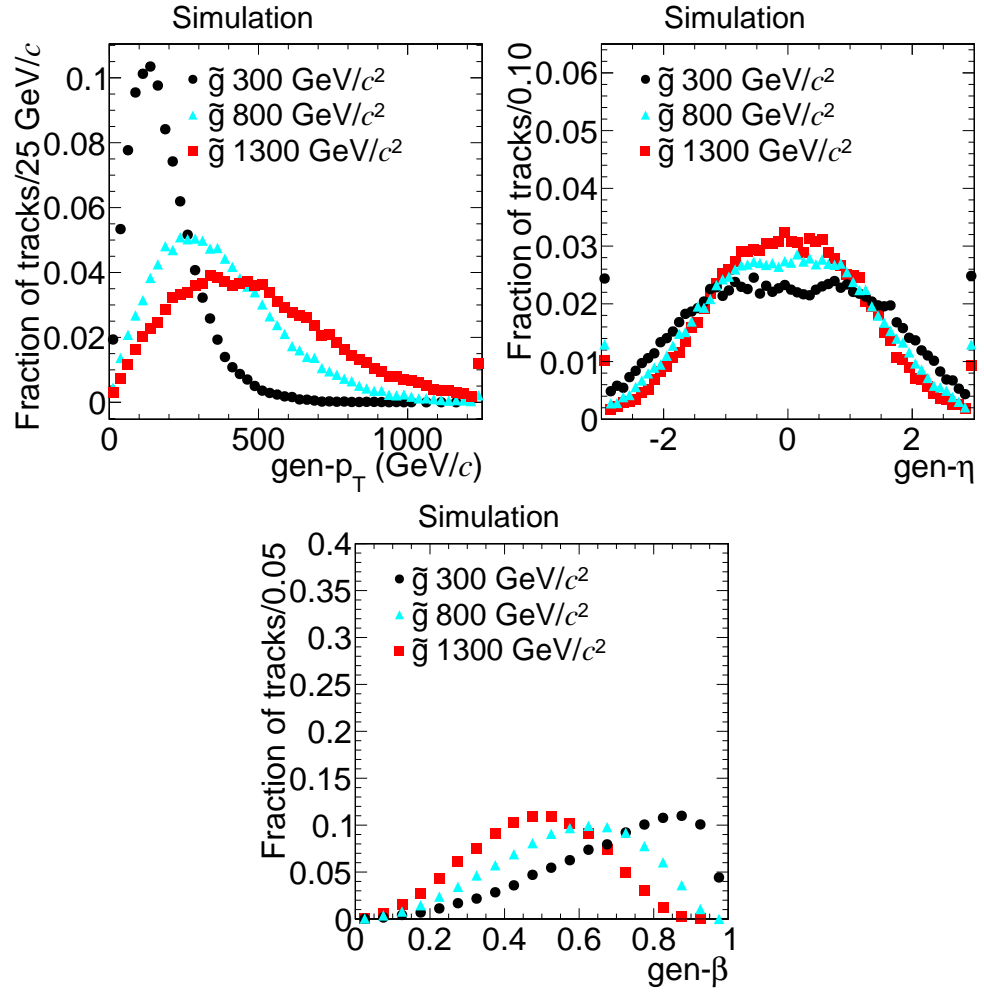
Figure 5.1: Distribution of various kinematic variables for various gluino ($\tilde{g}$) samples at generation: p_T (top left), η (top right), and β (bottom).
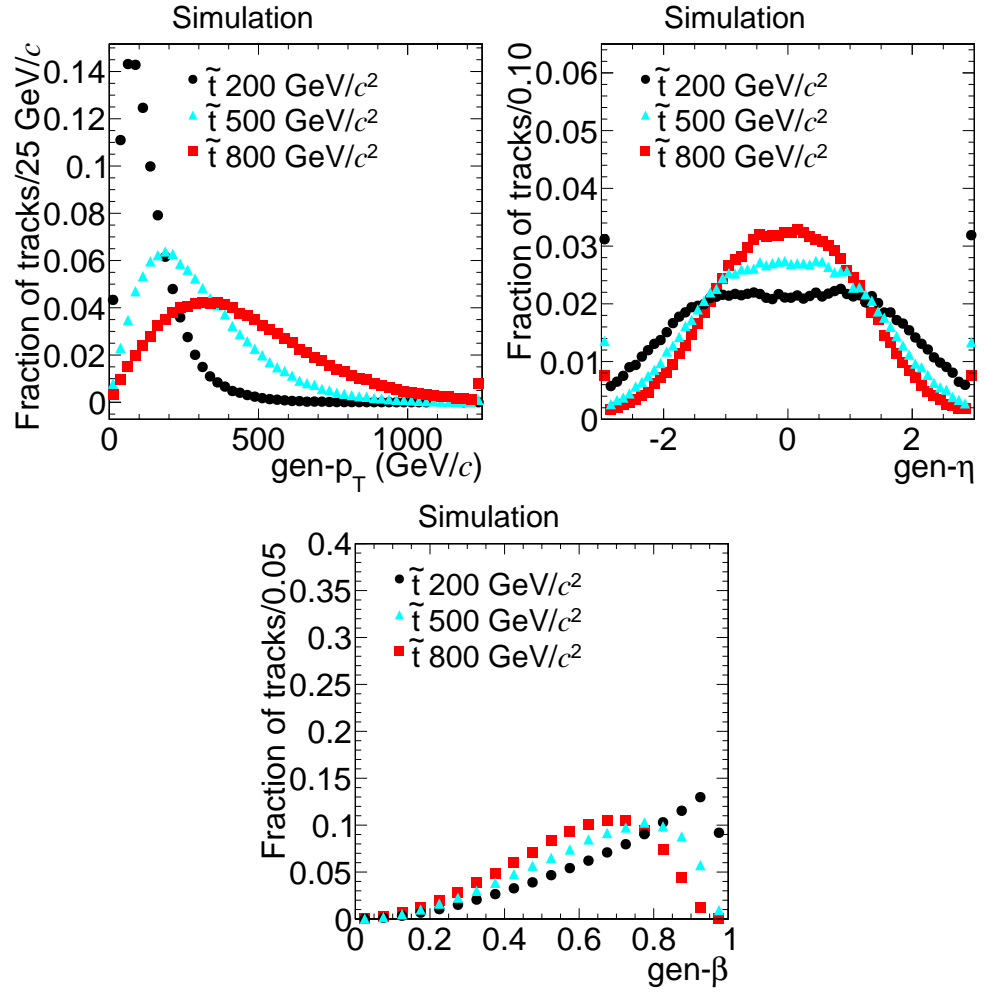
Figure 5.2: Distribution of various kinematic variables for various stop samples at generation: p_T (top left), η (top right), and β (bottom).

staus within a mass range of 100–557 GeV/c^2. The produced mass spectrum and decay chains are passed to PYTHIAv6.426 [46]. Stau production proceeds either by direct electroweak production or from the cascade decay of other particles (usually through the pair production of gluinos and squarks). Cascade decay is dominant due to the strong nature of the production mechanism. In order to give the best results while maintaining model independence, two stau samples are used: one with both direct production and production from cascade decays (CD) and one with staus only produced through direct production (DP). The second sample is less dependent on the model parameters. The distribution of p_T, η, and β at generation are shown in Figs 5.3 and 5.4 for various CD and DP stau samples, respectively.

The last of the signal samples used is modified Drell-Yan production of long-lived leptons with different electrical charges. In the model considered, the particles are neutral under $SU(3)_C$ and $SU(2)_L$ but still interact through $U(1)_Y$ interactions [14]. As all SM particles that reach CMS have Q equal to $1e$ or are neutral, the possibility of HSCPs with non-unit charge is interesting. The production of these particles is simulated with PYTHIAv6.426 [46]. Samples are produced with charge Q = $1e$, $2e$, $3e$, $4e$, $5e$, $6e$, $7e$, and $8e$ for masses of 100-1000 GeV/c^2 for $1e <= Q <= 5e$ and 200-1000 GeV/c^2 for $Q > 5e$. The distribution of p_T, η, and β at generation for various charges and masses are shown in Fig. 5.5.

All MC simulation events are overlaid with additional proton-proton collisions, see Section 3.2. Weights are given to the events so that the distribution of additional collisions in the MC simulation samples matches what is observed in data. The reconstruction of the event by CMSSW tries to identify each proton-proton collision as a separate primary vertex [47]. The distribution of the number
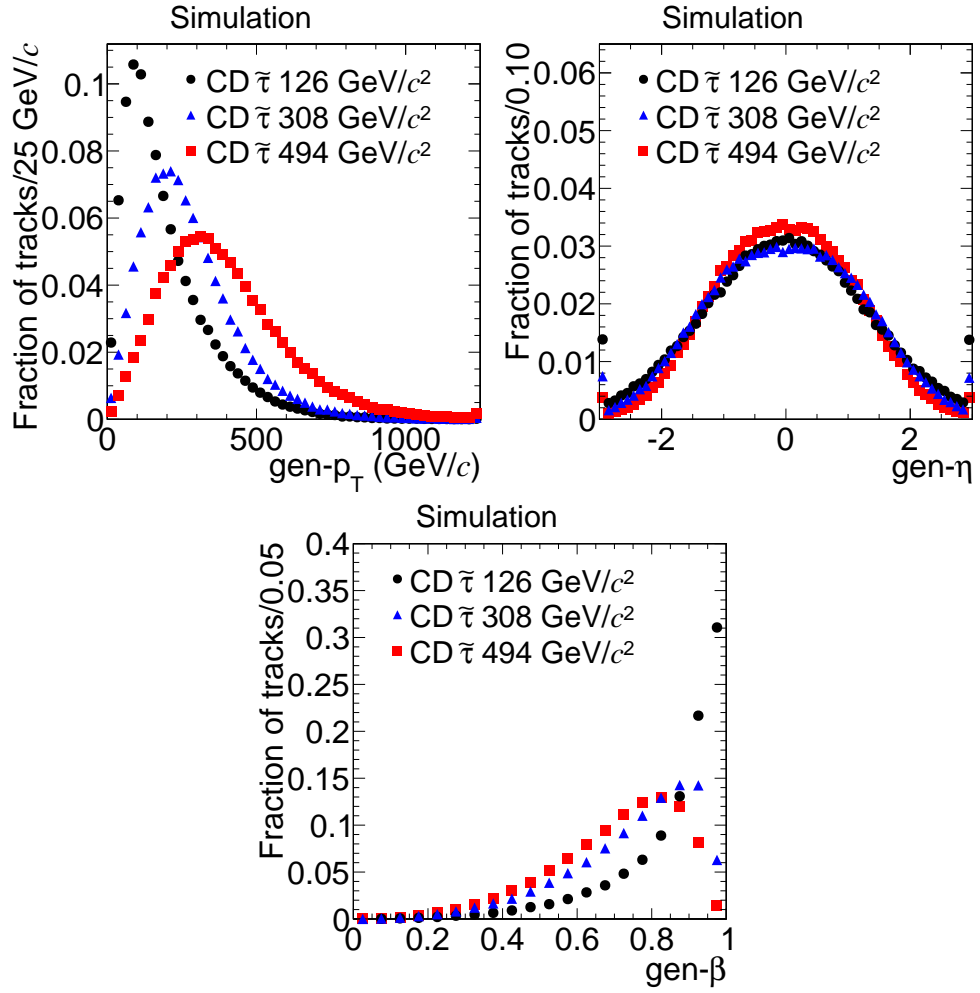
Figure 5.3: Distribution of various kinematic variables for various CD stau ($\tilde{\tau}$) samples at generation: p_T (top left), η (top right), and β (bottom)
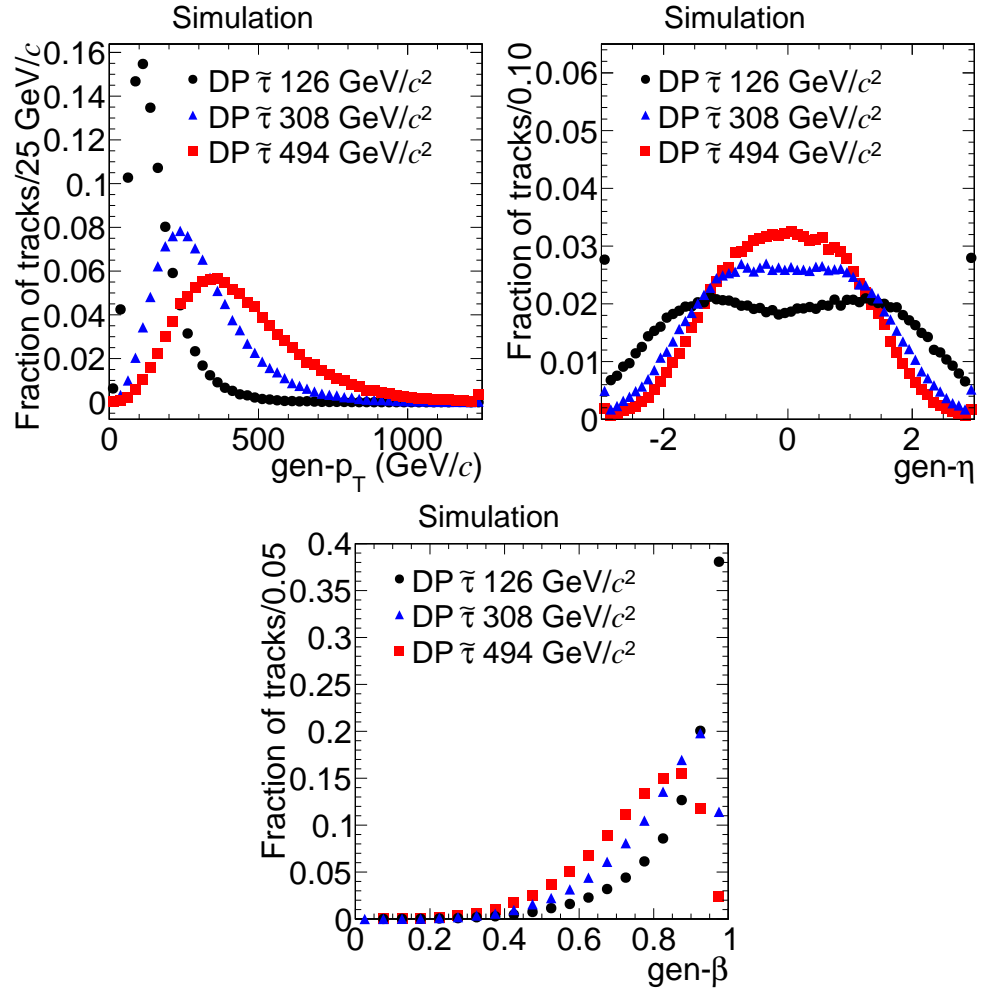
Figure 5.4: Distribution of various kinematic variables for various DP stau ($\tilde{\tau}$) samples at generation: p_T (top left), η (top right) and β (bottom).
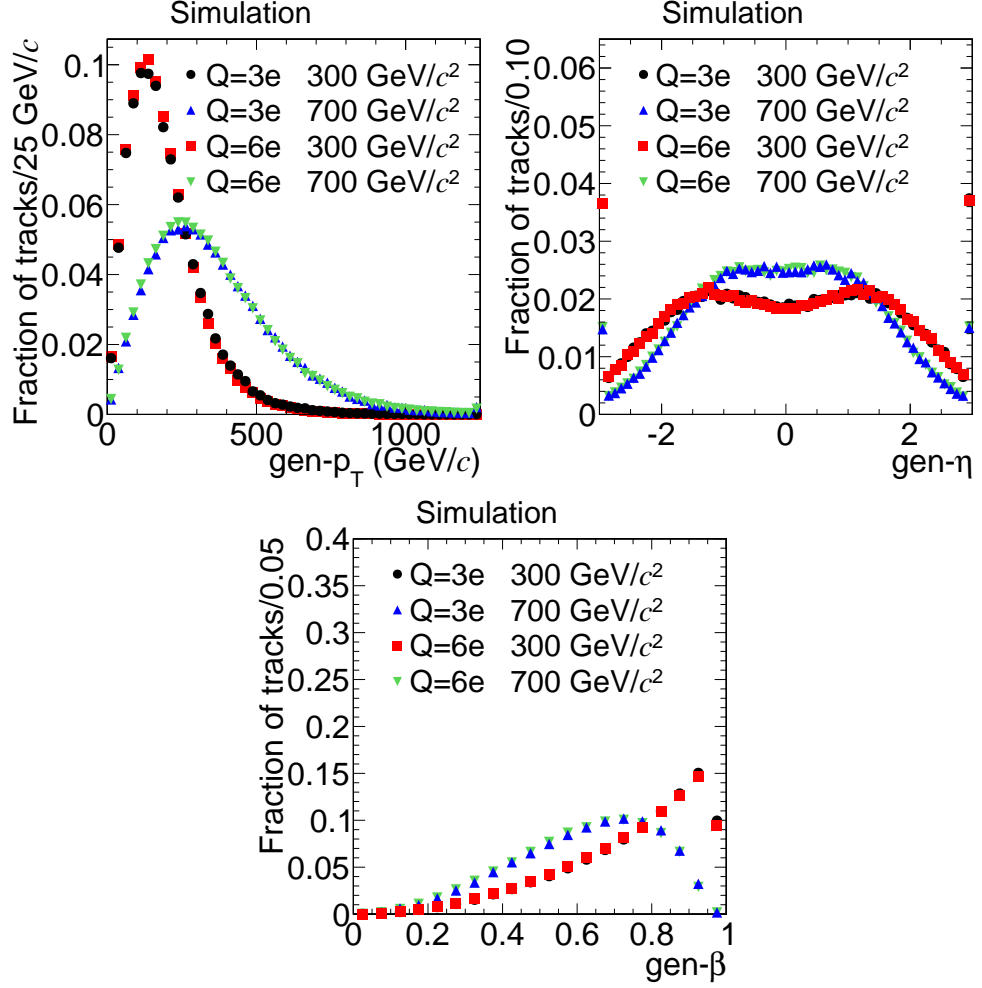
Figure 5.5: Distribution of various kinematic for modified DY samples with various charges and masses at generation. Top: p_T (left) and η (right). Bottom: β
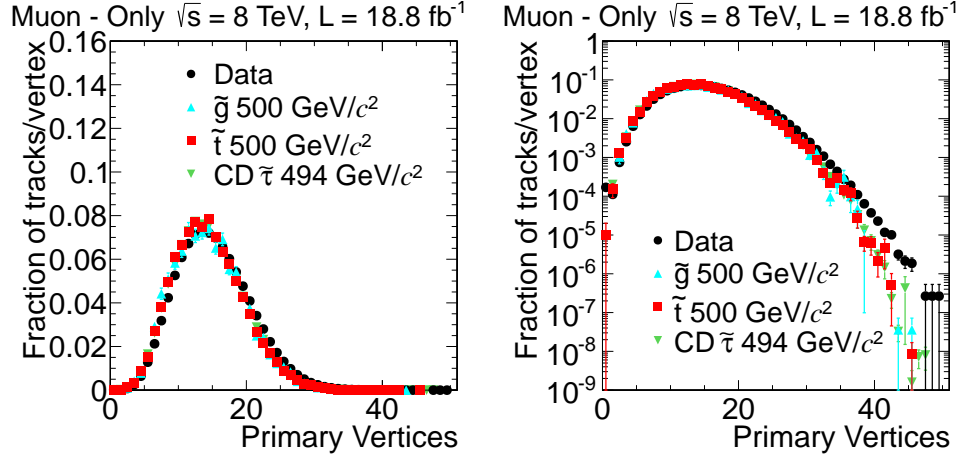
Figure 5.6: Distribution of number of primary vertices in data and various MC simulation samples. The samples shown in the figure are required to have been collected with one of the three triggers detailed in Sec. 5.4. Left with linear y-axis scale, right with log scale.

of primary vertices found in events after the reweighting is shown in Figure 5.6 for data and MC simulation. The samples shown in the figure are required to have been collected with one of the triggers detailed in Sec. 5.4.

5.4 Trigger

As discussed in Sec. 3.3.2, in order for an event to be triggered for readout it must pass one of a collection of algorithms. The data used in this chapter is required to have been collected by algorithms looking for a high momentum track to be found and/or missing transverse energy, MET, as calculated by the particle flow algorithm [48].

The particle flow algorithm attempts to reconstruct all particles in an event, then calculates MET as the magnitude of the negative vector sum of the trans-

verse momenta of the particles. The MET calculated by the particle flow algorithm is referred to as PFMET. As the proton-proton collision occurs at rest in the transverse plane, PFMET is meant to represent the magnitude of the vector sum of all particles not found by the particle flow algorithm. For most CMS analyses, PFMET is created by either the limited detector response in finding all tracks in an event and determining their momentum or from neutral particles in the event which leave no signals in the detector. These neutral particles could be neutrinos from the SM or new neutral particles created in a BSM theory such as supersymmetry.

For HSCP, PFMET often arises because of details of the particle flow algorithm. The algorithm assumes SM particles and rejects tracks that do not conform to the properties expected of a SM particle. Two types of possible HSCP tracks are rejected by the algorithm.

The first type is tracks reconstructed only in the muon system. The only charged SM particles that are expected to reach the muon system are muons. As muons should have a matching track in the inner tracker, particle flow rejects tracks found only in the muon system. HSCP produced neutral then acquiring charge by interacting with the calorimeter would only have a track in the muon system and as such would not be included in the PFMET calculation.

The second type is tracks produced charged but becoming neutral as they propagate through CMS. The particle flow algorithm rejects tracks reconstructed only in the inner tracker that have a track p_T much larger than the associated energy deposited in the calorimeter as this indicates the track has been misreconstructed. As an HSCP only deposits approximately 10 GeV of energy in the calorimeter and normally has > 100 GeV of momentum, HSCP neutral in the muon system will likely be rejected.

These two effects lead to PFMET in HSCP events to be roughly equal to the vector sum of any R–hadrons neutral in either the muon system or the inner tracker, less however much energy they deposit in the calorimeter. This effect is illustrated in Figures 5.7 and 5.8 which compare the di-HSCP system with online PFMET in gluino pair events with at least 150 GeV of online PFMET.

One trigger issue unique to slow-moving particles is the timing acceptance of the L1 trigger. If an HSCP arrives in the muon system too late, it can trigger the readout of the wrong bunch crossing. As most of the CMS subdetectors, though not the muon system, are designed to not readout data coming from adjacent bunch crossings, the data from the correct bunch crossing would be lost. To help deal with this, members of the CMS L1 trigger team developed a special configuration of the RPC L1 trigger to partially recover HSCP that arrive in the muon system in the bunch crossing window following the crossing that produced them. This configuration is discussed in Sec. 3.3.2.

The first trigger used, L2Mu+MET, requires both a high-momentum track to be found in the muon system and large PFMET. The algorithm starts at the L1 step where a track must be found in the muon system by the detector electronics with a momentum greater than 16 GeV and $|\eta|$ less than 2.1 in order to trigger the readout of the event to the computing farm. There, the L1 track is used to seed the reconstruction of the track in the L2 step using only data readout from the muon system. The track is required to have $p_T > 70$ GeV, $|\eta| < 2.1$, and hits in at least two muon stations. In the L3 step, the particle flow algorithm is run and the calculated PFMET must be greater than 55 GeV. For the first 0.7 fb^{-1} of 2012 running the threshold on PFMET was at 65 GeV. The signal samples are weighted to account for the amount of data taken at each threshold.

The lack of a requirement that the track be found in the silicon tracker allows
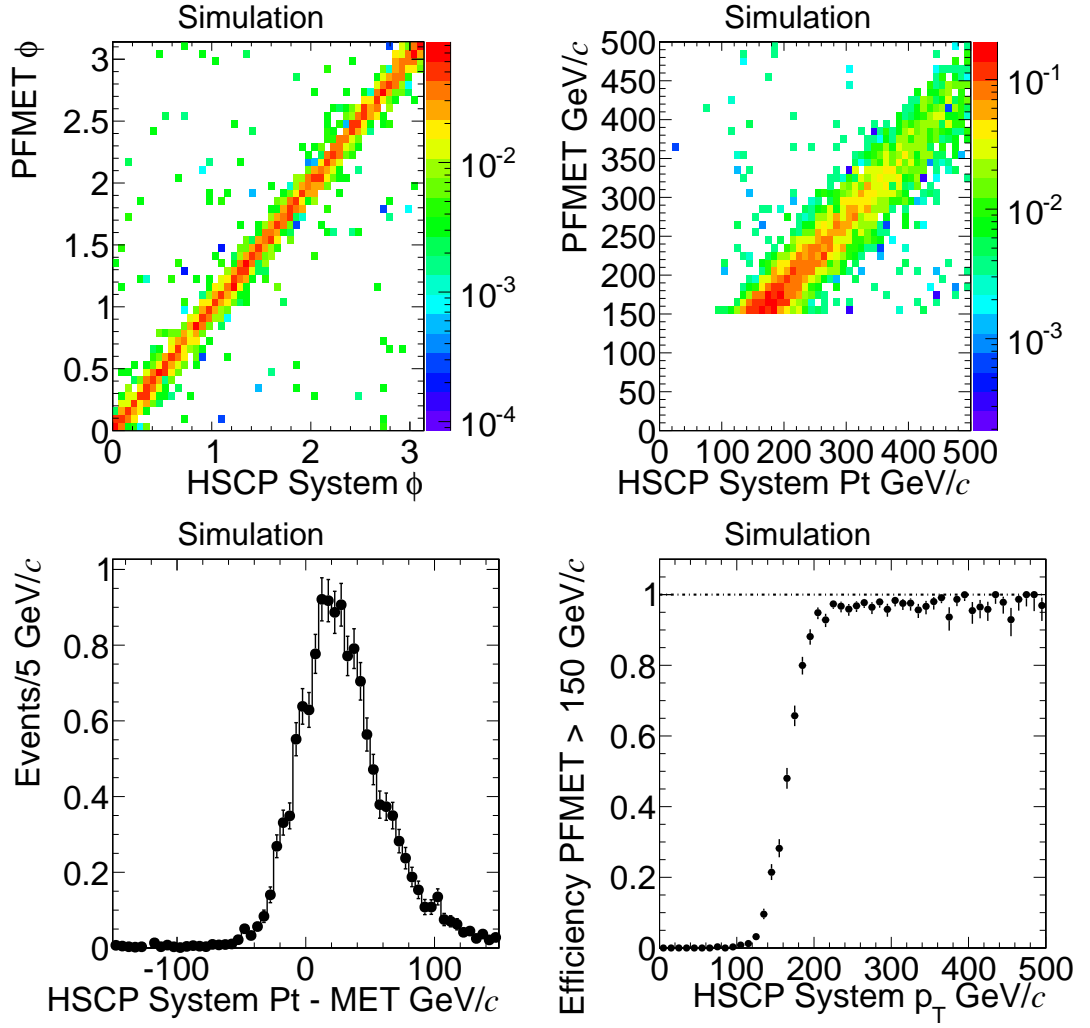
Figure 5.7: Comparison of di-HSCP system with online PFMET for a 1200 GeV Gluino $f = 1.0$ sample. All figures but the bottom right one only consider events with at least 150 GeV of online PFMET. Top Left: Online PFMET ϕ versus di-HSCP system ϕ. Top Right: Online PFMET value versus di-HSCP system p_T. Bottom Left: Difference between di-HSCP system p_T and online PFMET value. Bottom Right: Probability to have online PFMET greater than 150 GeV versus di-HSCP system p_T. A horizontal dashed line is drawn at one.
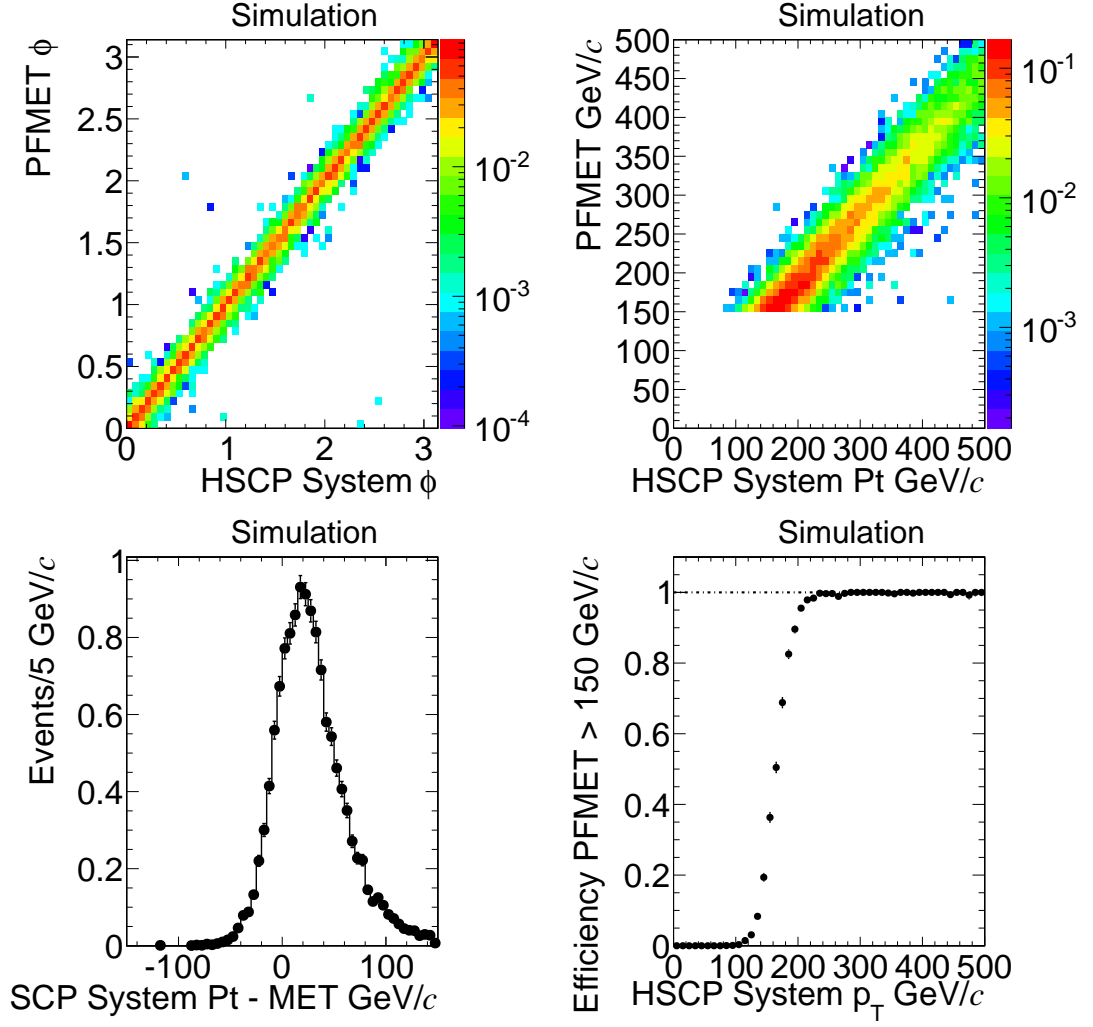
Figure 5.8: Same as Fig. 5.7 but the sample used is 1200 GeV $f = 0.1$ charge suppressed gluino.

the trigger to be sensitive to R-hadrons produced neutral and only later becoming charged. The main objective of the PFMET requirement is to reduce the rate of events collected by the trigger down to a few Hertz. The momentum measurement by the muon system suffers from long tails and the rate would be too large even with a very high momentum threshold. Events collected with this trigger are only used in the *muon only* analysis.

The second trigger used, Mu40, requires a high momentum track matched in both the silicon tracker and muon system be found. During the L1 and L2 steps, the algorithm follows the same procedure as the above trigger, with the only difference being that p_T threshold on the L2 track is reduced to 16 GeV and only one muon station is required to have hits. During the L3 step, the L2 track is used to seed the reconstruction of tracks that span from the silicon tracker to the muon system. A track must be found with momentum greater than 40 GeV and $|\eta|$ less than 2.1. The very good resolution of the silicon tracker allows for an acceptable trigger rate without any further requirements. Events collected with this trigger are only used in all analyses.

The third trigger used, PFMET150, requires at least 150 GeV of PFMET be found at the L3 step. The L1 and L2 steps of the trigger calculate the MET in the event using only the energy deposits in the calorimeter, a faster method than particle flow, and apply looser requirements on the MET of 40? and 80? GeV, respectively. Events collected with this trigger are only used in all analyses.

The decision to use the pure PFMET trigger even when a muon signature is required offline is prompted by the late arrival of the HSCPs in the muon system. Even with the RPC configuration described above, very slow moving HSCP can trigger the readout of the wrong event but still be reconstructed offline if the event has been triggered by the pure PFMET trigger. This can be seen in Figure 5.9
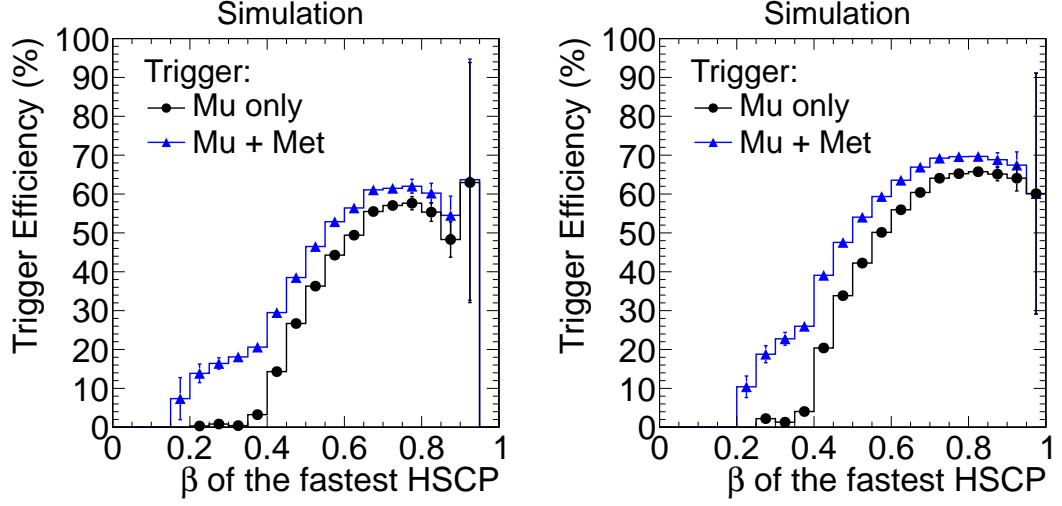
Figure 5.9: Trigger efficiency as a function of the β of the fastest HSCP reconstructed offline in the muon system with only the muon triggers and additionally including the pure PFMET trigger. The samples are 1200 GeV Gluino $f = 0.1$ (left) and 800 GeV stop (right).

which shows the trigger efficiency versus β with and without the pure PFMET trigger. It can be seen that using the pure PFMET trigger allows the search to probe lower β particles.

When evaluating trigger efficiencies, it is important to only consider events that have a possibility of being selected offline. For the case of strongly charged HSCP this is made more difficult as some events may not have any $R - hadrons$ electrically charged while they pass through the detector. To deal with this, the trigger efficiencies are reported with respect to events where at least one HSCP is found offline. The efficiency for each trigger, as well as the combined efficiency, is listed for various signal samples in Tables 5.1 and 5.2 in events with at least one HSCP reconstructed in the muon system and the muon system plus the silicon tracker, respectively. The simulation has been found to provide

Table 5.1: Efficiency in percentage for various models for the L2Mu+MET, Mu40, PFMET150 triggers and a combination of the three. The efficiencies are with respect to events with at least one HSCP reconstructed in the muon system.

Model	Mass (GeV)	L2Mu+MET	Mu40	PFMET150	Total
Gluino $f = 0.1$	400	34.3	35.6	19.4	58.6
Gluino $f = 0.1$	800	31.2	31.6	22.6	54.9
Gluino $f = 0.1$	1200	24.6	26.6	20.5	47.5
Gluino $f = 1.0$	400	36.6	5.6	23.2	46.1
Gluino $f = 1.0$	800	31.9	5.0	24.5	43.4
Gluino $f = 1.0$	1200	23.6	3.7	20.6	35.5
Stop	200	27.3	42.8	11.2	58.8
Stop	500	31.1	42.1	19.8	61.2
Stop	800	30.3	41.6	21.6	60.7

a good modeling of muon reconstruction [19] and MET determination [49] by CMS. Further discussion of possible residual differences between simulation and data can be found in Sec. 5.10.

Muons from cosmic rays are an important background for the *muon only* analysis. To study and predict them, a trigger that selects events when no beams are passing through CMS is used. The trigger requires the presence of a muon system track with $p_T > 20$ GeV, no proton bunches passing through CMS within 50ns, and for the event not to be flagged as beam halo. Beam halo [50] occurs when protons acquire enough transverse momentum by the repulsive electric forces of the proton bunch to form a halo around the bunch. If the radius is large enough the beam halo can interact directly with CMS before the proton bunch reaches the center of CMS. The muon system track reconstruction used for the cosmic

Table 5.2: Efficiency in percentage for various models for the Mu40, PFMET150, triggers and a combination of the two. The efficiencies are with respect to events with at least one HSCP reconstructed in both the muon system and inner tracker.

Model	Mass (GeV)	Mu40	PFMET150	Total
Gluino $f = 0.1$	400	51.87	16.06	59.09
Gluino $f = 0.1$	800	46.50	20.50	56.42
Gluino $f = 0.1$	1200	38.96	19.56	49.95
Stop	200	58.43	7.69	61.54
Stop	500	56.91	17.40	64.44
Stop	800	56.15	20.49	65.59
CD Stau	100	97.86	14.74	98.06
CD Stau	308	97.03	17.53	97.47
CD Stau	494	95.56	17.76	96.35
DP Stau	100	95.06	0.17	95.09
DP Stau	200	95.78	0.37	95.82
DP Stau	494	95.23	1.16	95.36

ray muon trigger is slightly different than for the collision trigger. However both reconstructions are required offline as discussed in section 5.6 so no bias is introduced.

Throughout the rest of this chapter, the data sample is defined to be events collected with the L2Mu+MET, Mu40, or PFMET150 triggers if in reference to the *muon only* analysis For the other analyses it is defined to be events collected with either the Mu40 or PFMET150 triggers. The cosmic-ray control sample used in the *muon only* analysis is defined to be events collected with cosmic-ray trigger discussed above. In all following discussions or figures, simulated samples must have passed one of the triggers associated with the relevant analysis.

5.5   Selection Variables

HSCPs can be distinguished from SM particles in CMS due to their high momentum and slow speed. The momentum of a particle can be determined by its bending in the magnetic field of CMS. The slow speed of HSCPs lead to two interesting detector signatures. The first is that the particles will arrive at the detector elements later than SM particles will. The muon system, being the furthest detector element from the interaction point, has the largest timing difference. The measurement of the arrival time of particles in the muon system is discussed in Ch. 4. The β^{-1} variable is used in the searches to discriminate between HSCPs and SM particles. The second interesting signature is that HSCP have a larger amount of ionization energy loss per unit length than SM particles of the same momentum as discussed below.

5.5.1 Transverse Momentum Measurement

A muon passing through CMS will likely be reconstructed three times [19]; once only in the silicon tracker, referred to as a tracker track; once only in the muon system, referred to as a stand-alone muon; and once as a combined track found in both the muon system and silicon tracker, referred to as a global muon. CMS measures the curvature of a track which is proportional to and can be used to determine the Q/p_T of the track. In the central region of CMS, tracker tracks have a resolution on Q/p_T of 1% for muons at intermediate momentum and 7% at high momentum with the resolution being approximately twice as large in the forward region. Intermediate momentum is defined as 15–100 GeV and high momentum is defined as 400–1000 GeV. Stand-Alone muons in the central region have a resolution on Q/p_T of 8% for intermediate momentum and 25% [51] for high momentum with the uncertainty again being about twice as large in the forward region. The resolution for global muons is the same as for tracker muons for intermediate momentum and is slightly better than tracker muons at high momentum at 6% in the central region.

The *muon only* analysis uses the p_T measurement coming from the stand-alone muon while the rest of the analyses use the measurement from the tracker track. The tracker track momentum is used even when the global muon is available due to issues specific to R-hadrons. R-hadrons are unlikely to undergo a nuclear interaction while traversing the silicon tracker so they would have the same electric charge at all points in the tracker. While passing through the muon system however, R-hadrons will often undergo a nuclear interaction with the steel return yoke located between the muon stations possibly causing the electric charge to change in the middle of the muon system. This behavior affects the momentum measurement of the HSCP track in the muon system.

To convert the measured Q/p_T to p_T, a charge of $Q = 1e$ is assumed. For R-hadrons that can change their charge inside of CMS it can be the case that the average value of Q during their passage through the muon system does not equal $1e$. This effect has different consequences for the stop and gluino samples.

A stop particle, specifically not an anti-stop, has a charge of $+(2/3)e$ and forms an R-hadron with either an anti-quark ($\tilde{t}\bar{q}$) or two quarks ($\tilde{t}qq$). Anti-quarks have a charge of $-(2/3)e$ or $+(1/3)e$ leading to R-hadrons with a charge of either 0 or $+1e$. Quarks have a charge of either $+(2/3)e$ or $-(1/3)e$ which allows for the creation of R-hadrons with a charge of 0, $+1e$, or $+2e$. Thus a stop R-hadron will always have a positive charge or be neutral. For an anti-stop, the effect is reversed and the R-hadron will always have a negative charge or be neutral.

For gluino R-hadrons this statement does not hold true. Gluinos can hadronize into glue balls ($\tilde{g}g$), R-mesons ($\tilde{g}q\bar{q}$), or R-baryons with either quarks or anti-quarks ($\tilde{g}qqq$ or $\tilde{g}\bar{q}\bar{q}\bar{q}$), allowing the charge of the R-hadron to range from $-2e$ to $+2e$. This leads to the average charge of the R-hadron as it traverses the muon system to often be less than $1e$ and the p_T value to be overestimated allowing for further separation between HSCP and SM particles.

To observe this effect the function $\Delta(Q/p_T)$ is defined in Equation 5.1

$$\Delta(Q/p_T) = ((Q/p_T)_{SA} - (Q/p_T)_{Tk})/(Q/p_T)_{Tk} \tag{5.1}$$

where "SA" refers to stand-alone muon qualities and "Tk" refers to tracker track qualities. As the p_T resolution of tracker tracks is much better than for stand-alone muons, it is a sufficiently good approximation of the true particle momentum. Figure 5.10 shows the distribution of $\Delta(Q/p_T)$ for tracks with inner track $p_T > 200$ GeV for data and various simulated HSCP signal samples. A value of zero in this plot indicates the p_T was reconstructed correctly while negative one
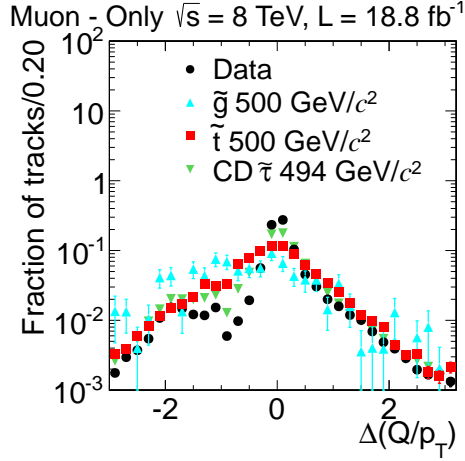
Figure 5.10: Distribution of $\Delta(Q/p_T)$ for data, 500 GeV gluino, 500 GeV stop, and 494 GeV CD stau.

indicates the reconstructed p_T approaches infinity. The CD stau sample, which does not change charge, has a distribution similar to data, though slightly wider. The slight discontinuity at negative one is due to particularities of the reconstruction but only affects a small number of tracks. The stop sample, which is not able to flip charge but merely to switch between one sign and zero, is centered at zero but with a slightly wider width than data or CD stau. The gluino sample, which can flip charge, is centered closer to negative one meaning that the reconstructed p_T is normally larger than what is generated, sometimes to a very large degree. This increases the differences between gluino HSCPs and the background.

For the lepton like samples with non-unit charge, the p_T will be mismeasured by a factor of $1/Q$. This means that multiply charged particles will have their p_T underestimated making them somewhat harder to separate from backgrounds. This effect can be seen in Figure 5.11.
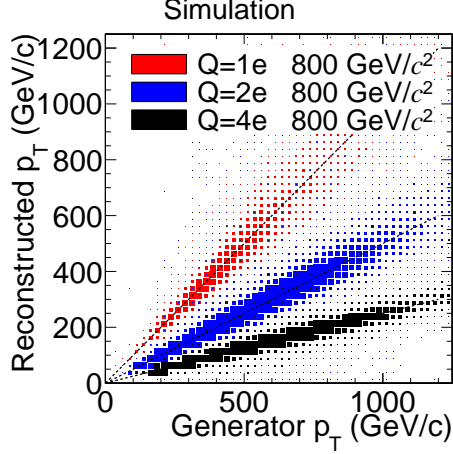
Figure 5.11: Distribution of reconstructed p_T versus generator p_T for Q=1e, 2e, and 4e samples.

5.5.2 Energy Loss Measurement

The amount of ionization energy a particle deposits can be measured by the silicon tracker. For paticles with $0.1 \gtrsim \beta\gamma \lesssim 1000$, where γ is $1/\sqrt{1-\beta^2}$, the average amount of the ionization energy deposited per unit length in a given material, dE/dx, is to a large degree dependent only on the velocity of the particle and its charge as described by the Bethe-Bloch formula [15]. The dependence of dE/dx on charge varies approximately as Q^2, meaning that even a $Q = 2e$ HSCP will have almost four times as much energy loss as a SM particle. The dependence on speed for particles with $0.1 < \beta < 0.9$ varies approximately as $1/\beta^2$; so slow moving HSCP would have large dE/dx values. At higher speeds, the energy loss has a broad minimum up to $\beta\gamma$ of 1000. Particles in this broad minimum all have close to the same energy loss and are generically referred to as minimum ionizing particles (MIP). Above this level, radiative effects become important as they cause very rare, very high-energy losses that result in an increase to the

68

average energy loss. Techniques described below are used to help mitigate the effect of this radiative rise.

A short description of the dE/dx measurement is included here, a more detailed description can be found in [47, 31, 52]. As in [36], two variables related to dE/dx are calculated for each track. The first is a harmonic mean of the dE/dx measurements along the track;

$$I_h = \left(\frac{1}{N} \sum_i c_i^{-2} \right)^{-1/2},$$ (5.2)

where N is the number of measurements in the silicon-strip tracker and c_i is the energy loss per unit path length of the ith measurement. The use of a harmonic mean greatly reduces the impact of the rare radiative losses as the highest energy losses are effectively given less weight than lower energy losses. This leads to all SM particles produced at the LHC with momentum above 10 GeV on average having I_h values close to the minimum value ($\approx 3\mathrm{MeV/cm}$). HSCP will have high I_h as their energy loss is consistently large.

The second variable is I_{as} which is a modified version of the Smirnov-Cramer-von Mises [53, 54] discriminant. The discriminant is given by:

$$I_{as} = \frac{3}{N} \times \left(\frac{1}{12N} + \sum_{i=1}^{N} \left[P_i \times \left(P_i - \frac{2i-1}{2N} \right)^2 \right] \right),$$ (5.3)

where P_i is the probability for a MIP to produce a charge smaller or equal to that of the ith measurement in the silicon-strip tracker for the observed path length in the detector, and the sum is over the measurements ordered in terms of increasing P_i. The probabilities are found from tracks with momentum greater than five GeV collected with a trigger requiring only that a proton collision occured inside CMS. The discriminant is designed to give the best separation between MIPs and high-ionizing particles. The discriminant is peaked at zero for

MIPs and approaches one for high-ionizing particles. The same measurements are used to determine I_h and I_{as} so the variables are not independent.

An estimate of the mass m, assuming Q=1e, of a particle can be made from I_h and the momentum p of a track. This is done by using Eq. 5.4;

$$I_h = K \frac{m^2}{p^2} + C. \tag{5.4}$$

with $K = 2.559 \pm 0.001$ MeV cm^{-1} c^2 and $C = 2.772 \pm 0.001$ MeV cm^{-1} as determined from low momentum protons [31].

5.6 Preselection

Candidates for the *muon only* analysis are tracks identified as stand-alone muons. Candidates for the *muon+track* and *multiple charge* analyses are tracks identified as global muons. The candidates for the *track only* analysis are tracker muons. Various requirements are applied to the candidates in order to reduce tracks from background processes while maintaining good efficiency for HSCP.

5.6.1 Preselection for *muon only*

The *muon only* analysis requires the tracks to have $p_T > 80$ GeV, $|\eta| < 2.1$, and valid DT or CSC hits in at least two muon stations to reinforce the requirements applied at trigger level. The distributions of η and number of muon stations are shown in Fig. 5.12 for data, the cosmic-ray muon control sample, and signal MC. The discontinuities in the η distribution are due to interfaces between the detector elements in the muon system.

Quality cuts on the β^{-1} measurement are applied. The measurement must have at least eight degrees of freedom and the uncertainty must be less than 0.07.

Additionally the track must have β^{-1} greater than one. A potential background source is muons coming from adjacent bunch crossings. Tracks are required to have a measured time at vertex not be within ± 5 ns of an expected adjacent collision. Figure 5.13 shows the distribution of these quantities for data, cosmic-ray muon control sample, and signal MC.

Additional cuts are used to control the background from cosmic-ray muons. Tracks are vetoed if the displacement of the track with respect to the beam spot is larger than 15cm in either the longitudinal or transverse direction relative to the beam line. The track $|\phi|$ must not be within 1.2–1.9 radians, this region represents tracks pointing in the vertical direction, as is expected of cosmic-ray muons. Cosmic-ray muons travel through the top and bottom halves of the detector leaving hits in the muon system opposite of the track. Thus, it is required that there be no muon segments with η within 0.1 of $-\eta_{track}$. The requirement is only applied to segments separated from the track by at least 0.5 in ϕ so that tracks with η close to zero do not match to their own segments. Figure 5.14 shows the distribution of these quantities.

5.6.2 Preselection for *muon+track*

The *muon+track* analysis applies cuts on the inner tracker track, which has a much better p_T and impact parameter resolution than the muon system track. The track is required to have $p_T > 45$ GeV and $|\eta| < 2.1$ to match the trigger level requirements. Quality cuts are applied as low quality background tracks can have mismeasured momentum and potentially high fluctuations in dE/dx. The inner track is required to have at least eight hits in the inner tracker with at least two coming from the pixel detector. At least 80% of the hits associated with the track must be considered valid. As in [36], a cleaning procedure is applied to the
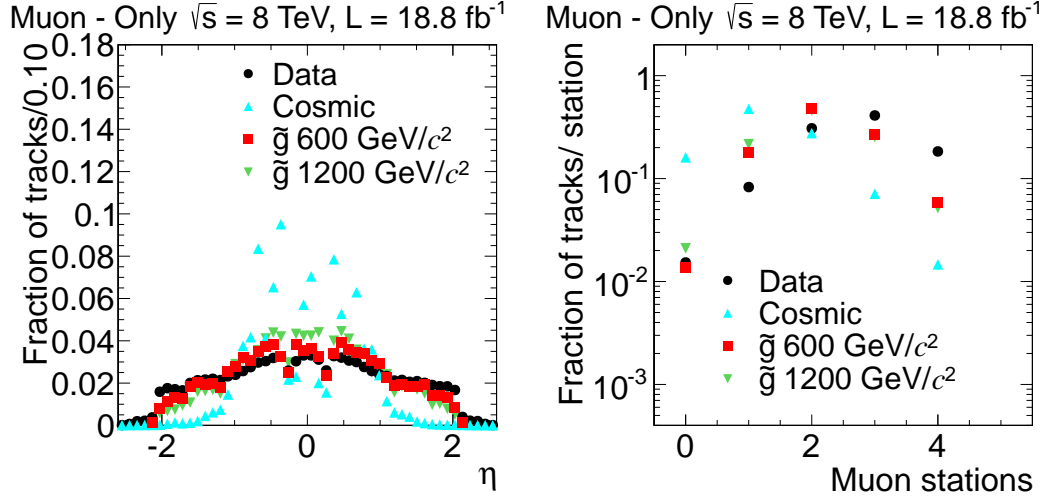
Figure 5.12: Distribution of η (left) and number of matched muon stations (right) for tracks in the *muon only* analysis for data, cosmic-ray muon control sample, and signal MC.

hits before calculating dE/dx that is intended to remove anomalous energy loss from overlapping tracks, nuclear interactions, and hard δ-rays. There must be at least six measurements passing this cleaning. Figure 5.15 shows these variables for data and signal MC.

The relative uncertainty on the track p_T (σ_{p_T}/p_T) must be less than 0.25 and the χ^2 per degree of freedom must be less than five. While cosmic-ray muons are expected to be a negligible background in the *muon+track* analysis loose cuts are placed on the impact parameter of the track, these cuts are nearly 100% efficient for signal particles. The displacement of the track with respect to the primary vertex with the smallest longitudinal displacement must be less than 0.5 cm in both the transverse and longitudinal directions with respect to the vertex with the smallest longitudinal displacement. Figure 5.16 shows p_T uncertainty, χ^2 per degree of freedom, and the d_z and d_{xy} displacement for data and signal MC.
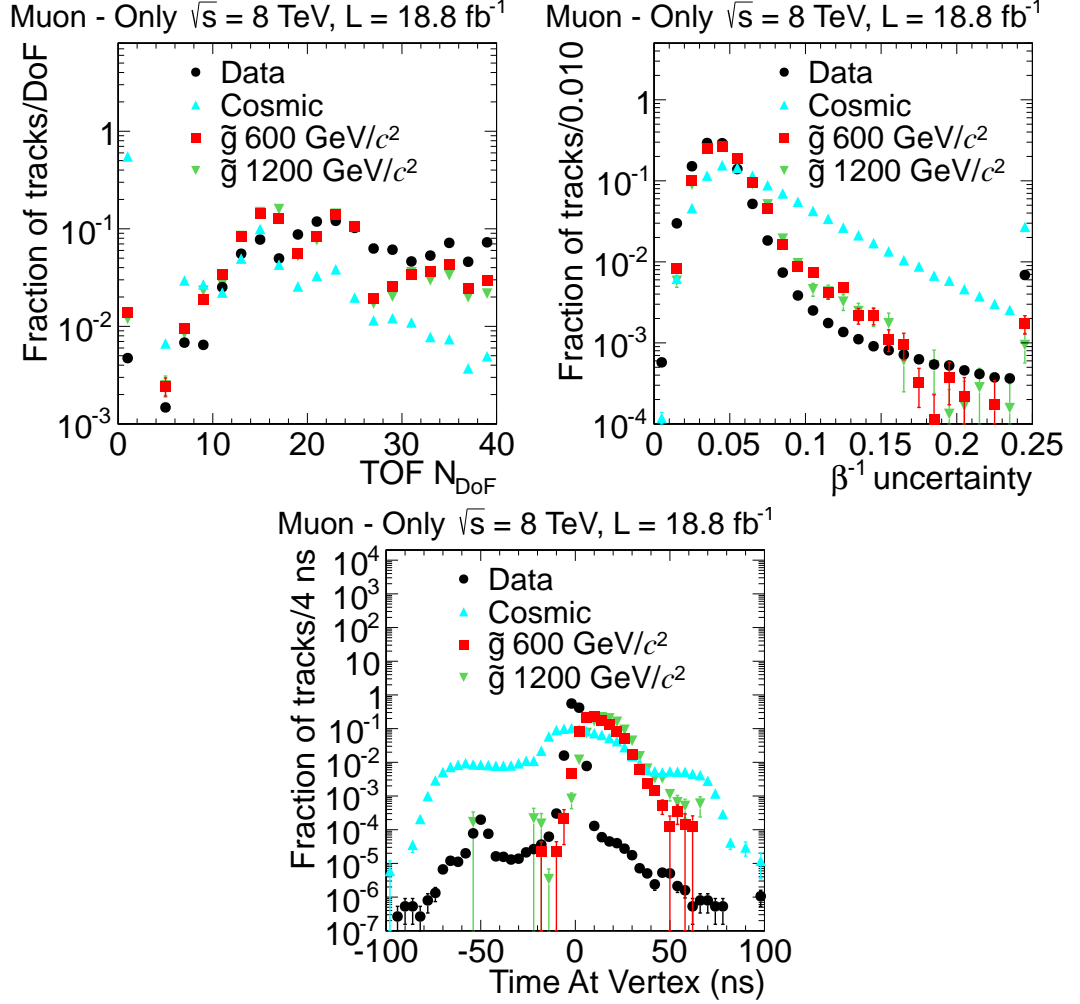
Figure 5.13: Distribution of various preselection variables in the *muon only* analysis for data, cosmic-ray muon control sample, and signal MC. Top row: Number of degrees of freedom (left) and uncertainty (right) on the β^{-1} measurement. Bottom row: Time at vertex.
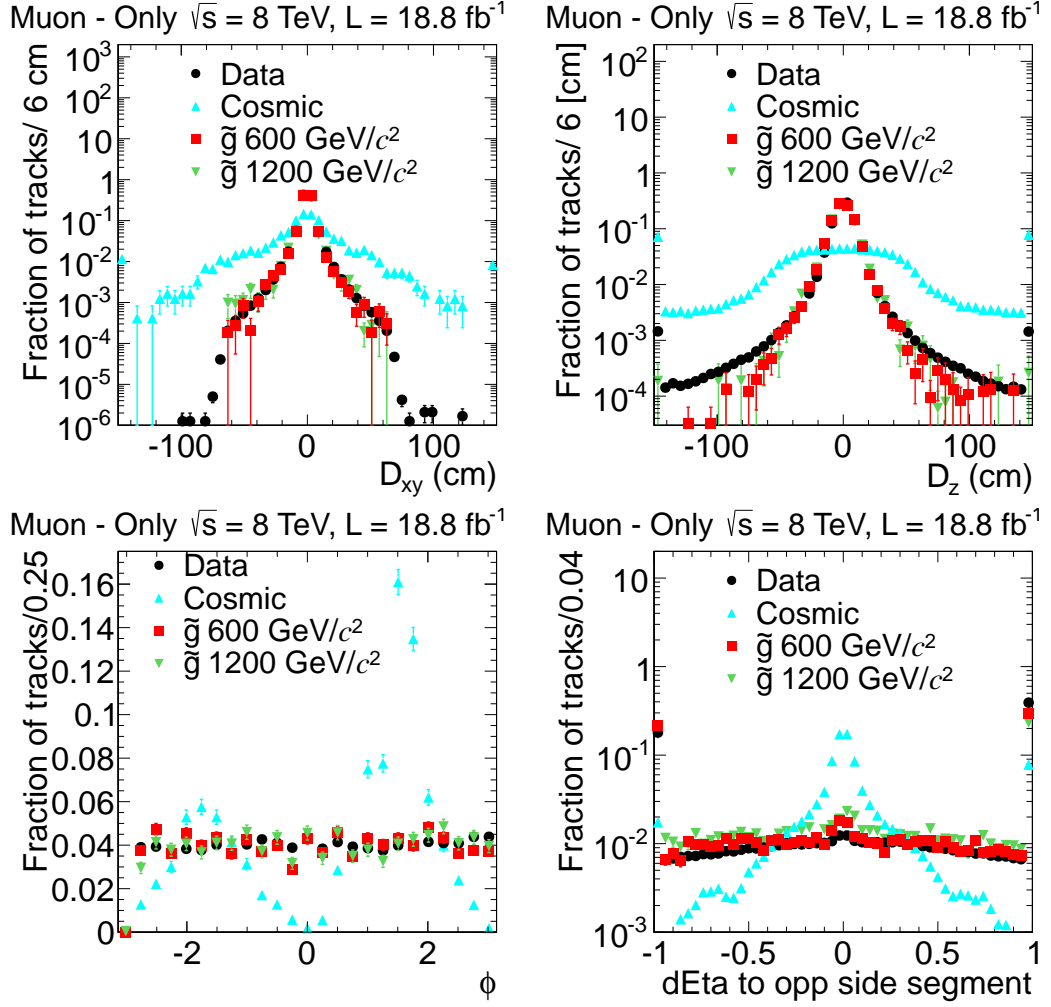
Figure 5.14: Distribution of various preselection variables in the *muon only* analysis for data, cosmic-ray muon control sample, and signal MC. Top row: Distribution of transverse (left) and longitudinal displacement (right). Bottom row: Distribution of the ϕ of the track (left) and the η separation of the track to muon segments (right). The rightmost bin in the η separation plot includes tracks where no segments were found.
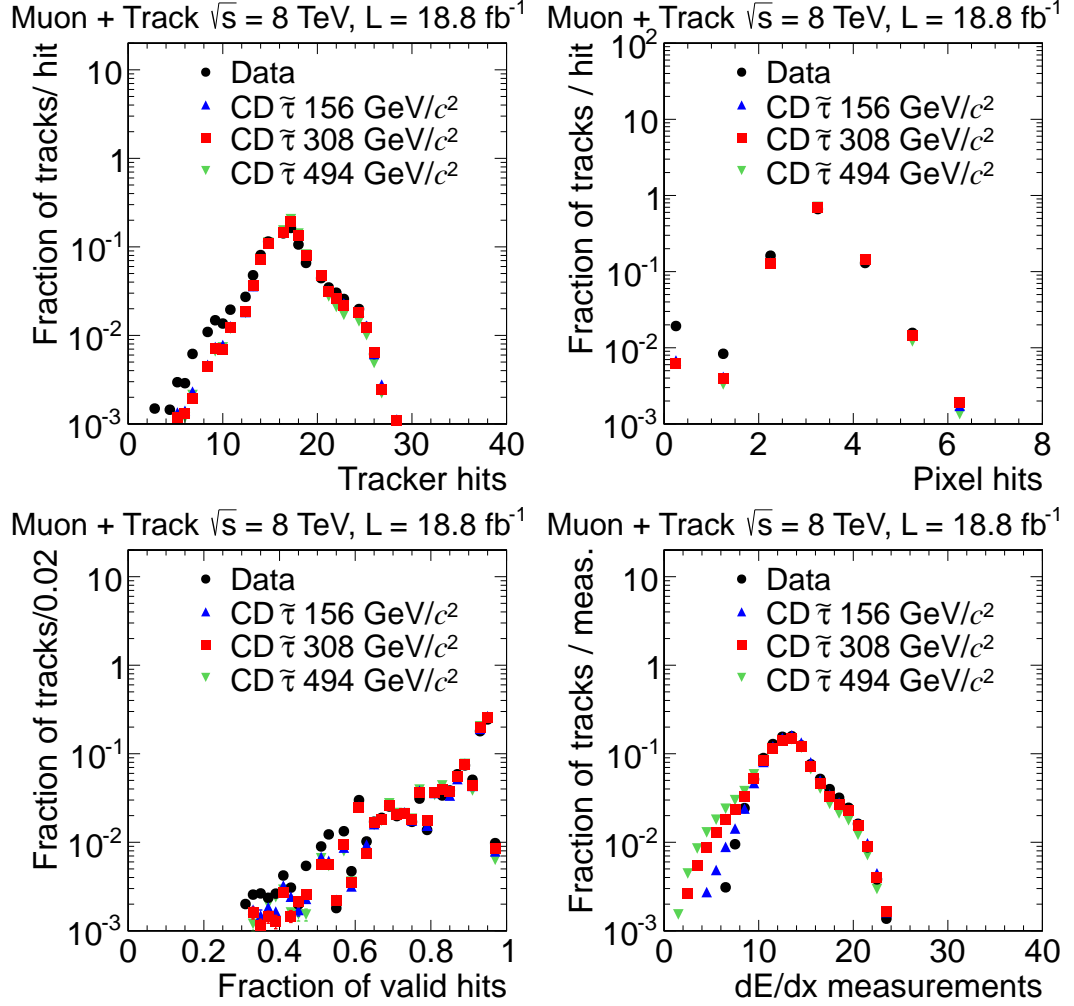
Figure 5.15: Distribution of various preselection variables in the *muon+track* analysis for data and signal MC. Top row: Number of tracker (left) and pixel (right) hits. Bottom row: Fraction of valid tracker hits (left) and number of measurements used for the *dE/dx* calculation (right).
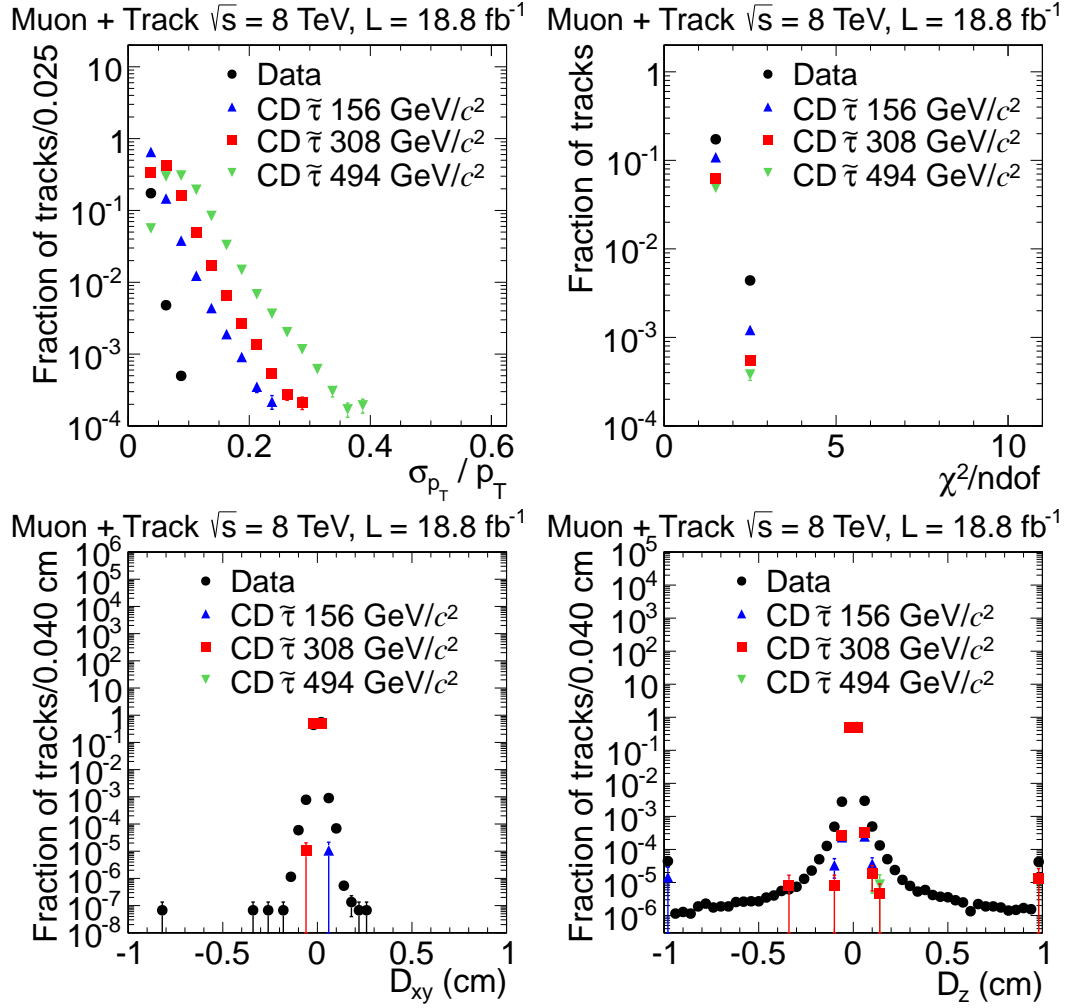
Figure 5.16: Distribution of various preselection variables in the *muon+track* analysis for data and signal MC. Top row: Relative p_T uncertainty (left) and χ^2 per degree of freedom (right). Bottom row: Displacement in the transverse (left) and longitudinal (right) directions.

Isolation cuts are also applied in the *muon+track* analysis. Isolated means that there not be high energy particles near the track. This is required to reduce the background from jets where overlapping tracks could give anomalously high dE/dx values. The isolation cuts are kept very loose as the goal is not to find isolated particles but just to reject very high energy jets. Specifically, the sum of the momentum of the tracks within 0.3 in $\eta - \phi$ space of the track (excluding the track itself) is required to be less than 50 GeV. Additionally, the ratio of the total amount of energy measured in the calorimeter within a radius of 0.3 in $\eta - \phi$ space to the track to the track momentum must be less than 0.3.

Additionally, the *muon+track* analysis uses the same cuts on the β^{-1} uncertainty and number of measurements as the *muon only* analysis. Figure 5.17 shows the isolation and β^{-1} variables for data and signal MC.

5.6.3 Preselection for *track only* and *multiple charge*

The *track only* analysis applies the same preselection as the *muon+track* analysis except the cuts on the timing measurement are not applied, as the tracks are not required to be reconstructed in the muon system.

The *multiple charge* analysis applies the same selection criteria as the *muon+track* analysis except the cut on relative isolation less than 0.3 and the cleaning of the hits used for the dE/dx calculation is not done. The cleaning procedure is not applied because the amount of charge deposited is proportional to Q^2 meaning that even a $Q = 2e$ HSCP will deposit four times as much charge as a $Q = 1e$ HSCP. As the tracker saturates for a energy loss approximately three times that expected for a MIP, many of the hits from $Q > 1e$ HSCP will be saturated; this can confuse the cleaning procedure. Additionally, as the high charge samples deposit so much charge, there will still be good signal/background separation
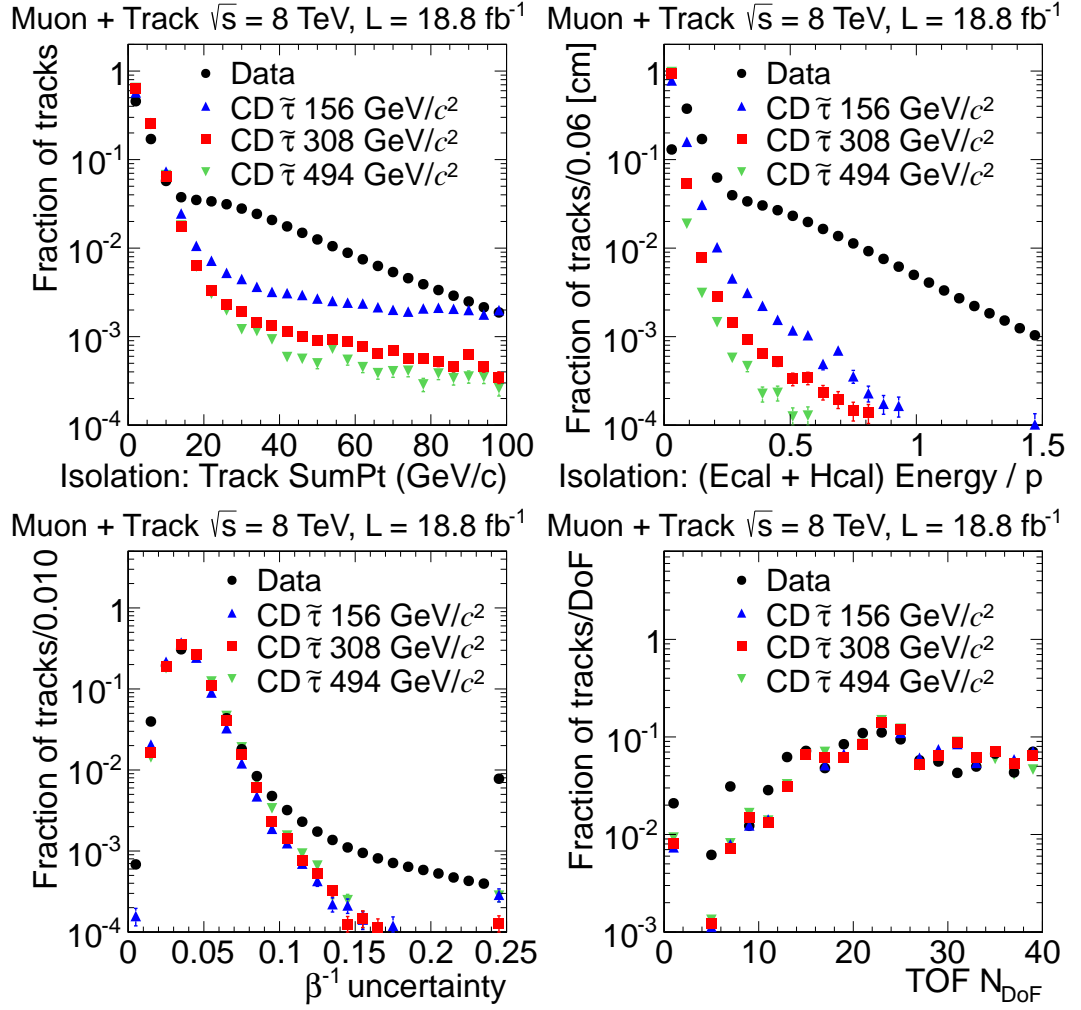
Figure 5.17: Distribution of various preselection variables in the *muon+track* analysis for data and signal MC. Top row: Sum momentum of tracks within 0.3 (left) and calorimeter energy within 0.3 divided by track momentum (right). Bottom row: Distribution of the β^{-1} measurement uncertainty (left) and the number of degrees of freedom (right).
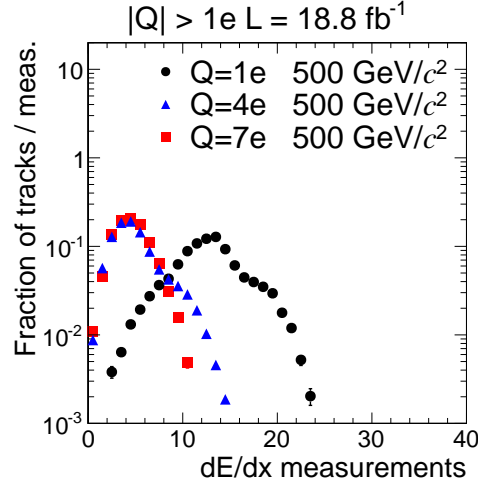
Figure 5.18: Distribution of number of dE/dx measurements passing cleaning for samples of three different charges

even with longer tails in the dE/dx distribution. Figure 5.18 shows the number of measurements passing the cleaning for multiply charged samples.

5.6.4 Summary of Preselection

The preselection criteria applied on the track in the muon system used in the *muon only*, *muon+track*, and *multiple charge* analyses are summarized in Table 5.3. The preselection criteria applied on the track in the inner tracker used in the *muon+track*, *track only*, and *multiple charge* analyses are summarized in Table 5.4.

The total preselection efficiency is shown in Tables 5.5 and 5.6 for the SUSY and modified DY samples, respectively. The efficiencies are presented with respect to HSCP reconstructed as a track in CMS. The inefficiency for the *muon only* analysis mostly arises from the cuts used to suppress the background from cosmic-ray muons. The other analyses lose efficiency due to quality requirements

Table 5.3: Summary of preselection criteria on muon system qualities used in the various analyses as defined in the text.

	muon only	*muon+track*	$|Q| > 1e$
# TOF measurements		> 7	
$\sigma_{1/\beta}$		< 0.07	
$1/\beta$		> 1	
$|\eta|$	< 2.1		$-$
p_T (GeV/c)	> 80		$-$
d_z and d_{xy} (cm)	< 15		$-$
# DT or CSC stations	> 1		$-$
Opp. segment $|\eta|$ difference	> 0.1		$-$
$|\phi|$	< 1.2 OR > 1.9		$-$
$|\delta t|$ to other beam crossing (ns)	> 5		$-$

Table 5.4: Summary of preselection criteria on the silicon tracker qualities used in the various analyses as defined in the text.

	muon+track	track only	$|Q| > 1e$
$|\eta|$		< 2.1	
p_T (GeV/c)		> 45	
d_z and d_{xy} (cm)		< 0.5	
σ_{p_T}/p_T		< 0.25	
Track χ^2/n_d		< 5	
# Pixel hits		> 1	
# Tracker hits		> 7	
Frac. Valid hits		> 0.8	
$\Sigma p_T^{trk}(\Delta R < 0.3)$ (GeV/c)		< 50	
# dE/dx measurements		> 5	
dE/dx strip shape test		yes	no
$E_{cal}(\Delta R < 0.3)/p$		< 0.3	–

Table 5.5: Preselection efficiency for a few benchmark SUSY samples in each analysis. This efficiency is with respect to the reconstructed HSCP track (i.e. muon system track for the *muon only* analysis and muon system plus inner tracker for the *muon+track* analysis). The fraction of glueballs assumed for the gluino samples is given in parentheses at the end of the signal name.

Model	*muon only*	*muon+track*	*track only*
Gluino 500 GeV (1.0)	44%	-	-
Guino 1000 GeV (1.0)	40%	-	-
Gluino 500 GeV (0.1)	44%	60%	70%
Gluino 1000 GeV (0.1)	43%	42%	51%
Gluino(CS) 500 GeV (0.1)	-	-	64%
Gluino(CS) 1000 GeV (0.1)	-	-	47%
Stop 600 GeV	48%	53%	61%
Stop (CS) GeV	56%	-	56%
CD Stau 370 GeV	-	76%	78%

on the inner track and dE/dx measurement which are necessary to constrain the background from misreconstructed tracks. Additionally, as CMS reconstruction generally assumes signatures of SM particles, HSCP tracks can have a lower quality than a SM particle would. The requirements are set trying to balance keeping the signal efficiency high while maintaining a low background contamination of the signal region.

The distributions of p_T and β^{-1} for the *muon only* analysis for data, cosmic-ray muon control sample, and various signal models is shown in Figure 5.19 after applying the preselection requirements. Figure 5.20 shows the p_T, β^{-1}, and dE/dx distributions after applying the *muon+track* preselection cuts for data

Table 5.6: Preselection efficiency for a few benchmark modified DY samples in each analysis. This efficiency is with respect to the reconstructed HSCP track (i.e. muon system plus inner track for the *multiple charge* analysis and inner track for the *track only* analysis).

Model	muon+track	track only	multiple charge
DY $Q = 1e$ 600 GeV	72%	76%	75%
DY $Q = 3e$ 600 GeV	-	-	71%
DY $Q = 5e$ 600 GeV	-	-	50%
DY $Q = 7e$ 600 GeV	-	-	37%

and various signal models.

5.6.5 Tag and Probe Studies

The study of the agreement between data and MC for numerous muon qualities is done by the Muon Physics Object Group (POG) of CMS. The group provides scale factors for correcting MC to match data. For all of the analyses except for *muon only* it is sufficient to use results obtained from this group as the muon qualities those analyses use are common within CMS. However, as the *muon only* analysis uses numerous variables which are unique to it, the results from the muon POG are not applicable to it.

For this reason, additional studies were performed to test the agreement of MC with data. The efficiency of the selections was checked with a tag-and-probe technique [19] using muons from Z boson decays. The tag-and-probe procedure proceeds by requiring one muon, the "tag" muon, be found with a stringent selection while the other muon, the "probe" muon, is required to be found with only a loose selection using only the silicon tracker. The efficiency to pass the
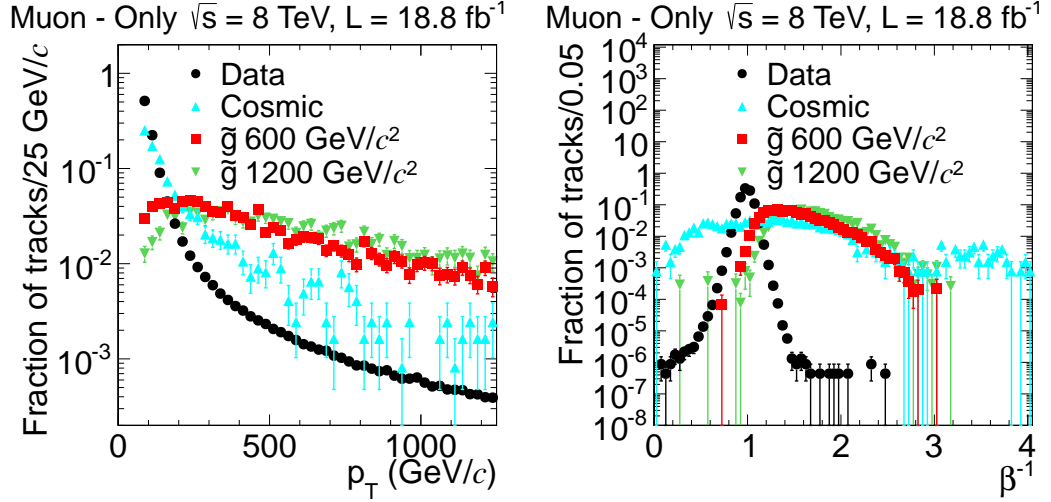
Figure 5.19: Distribution of selection variables for data, cosmic-ray muon control sample, and signal MC. Left: Distribution of p_T. Right: Distribution of β^{-1}.

preselection in the *muon only* analysis can then be estimated as the fraction of of the probes that pass the preselection. The background from processes other than Z bosons is small and is subtracted by a simultaneous fit to the tag-probe invariant mass distributions of signal and background around the Z boson mass. The efficiency estimated in data is compared with that found in MC. Scale factors are used to correct MC for any discrepancy observed between the efficiencies. The MC sample used does not contain any production from background processes.

The tag muon is required to pass a tight selection recommended by the Muon POG and to match to an object that triggered the read out of CMS. The last requirement assures that no bias is introduced in the efficiency measurement by the need for the event to have been read out. Additionally, the tag must pass the requirements of a skim that was used to reduce the data size to a level making processing reasonable. The skim requirements are at least three dE/dx measurements and $I_h > 3.0$ or $I_h < 2.8$.
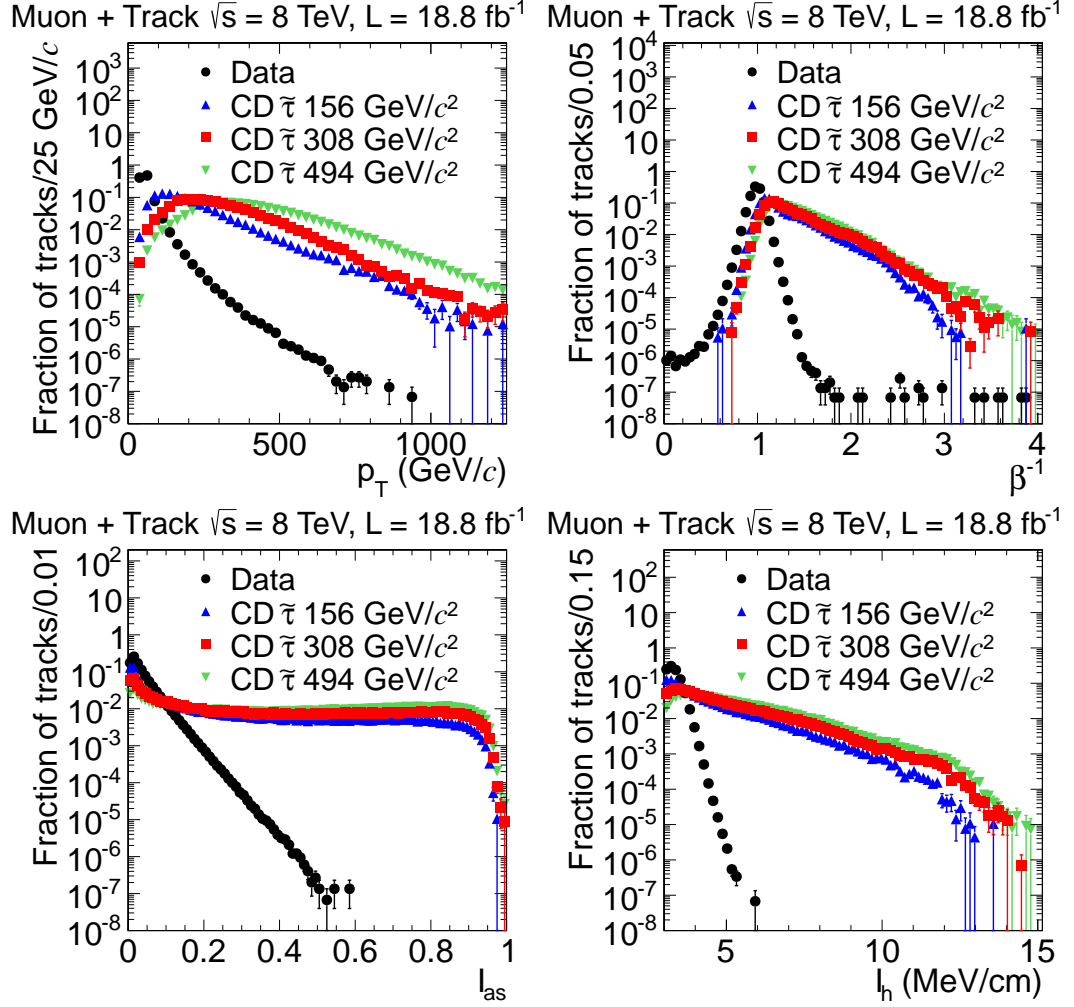
Figure 5.20: Distribution of section variables for data and signal MC. Top row: Distribution of p_T (left) and β^{-1} (right). Bottom row: Distribution of I_{as} (left) and I_h (right).

A set of probe candidates is defined as tracks reconstructed in the inner tracker with no requirement of muon system activity. The probes are required to have $p_T > 40$ GeV, $|\eta| < 2.1$, and the opposite charge of the tag muon. The invariant mass of the tag-probe pair is then required to be within 10 GeV of the mass of the Z boson, 91 GeV. The invariant mass distribution of the tag-probe pairs is fit using the sum of two Voigtians (the convolution of a Lorentzian and a Gaussian) to represent the signal and an exponential for the background.

Figure 5.21 shows the efficiency for the probes to pass the preselection, except for the selection on p_T, against the probe p_T, η, and the number of primary vertices in the event. Overall the efficiency is approximately 75% in data and 80% in MC. The efficiency is mostly flat versus p_T and number of vertices but does depend on η. MC is scaled by an η dependent scale factor to correct for the discrepancy.

5.7   Background Predictions

All of the analyses count the number of tracks passing threshold values on some grouping of the p_T, β^{-1}, and I_{as} variables. The *muon+track* and *track only* analyses also place a requirement on the mass of the track as described below. There are two sources of background considered in the analyses.

The first is muons, or for the *track only* analysis any charged SM particle, from the collisions in the LHC. Muons can pass the thresholds on the selection variables for a variety of reasons. All muons at the LHC will be traveling at very nearly the speed of light, but finite detector resolution results in a smearing of the measured time of hits. This can cause muons to have a high measured β^{-1}. While muons in the momentum region of interest all deposit approximately
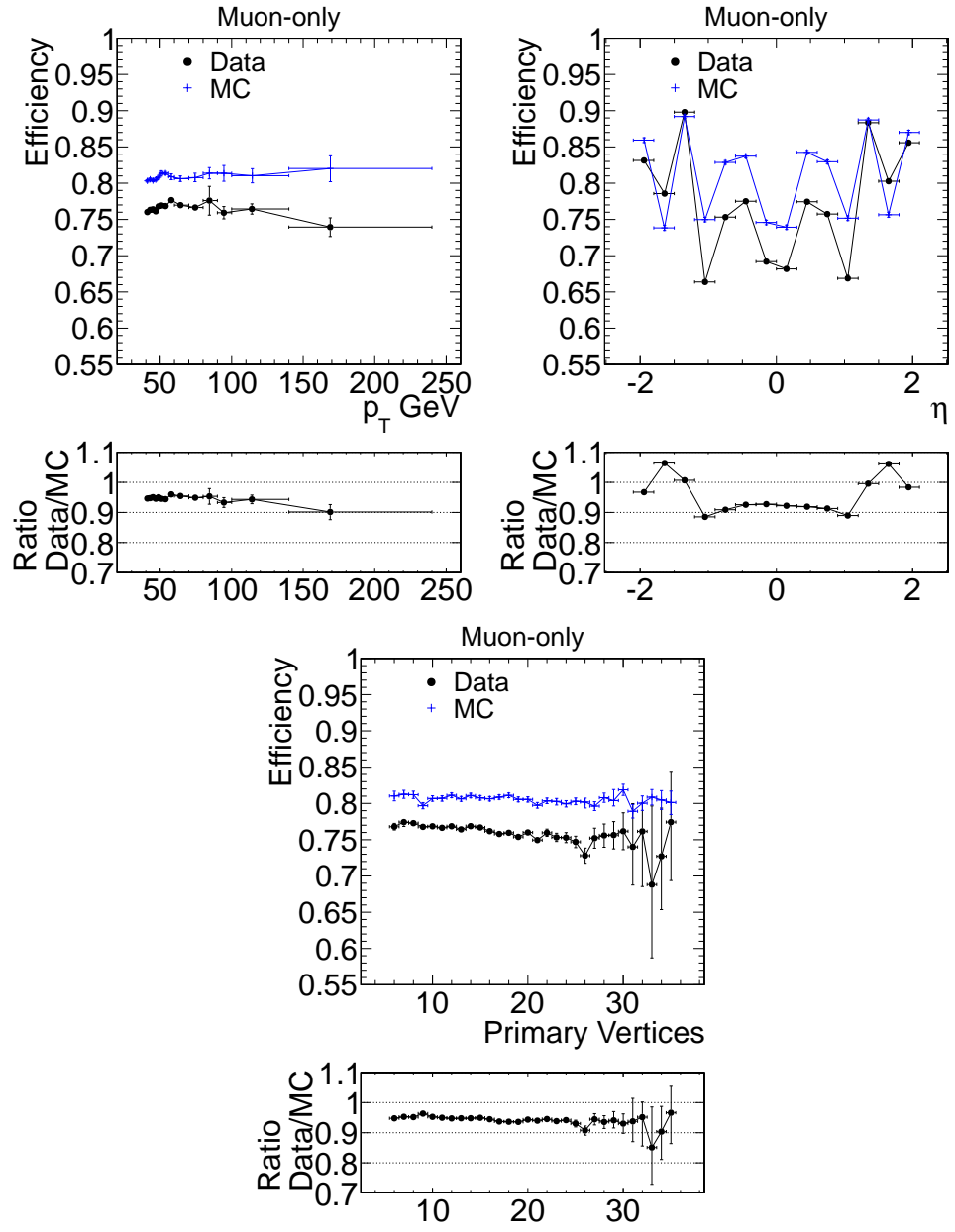
Figure 5.21: Efficiency to pass preselection cuts for the *muon only* analysis. Top row: As a function of p_T (left) and η (right) Bottom row: As a function of number of primary vertices.

the same amount of energy in the tracker on average, the amount deposited in each interaction is subject to large variations. This can lead to muons with a high dE/dx value. Detector resolution can also contribute to muons with high dE/dx. Additionally, collision muons can have large reconstructed momentum, either due to true high momentum or detector mismeasurement promoting a low momentum muon to a high reconstructed momentum. Detector mismeasurement is especially important for the momentum measured in the muon system.

Collision muons are predicted exploiting the lack of correlation between the selection variables for muons through the $ABCD$ method. In the $ABCD$ method, multiple bins are defined by whether the track passes thresholds on the selection variables. In the normal two dimensional version of the $ABCD$ method, two selection variables are used and four regions are defined. The A region has tracks failing both of the thresholds on the selection variables, B (C) fails only the threshold on the first (second) of the selection variables. The signal region, D, passes the threshold on both selection variables. The number of background muons in the D region can be predicted as $B \times C/A$, where the letters represent the number of tracks in the regions. This prediction holds as long as the probability for a background muon to pass the threshold on one of the variables is independent of whether it passes the threshold of the other. Tests of the correlation between the selection variables are given below.

The four different analyses use different combinations of the selection variables defined in Sec. 5.5. With three different selection variables (p_T, β^{-1}, dE/dx), eight different bins are defined. In order to simplify the nomenclature in this section, Table 5.7 defines the names of the bins (ranging from A-H) and whether they pass or fail the thresholds on the selection variables. For all the selection variables passing means having a value above the threshold. If a selection variable

is not used in an analysis then it is taken to have passed.

Only the *muon+track* analysis applies a threshold on all three selection variables and as such is the only one to use all eight bins. An extended three-dimensional version of the $ABCD$ method is then used to make the prediction as is described in the *muon+track* subsection below. The other three analyses use only the four bins where the unused variable is said to have passed. These analyses use the traditional two-dimensional $ABCD$ method though the names of the bins may be different. For all the analyses the D region is always the signal region.

In order to perform systematic studies, the analyses that use β^{-1} reverse the preselection requirement on β^{-1} greater than one. This creates a group of tracks measured as going faster than the speed of light, making it signal free. As the β^{-1} distribution is close to symmetrical for background muons this makes the region very good for testing the background prediction. New bins are defined as in Table 5.7 but now β^{-1} is said to have passed if the value is below the threshold. The bins are referred to with a prime to denote that they are from the control region, so the new "signal" region would be referred to as D'.

The second source of background, important only for the *muon only* analysis, is muons from cosmic-rays. As discussed in Section 2.2 muons from cosmic-rays are constantly passing through CMS. Cosmic-ray muons will arrive to the muon system asynchronously with collisions in the LHC. Depending on exactly when the cosmic-ray muon arrives in the muon system relative to collisions in the LHC this can give rise to a particle with a large β^{-1} measurement. Out of time particles are not centered in the tracker's charge collection window giving them lower dE/dx. This combined with the impact parameter requirements applied at preselection makes cosmic-ray muons negligible for the analyses looking for

Table 5.7: Bin naming convention. The signal region is always the D region.

Name	p_T	β^{-1}	dE/dx
A	Fail	Fail	Pass
B	Fail	Pass	Pass
C	Pass	Fail	Pass
D	Pass	Pass	Pass
E	Fail	Fail	Fail
F	Fail	Pass	Fail
G	Pass	Fail	Fail
H	Pass	Pass	Fail

high dE/dx in the tracker. The distribution of p_T for cosmic-ray muons falls off at high momentum slower than for collision muons, as evidenced in Figure 5.19 (left). As cosmic-ray muons have different β^{-1}, p_T, and dE/dx distributions than collision muons they will not be accurately predicted with the same method used to predict the collision muon background in the *muon only* analysis. A dedicated method using the cosmic-ray muon control sample is described below.

For all the analyses, the expected background in the signal region is estimated by multiple different predictions. The details on how the different predictions are found for each analysis are given in the corresponding subsection below. The spread of the different background predictions can be used to estimate the systematic uncertainty for each analysis.

The following variables are defined:

$$S_N^{syst+stat} = \sqrt{\sum_i \left(x_i - \langle x \rangle\right)^2 / (N-1)}$$

$$S_N^{stat} = \sqrt{\sum_i \left(\sigma_i\right)^2 / N} \tag{5.5}$$

$$S^{syst} = \sqrt{S_{syst+stat}^2 - S_{stat}^2}$$

where N is the number of background estimates made, the sum is over N, x_i is the value of the ith background estimate, and σ_i is the statistical uncertainty on the ith background estimate. The first quantity is an estimator of the standard deviation of the background estimates, which takes both statistical and systematic contributions. The second quantity is adopted as an estimator of the contribution of the statistical uncertainties to the standard deviation. Finally, the last equation gives the systematic uncertainty on the background prediction assuming the statistical and systematic uncertainties add in quadrature to give the standard deviation.

5.7.1 Prediction for *muon only* analysis

The collision muon background in the *muon only* analysis is predicted with the selection criteria of β^{-1} and p_T in the $ABCD$ method. The expected number of background tracks in the signal region D (see Table 5.7) is predicted as $B \times C/A$.

The $ABCD$ method only works if the probability to pass one of the thresholds is independent of the other variable. However, it has been observed that a correlation exists between the p_T and β^{-1} measurements based on whether the track is in the barrel or forward region of the detector as well as the number of DT or CSC stations containing valid hits. Six bins are created defined by the η of the track, greater or less than 0.9; and the number of stations, 2, 3, or 4. The
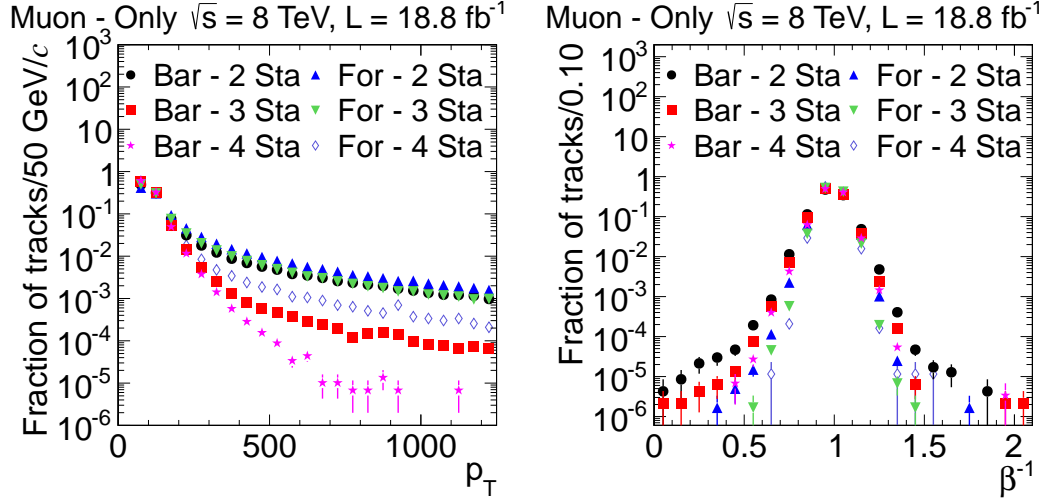
Figure 5.22: Distribution of p_T and β^{-1} for data for six different regions depending on whether the track is in the barrel (Bar) or forward (For) region of CMS and number of muon stations (Sta) used in the fit.

distributions of p_T and β^{-1} in the six regions is shown in Figure 5.22. The predicted number of tracks in each bin is predicted separately and the total number of predicted background tracks is the sum of the six predictions.

After the binning the correlation is small enough not to bias the background prediction as can be seen in Figs. 5.23 and 5.24.

To predict the cosmic-ray muon background, sidebands in the $|\delta_z|$ distribution and the pure cosmic-ray muon sample (see Section 5.3) are used. The number of tracks, N, in a sideband region of $|\delta_z|$ are counted. The tracks are required to pass the full selection except the $|\delta_z|$ requirement is changed from $0 < |\delta_z| < 15$ cm to $70 < |\delta_z| < 120$ cm and the requirements on ϕ, segment η separation, and p_T are removed to increase the number of cosmic-ray muons in the sideband region. Additionally the tracks are required not to be reconstructed in the silicon tracker to decrease the contamination from collision muons. Then, the pure cosmic-ray
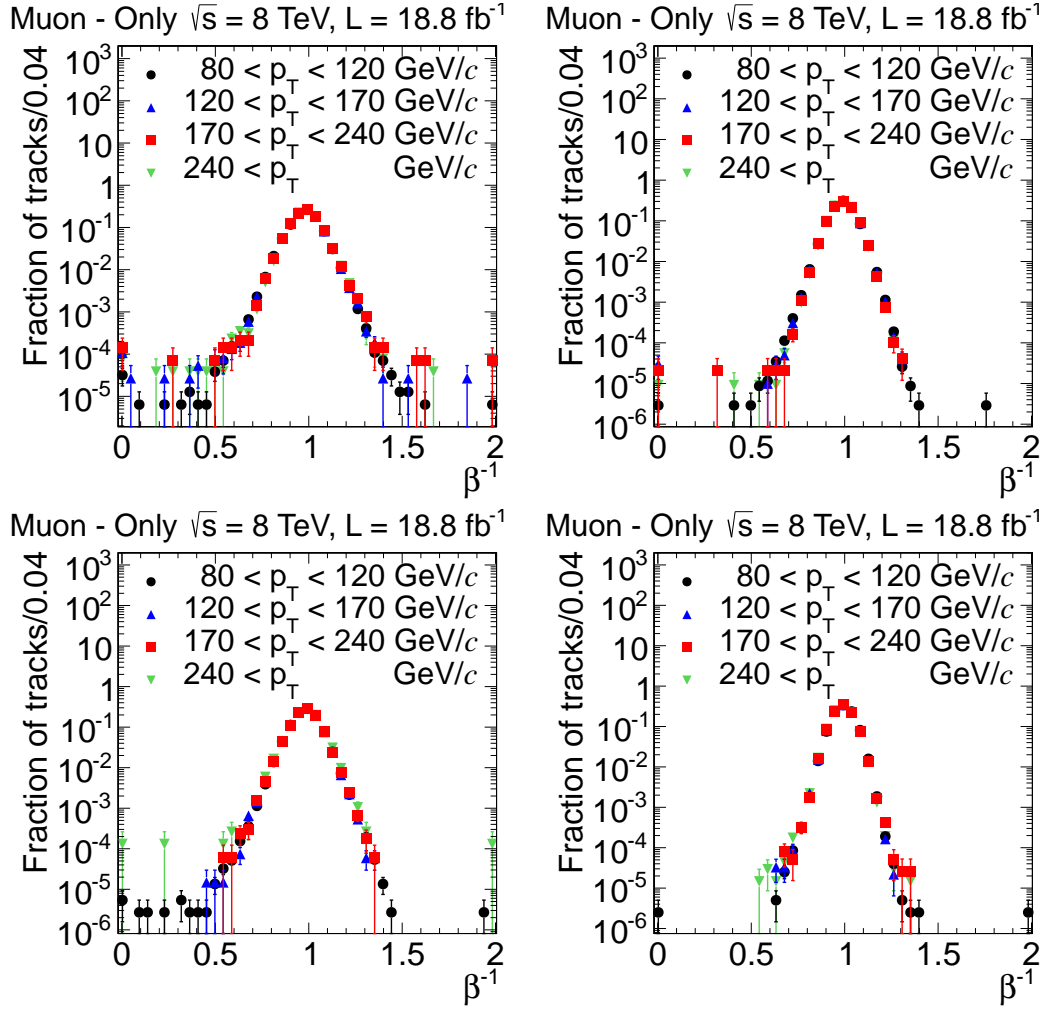
Figure 5.23: Distribution of β^{-1} for different momentum regions for four of the six different bins that are used to make the prediction. The left column shows the barrel region while the right column shows the forward region. The top (bottom) row are for 2 (3) stations.
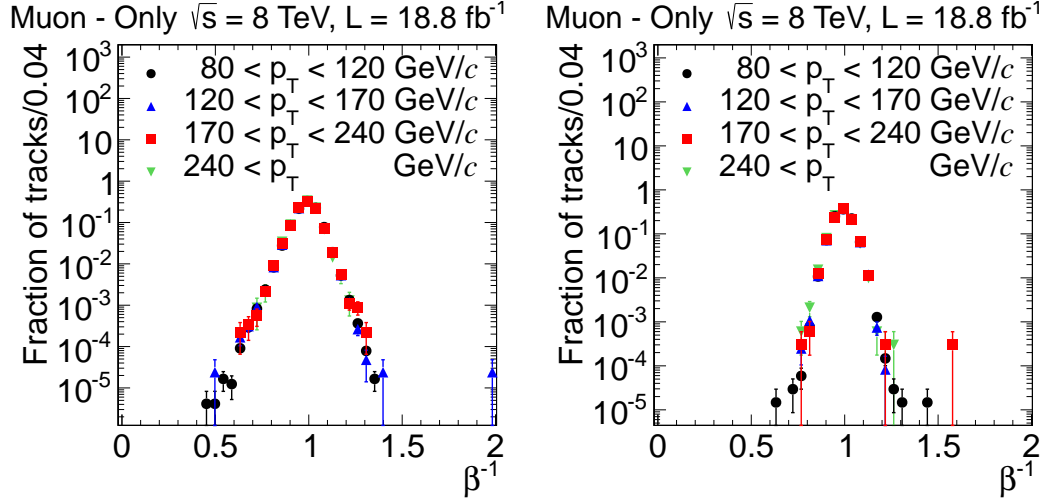
Figure 5.24: Distribution of β^{-1} for different momentum regions for four station tracks. The left column shows the barrel region while the right column shows the forward region.

sample is used to calculate the ratio, R, of tracks in the $|\delta_z|$ sideband region relative to the signal region with the same offline requirements as in the main data sample.

The number of cosmic-ray muons passing the final selection in the main data sample can then be predicted as

$$P_{Cosmic} = N \times R. \tag{5.6}$$

Numerous effects cancel in this ratio making the prediction robust. The number of cosmic-ray muons in any of the regions can be expressed as $C = F \times T \times \epsilon$, where C is the number of cosmic-ray muons observed, F is the flux of cosmic-ray muons per second, T is the amount of time that CMS was collecting data, and ϵ is the efficiency of the detector to reconstruct and select cosmic-ray muons in the region including detector acceptance effects.

The number of cosmic-ray muons expected in the signal region can be written as

$$P_{Cosmic} = F \times T_{Main} \times \epsilon_{Main}^{Signal} \tag{5.7}$$

and the number N in the sideband region as

$$N = F \times T_{Main} \times \epsilon_{Main}^{Sideband} \tag{5.8}$$

with Main referring to the samples gathered with the main analysis triggers and Signal and Sideband representing the $|d_z|$ signal and sideband regions, respectively. The ratio R can be expressed as

$$R = F \times T_{Control} \times \epsilon_{Control}^{Signal}/(F \times T_{Control} \times \epsilon_{Control}^{Sideband}) = \epsilon_{Control}^{Signal}/\epsilon_{Control}^{Sideband} \tag{5.9}$$

where Control refers to the pure cosmic-ray muon control sample.

Putting this all together and canceling numerous factors, it can be seen that Eq. 5.6 holds so long as the relationship

$$\epsilon_{Main}^{Signal}/\epsilon_{Main}^{Sideband} = \epsilon_{Control}^{Signal}/\epsilon_{Control}^{Sideband} \tag{5.10}$$

is accurate. The only difference between the two ratios is that one is using events collected with the main triggers while the other is using the cosmic-ray muon control trigger. As the offline requirements on tracks reinforce the trigger selection the relationship is likely to hold. Thus the prediction of the number of cosmic-ray muons in the signal region should be robust. Note that the relationship does not require the efficiency in the cosmic-ray muon control sample to be the same as in the main sample. Only that the ratio of the efficiencies in the signal and sideband regions be the same in the two samples.

As previously mentioned, the background prediction is checked using tracks with β^{-1} less than one. This region is useful as it is background dominated and
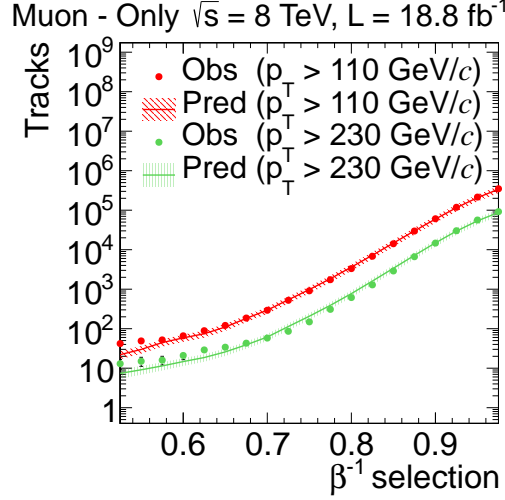
Figure 5.25: Number of predicted and observed tracks passing thresholds on p_T and β^{-1}. The tracks are required to be above the p_T threshold and below the β^{-1} threshold. Two representative p_T thresholds are shown. Threshold for β^{-1} set by x-axis. Figure is cumulative as tracks passing the selection with tight thresholds will also pass for loose thresholds.

provides a good approximation of background tracks in the signal region as the β^{-1} distribution is roughly symmetrical about one for background tracks. The background prediction procedure described above is repeated but instead looking for high p_T tracks with β^{-1} below some threshold. This is the same procedure that would be taken if looking for particles that travel faster than the speed of light. As described above, the bins in the low β^{-1} region are given a prime so the number of tracks in the "signal" region D' can be predicted as $C' \times B'/A'$. Figure 5.25 shows the number of predicted and observed number of tracks in D' for different p_T and β^{-1} thresholds. Good agreement is seen between the observed and predicted number of tracks.

To determine the systematic uncertainty on the predicted collision background, the β^{-1} less than one region is used once again. The predicted number
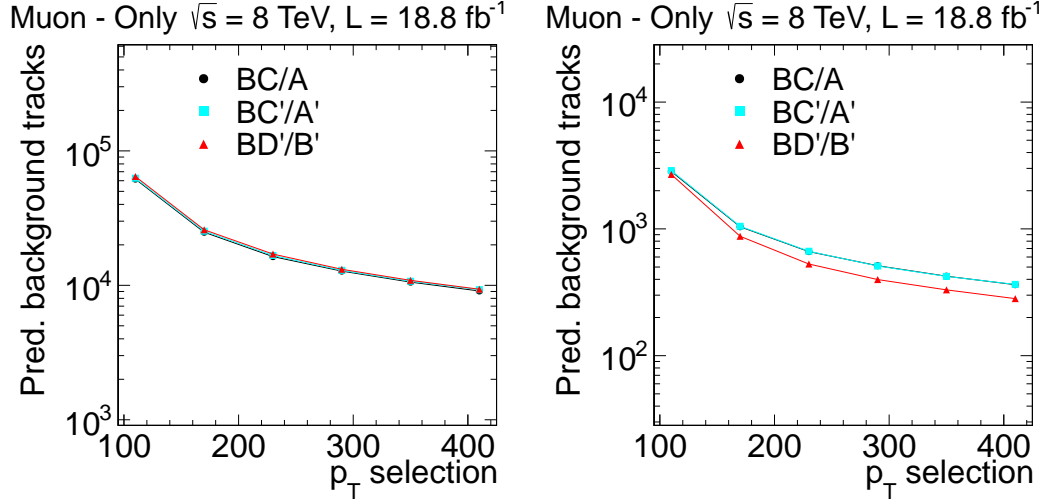
Figure 5.26: Distributions of the number of predicted tracks and their statistical uncertainty with different prediction formulae for different set of thresholds. The p_T threshold is defined by the x-axis. Figures are cumulative as tracks passing the selection with tight thresholds will also pass for loose thresholds. Left: $1/\beta > 1.1$ (< 0.9 for low $1/\beta$ regions). Right: $1/\beta > 1.2$ (< 0.8 for low $1/\beta$ regions).

of tracks in the signal region D can be predicted by three different formulae, the main one of $B \times C/A$ as well as $B \times C'/A'$ and $B \times D'/B'$. The B region contains tracks with β^{-1} above the final selection threshold and p_T below its threshold. The ratios C/A, C'/A', and D'/B' give the fraction of tracks to be above the threshold on p_T in the region with β^{-1} between one and the final threshold; the region with β^{-1} between a value less than one, for example 0.8, and one; and the region with β^{-1} below the same less than one value, respectively. Thus the different predictions can be used to evaluate how the fraction of background tracks to pass the p_T threshold depends on their β^{-1}. Figure 5.26 shows the number of predicted tracks from the three predictions for different β^{-1} and p_T thresholds.

The systematic uncertainty is extracted from the three predictions through

Table 5.8: Predicted numbers of cosmic-ray muon tracks for the *muon only* analysis.

$|d_z|$ Region	Prediction
$30 < |dz| < 50$ cm	3.1 ± 0.5
$50 < |dz| < 70$ cm	2.6 ± 0.7
$70 < |dz| < 120$ cm	3.2 ± 1.0
120 cm $< |dz|$	3.8 ± 0.7

Eq. 5.5 with N=3. Fig. 5.27 shows the variation of $S_{syst+stat}/\langle x \rangle$, $S_{stat}/\langle x \rangle$ and $S_{syst}/\langle x \rangle$ as a function of the p_T threshold. The statistical uncertainty due to the number of tracks in the B group is not subtracted as it is completely correlated between the three predictions. From the last plot the systematic uncertainty on the expected background in the signal region is estimated to be 20%.

The systematic uncertainty on the cosmic-ray muon background is determined by modifying the d_z range used to define the control sample. Predictions can also be made from tracks with $30 < |d_z| < 50$ cm, $50 < |d_z| < 70$ cm, and 120 cm $< |d_z|$. Table 5.8 shows the number of predicted cosmic-ray muons for each $|d_z|$ region using the final selection defined in Section 5.9 The statistical uncertainty from the number of tracks in the signal region in the pure cosmic-ray muon sample is not included in the uncertainties listed as it is correlated between the three predictions. Equation 5.5 with N=4 is used to calculate the systematic uncertainty. The relative systematic uncertainty is found to be 80%.

5.7.2 Prediction for *muon+track* analysis

The *muon+track* analysis uses three selection variables, p_T, β^{-1}, and I_{as}. With three selection variables an extended three dimensional version of the $ABCD$
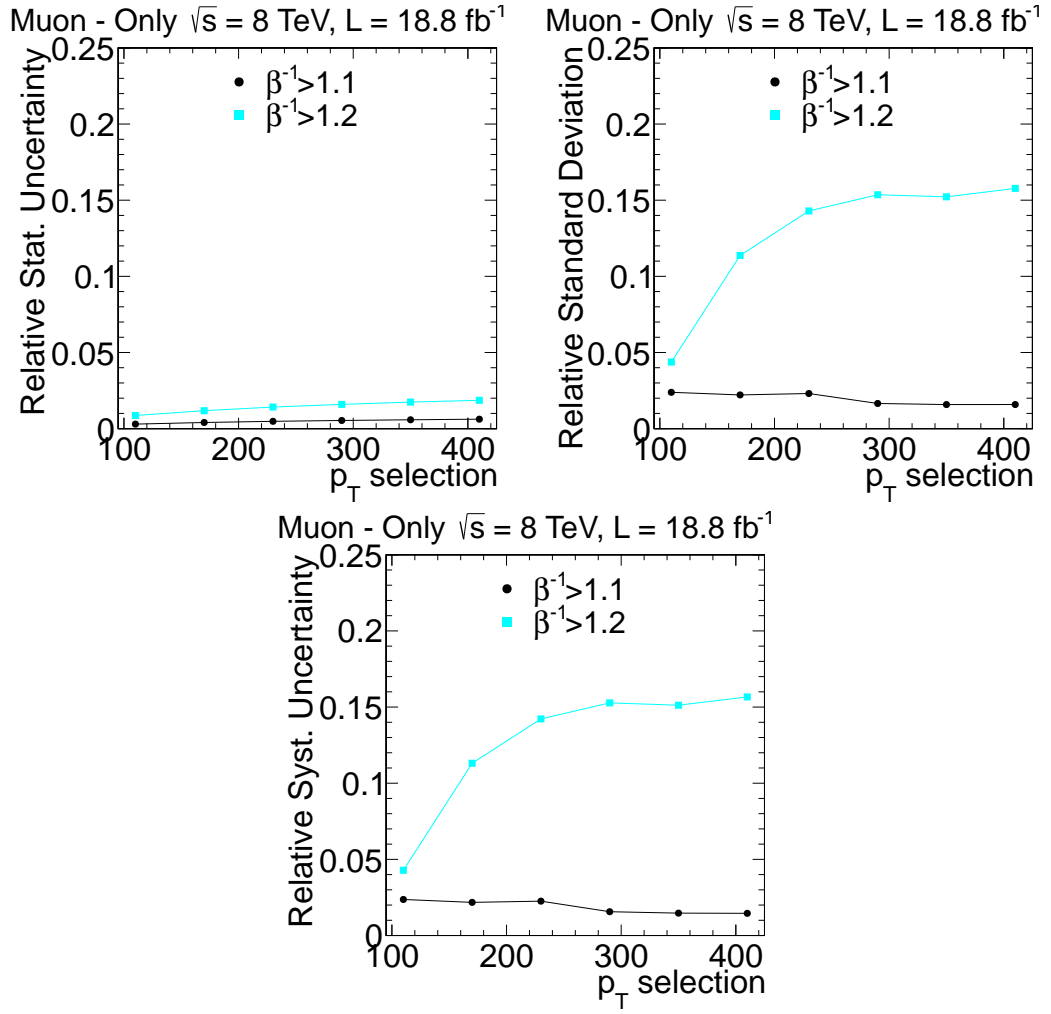
Figure 5.27: Calculation of uncertainty in the *muon only* analysis. Top left: Ratio of the square root of the quadratic mean of the statistical (stat.) uncertainties of the three possible background estimations to the mean of these estimations vs the p_T selection. Top right: Ratio of the standard deviation to the mean of the three background estimations vs the p_T selection. Bottom: Ratio of the square root of the difference between the variance and the quadratic mean of the statistical uncertainties of the three possible background estimations and the mean vs the p_T selection, taken as an estimate of the relative systematic (syst) uncertainty.

method is used to predict the collision muon background. An additional requirement on the reconstructed mass of the track is also applied and the prediction of the background mass spectrum is described below. For each signal point, the reconstructed mass of tracks must be above the average reconstructed mass of the signal minus two sigma of the mass distribution (both determined from MC) and below 2 TeV. As discussed above, the cosmic-ray muon background is negligible for the *muon+track* analysis.

To test if the selection variables are uncorrelated, the distribution of one of the variables is plotted for numerous ranges of one of the other variables. If the variables are uncorrelated then the distributions should all be the same. The distributions are shown in Fig. 5.28 and the variables are found to be sufficiently uncorrelated.

Since the *muon+track* analysis employs three selection variables it uses all eight bins defined in Table 5.7. With eight bins, the number of predicted tracks in the signal region, D, can be found via seven different equations utilizing the various bins. The predictions can be divided into three groups characterized by the amount of statistical uncertainty they have. The prediction $A \times F \times G/E^2$ has the smallest statistical uncertainty as it uses only the bins with at most one of the selection thresholds being passed. For this reason it is selected to determine the background estimate in the search. The predictions $A \times H/E$, $G \times B/E$, and $F \times C/E$ all use one of the bins where two of the thresholds have been passed. This results in them having a slightly larger statistical unceretainty (approximately a factor of 2–5 depending on the thresholds used). These predictions are used to determine the systematic uncertainty on the background prediction. The predictions $H \times C/G$, $C \times B/A$, and $H \times B/F$ include two of the bins that have tracks passing two of the thresholds giving it a much larger statistical uncertainty
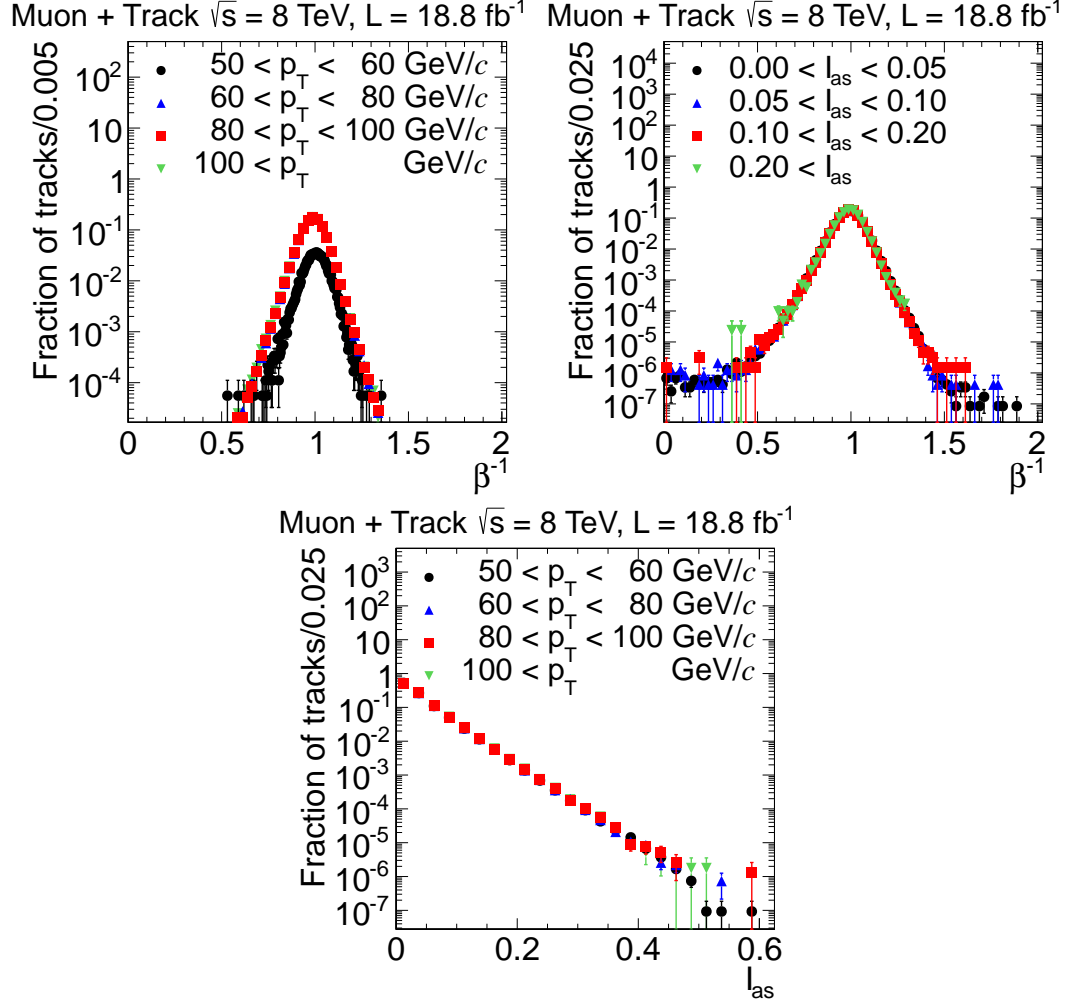
Figure 5.28: Top row: Measured β^{-1} distributions for several momentum ranges (left) and I_{as} ranges (right). Bottom row: Measured I_{as} distributions for several momentum ranges.
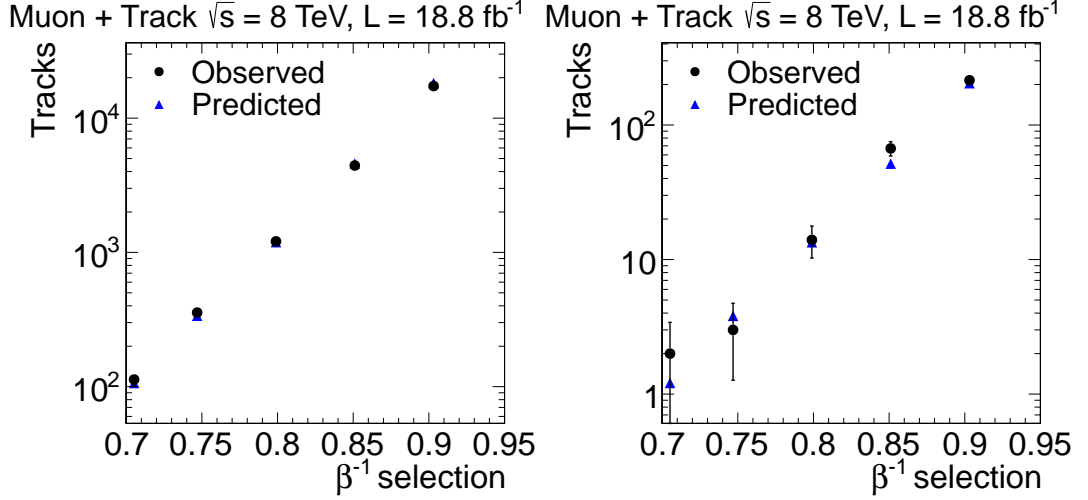
Figure 5.29: Number of observed and predicted tracks and their statistical error in the D' region for $p_T > 55, I_{as} > 0.1$ (left) and $p_T > 85, I_{as} > 0.2$ (right). Threshold on $1/\beta$ defined by the x-axis in the *muon+track* analysis. Figures are cumulative as tracks passing the selection with tight thresholds will also pass for loose thresholds.

(factor of ten larger). These predictions are not used in the analysis.

As with the *muon only* analysis the prediction is checked with tracks in the β^{-1} less than one region. Again the predicted number of tracks in D' is estimated following the same procedure as for the signal region except changing the β^{-1} requirement to be lower than some threshold, i.e. $D' = A' \times F' \times G'/E'^2$ Figure 5.29 shows the predicted and observed number of tracks in the D' region for various thresholds. Good agreement is seen even with a tight selection.

In addition to the requirements on the selection variables, the *muon+track* analysis also applies a requirement on the estimated mass of the track as determined from Equation 5.4. In order to do this the mass spectrum of background tracks in the signal region must be predicted. The background mass spectrum

is predicted using the dE/dx and momentum distributions taken from control regions. While the signal region is defined by thresholds on I_{as} and p_T (as well as β^{-1}), the mass prediction uses I_h and p so it is these distributions that must be taken from the control regions.

It has been found that the probability for background tracks to pass the threshold on I_{as} is dependent on the η of the track. The probability to pass the β^{-1} threshold has a small η dependence while the probability to pass the p_T threshold has almost no η dependence. These effects can be seen in Figure 5.30 which shows the η distribution of tracks which pass or fail the various thresholds.

This is found to have only a small effect on the total number of predicted tracks but does bias the predicted mass spectrum which uses p instead of p_T. The p_T distribution of background tracks is roughly the same for different values of η however this implies that the p distribution does vary, as momentum can be written as a function of only p_T and η. To correct for this a reweighting procedure is done such that the tracks used to determine the p distribution match the η distribution of tracks used to obtain the I_h distribution.

The $p\,(I_h)$ distribution is taken from the $G\,(A)$ region where only the $p_T\,(I_{as})$, value is above threshold and the other two are below. The mass distribution is then predicted by performing approximately 100 pseudo-experiments. The ith pseudo-experiment is done through multiple steps. First a value of E_i, F_i, is drawn from a Poisson distribution with a mean equal to the observed number of tracks in the E, F, regions in data. Next, a binned distribution of the p of tracks in the G region is employed. A value of n_{ij}, where j represents the bin of the p distribution, is drawn for each p bin from a Poisson distribution with mean equal to the number of tracks observed in that bin in data. A value of G_i is then found as the sum over j of the n_{ij}. A similar procedure is done in the
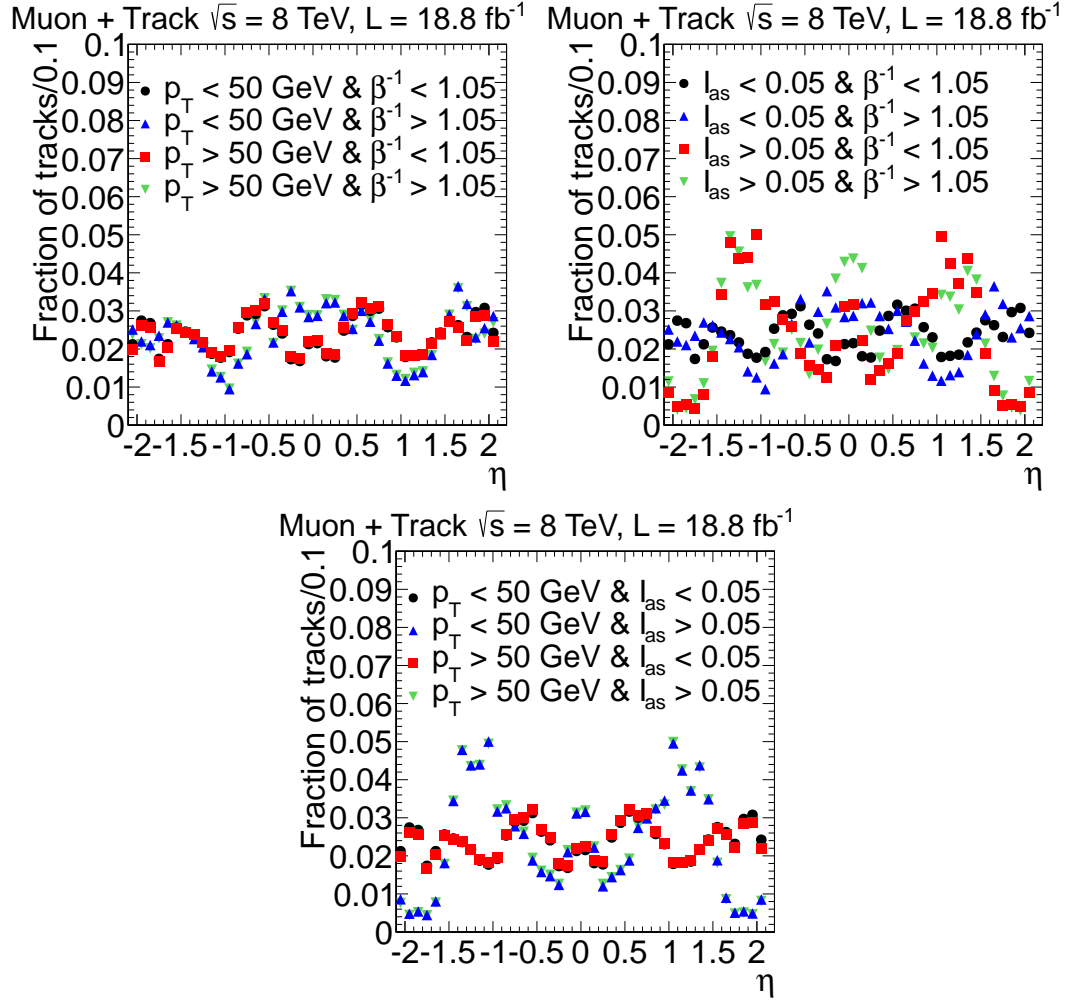
Figure 5.30: Distribution for data of the track η for various combinations of being above or below selection thresholds of 50 GeV for p_T, 1.05 for β^{-1}, and 0.05 for I_{as}. Top left: Combinations of flipping p_T and β^{-1} thresholds. Top Right: Combinations of flipping β^{-1} and I_{as} thresholds. Bottom: Combinations of flipping p_T and I_{as} thresholds. For all plots the variable not flipped is required to be below the threshold.

A region for determining the I_h distribution. Before the distribution is found, weight factors are attached to all of the tracks in the A region so that the η distribution of tracks in the A region matches that observed in the G region as necessitated by the conversation above. Next, a value of m_{ik} is found for each bin of the reweighted I_h distribution. A value of A_i is then found by summing m_{ik} over k. The predicted number of background tracks in the signal region for a given j–k bin in the $p - dE/dx$ plane, D_{ijk}, is then found via the relation

$$D_{ijk} = (A_i \times F_i \times G_i/E_i^2) \times (n_{ij}/G_i) \times (m_{ik}/A_i) = F_i \times n_{ij} \times m_{ik}/E_i^2 \quad (5.11)$$

The predicted tracks in D_{ijk} are taken to have a mass equal to the mass coming from Equation 5.4 with the p and I_h values determined by the bin that j and k represent in the p and I_h distributions, respectively. The mass distribution for the ith pseudo-experiment is then found by summing D_{ijk}, with its representative mass, over j and k.

The value in each mass bin is then found as the average of the value in all the pseudo-experiments. The statistical error is taken as the standard deviation of the values from the pseudo-experiments.

As the β^{-1} value of tracks is not currently used in the mass estimation the predicted and observed mass spectrums in the $\beta^{-1} < 1$ region can be found by only changing the groups that the tracks be drawn from be the regions with a prime (e.g. A'). Using the $\beta^{-1} < 1$ region allows for checking the predicted mass distribution in a background dominated region even when applying tight thresholds. The predicted and observed mass distributions are shown in Figure 5.31 with both loose and tight thresholds on the selection variables.

The systematic uncertainty on the background prediction for the *muon+track*
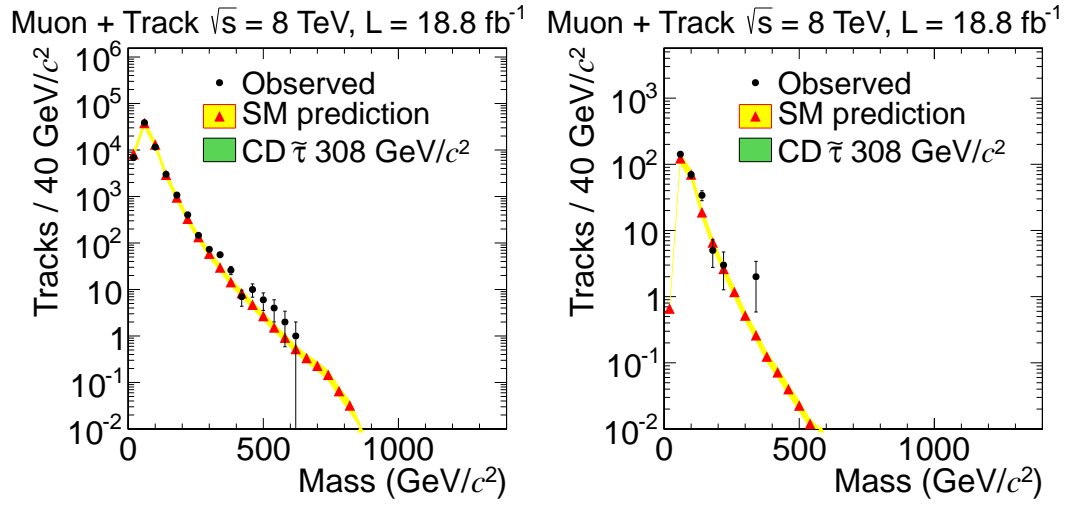
Figure 5.31: Observed and predicted mass spectrum for tracks in the D' region in the *muon+track* analysis. Left: Thresholds of $p_T > 55$ GeV, $I_{as} > 0.1$ and $1/\beta < 0.95$. Right: Thresholds of $p_T > 85$ GeV, $I_{as} > 0.1$ and $1/\beta < 0.8$. The error bands are only statistical.

analysis is evaluated by using the multiple different predictions possible when using the three dimensional variation of the $ABCD$ method. As mentioned above, in addition to the chosen prediction of $A \times F \times G/E^2$, there are three more equations that can be used to predict the amount of background in the signal region with relatively small statistical uncertainty. Those three are $A \times H/E$, $B \times G/E$, and $F \times C/E$.

The three additional background predictions each test the correlation between two of the three selection variables. Here the prediction $A \times H/E$ is used as an example but the argument is the same for the other predictions. Comparing $A \times H/E$ with the chosen background prediction of $A \times F \times G/E^2$ it can be seen that the difference is replacing $F \times G/E$ with H. The E group fails all three thresholds, the F and G groups pass only the β^{-1} and p_T thresholds, respectively, and the H group passes the β^{-1} and p_T thresholds but not dE/dx. If β^{-1} and p_T are uncorrelated then the equation $F \times G/E$ should predict the number of tracks in the H region. So a comparison of the two predictions will test how well the assumption that the variables are uncorrelated works. Likewise, the prediction $B \times G/E$ ($F \times C/E$) tests for possible correlation between p_T and dE/dx (β^{-1} and dE/dx).

The number of predicted tracks coming from the four predictions is shown in Figure 5.32. The spread of the four predictions is used to extract the systematic through Equation 5.5 with N=4. The statistical and systematic uncertainties are shown in Figure 5.33. From the last plot and the agreement in the predicted mass spectrum a conservative systematic uncertainty of 20% is taken.
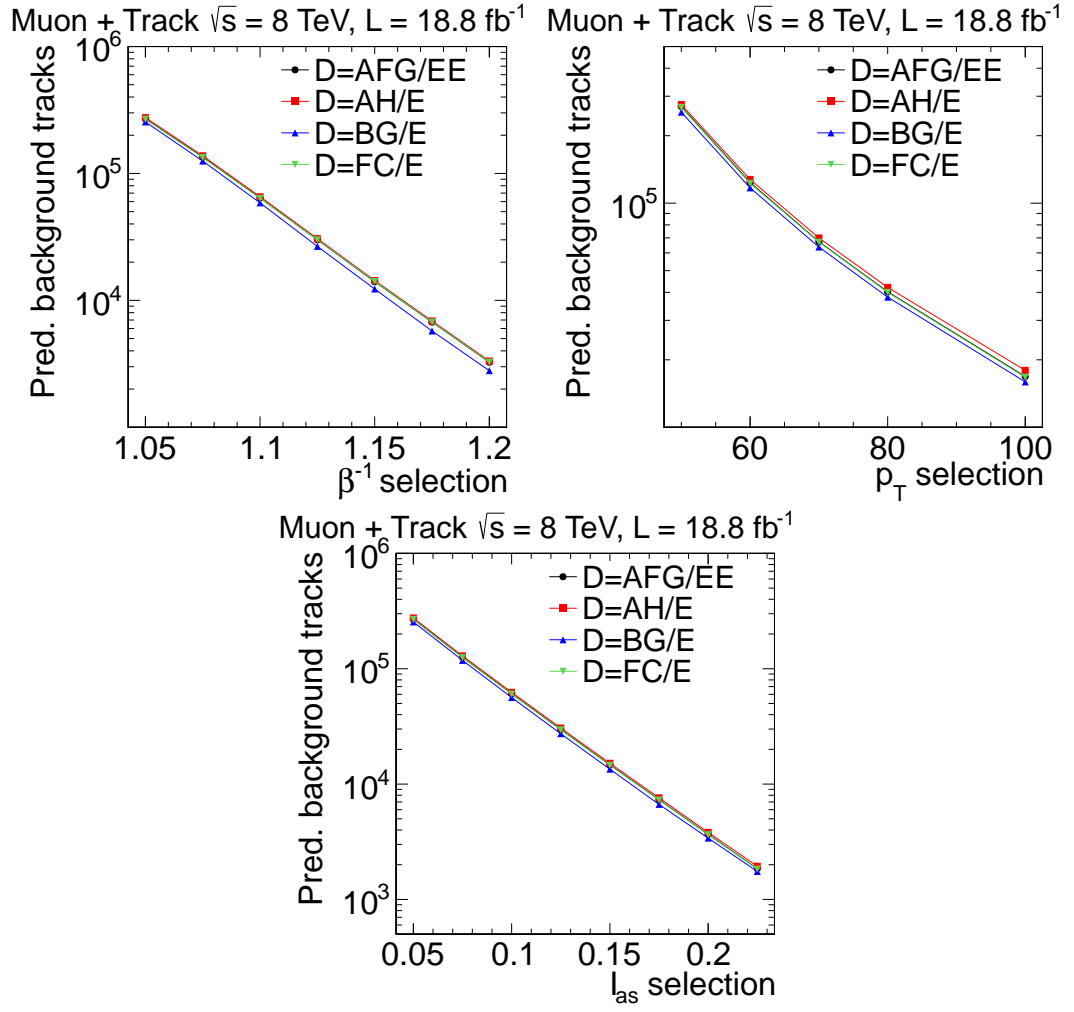
Figure 5.32: Number of predicted tracks from four different background predictions in the *muon+track* analysis. Figures are cumulative as tracks passing the selection with tight thresholds will also pass for loose thresholds. Top Left: p_T and I_{as} threshold of 50 GeV and 0.05, respectively. Threshold on β^{-1} set by x-axis. Top Right: Threshold on β^{-1} and I_{as} of 1.05 and 0.05, respectively. Threshold on p_T set by x-axis. Bottom: Threshold on β^{-1} and p_T of 1.05 and 50 GeV, respectively. Threshold on I_{as} set by x-axis.
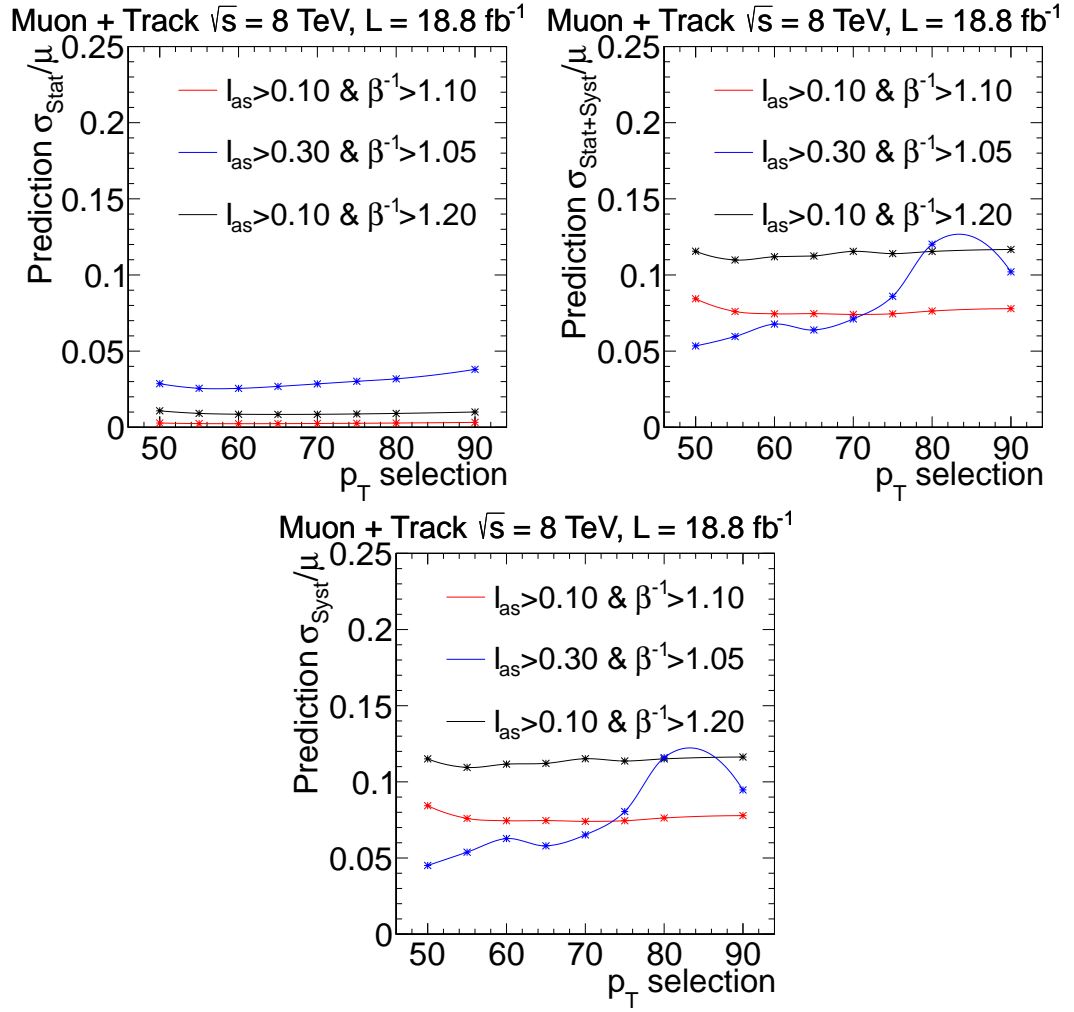
Figure 5.33: Calculation of uncertainty in the *muon+track* analysis. Top left: Ratio of the square root of the quadratic mean of the statistical uncertainties of the three possible background estimations to the mean of these estimations vs the p_T threshold. Top right: Ratio of the standard deviation to the mean of the three background estimations vs p_T. Right: Ratio of the square root of the difference between the variance and the quadratic mean of the statistical uncertainties of the three possible background estimations and the mean vs p_T.

5.7.3 Prediction for *track only* analysis

The prediction for the *track only* analysis is the same as the *muon+track* analysis except only the variables p_T and I_{as} are used in a traditional two dimensional ABCD method. The signal region, D, is predicted as $H \times B/F$ (see Table 5.7). The systematic uncertainty on the background prediction for the *track only* analysis is taken as the same as in the *muon+track* analysis.

5.7.4 Prediction for *multiple charge* analysis

The *multiple charge* analysis employs a two dimensional ABCD method using the variables β^{-1} and I_{as} without a mass requirement. No mass requirement is applied as the mass estimation assumes Q=1e and the large amount of saturation of the tracker readout (see Section 5.6.3) prevents correcting for the charge. No p_T requirement above the one applied at preselection is used in the *multiple charge* analysis because the reconstructed p_T of multiply charged particles is underestimated by a factor of 1/Q. This makes the separation between signal and background in the p_T spectrum small and a higher threshold would remove similar fractions of signal and background.

The signal region, D, is predicted as $H \times C/G$ (see Table 5.7). The background prediction is checked by using the control region with $\beta^{-1} < 1$ as was done for the *muon only* analysis. Figure 5.34 shows the predicted and observed number of tracks for various β^{-1} and I_{as} thresholds in the D' region: good agreement is observed.

The systematic uncertainty for the *multiple charge* analysis is determined by the same method as the *muon only* analysis, replacing p_T for I_{as}. Two additional predictions are made using the tracks in the $\beta^{-1} < 1$ region. Figure 5.35 shows
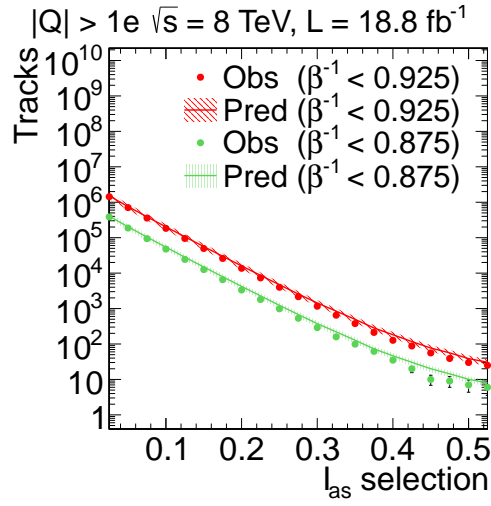
Figure 5.34: Predicted and observed number of tracks in the *multiple charge* analysis in the D' region for different β^{-1} thresholds with the x-axis indicating the I_{as} threshold. Figure is cumulative as tracks passing the selection with tight thresholds will also pass for loose thresholds.
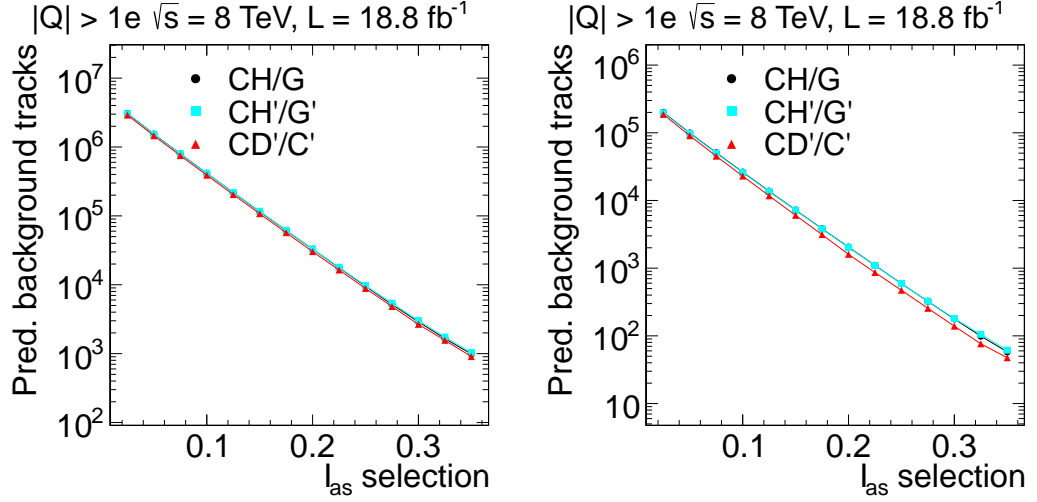
Figure 5.35: Distribution of the number of predicted tracks and their statistical error computed for the *multiple charge* analysis using different regions for two values of the $1/\beta$ threshold. The I_{as} threshold is defined by the x-axis. Figures are cumulative as tracks passing the selection with tight thresholds will also pass for loose thresholds. Left: $1/\beta > 1.05$ (< 0.95 for low $1/\beta$ regions). Right: $1/\beta > 1.15$ (< 0.85 for low $1/\beta$ regions).

the predicted number of tracks for various β^{-1} and dE/dx thresholds for the three predictions.

The spread in the three predictions is then used to determine the systematic uncertainty through Equation 5.5 with N=3. Fig. 5.36 shows the variation of the statistical and systematic uncertainties as a function of the I_{as} threshold. From the last plot a 20% systematic uncertainty is taken on the background estimate for the *multiple charge* analysis.
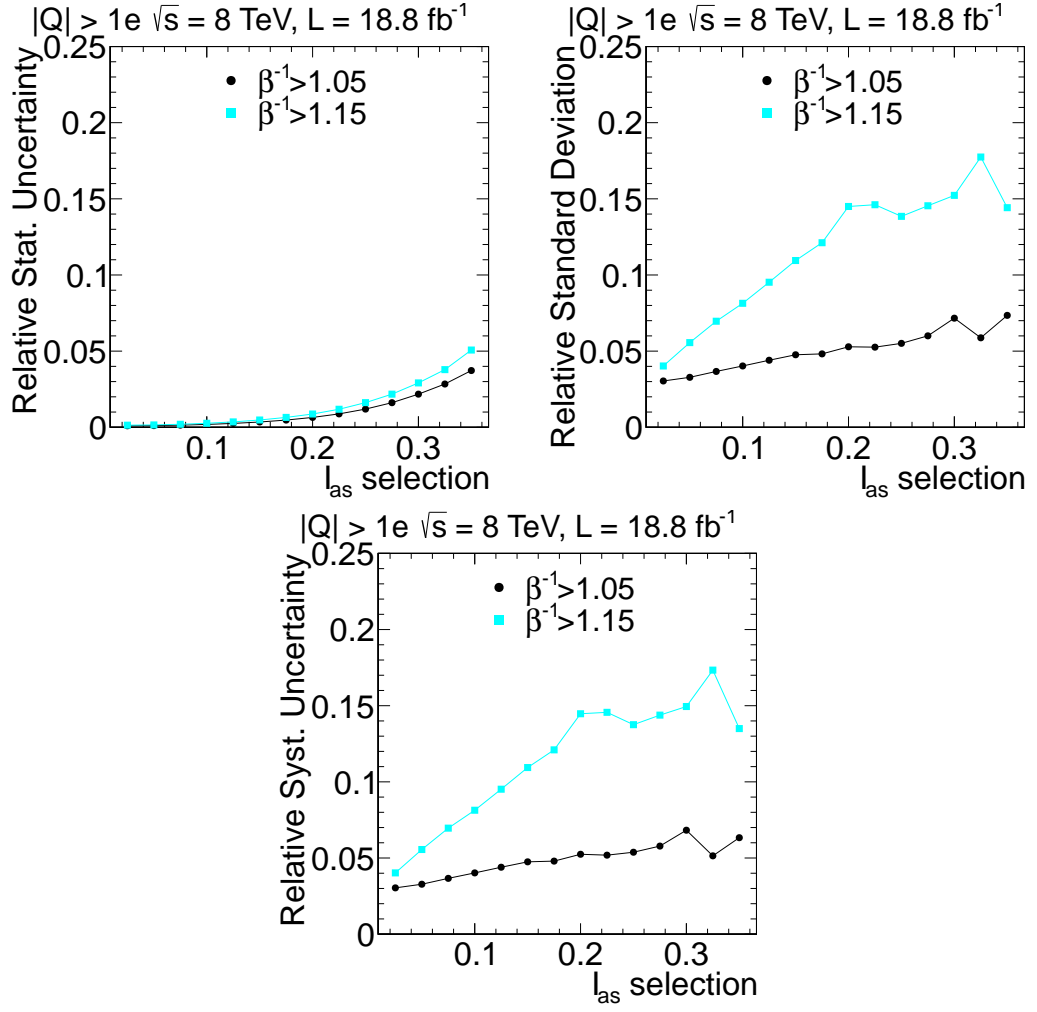
Figure 5.36: Calculation of uncertainty in the *multiple charge* analysis. Top left: Ratio of the square root of the quadratic mean of the statistical uncertainties of the three possible background estimations to the mean of these estimations vs the I_{as} threshold. Top right: Ratio of the standard deviation to the mean of the three background estimations vs I_{as}. Right: Ratio of the square root of the difference between the variance and the quadratic mean of the statistical uncertainties of the three possible background estimations and the mean vs I_{as}.

5.8 Statistical Technique

CMS has a Statistics Committee which provides advice on statistics issues as well tools which can be used to perform statistical calculations. Tools developed in the recent CMS search for the Higgs Boson were used in this analysis to determine the significance of any observed excess and if no excess is observed to place bounds on the signal cross-section. More information about the tools and statistical technique can be found in [3].

One of the tools calculates the significance of a signal by taking in the predicted background with its uncertainty and the observed data. The tool calculates a test statistic, q_0 comparing the likelihood that observed data came from background only or signal plus background. Then the probability of observing a test statistic at least as large as q_0 is found. The smaller the probability the less likely the observed data came from background only. The probability is returned in the form of a one-sided Gaussian sigma. For a given sigma x the probability p is found from Equation 5.12,

$$p = \int_x^\infty \frac{1}{\sqrt{2\pi}} e^{\frac{-x^2}{2}} \, \mathrm{dx}. \tag{5.12}$$

The function being integrated over is a normalized gaussian with unit variance. Particle physics has a somewhat arbitrary convention that one claims a discovery when the significance is greater than five sigma, and evidence when it is greater than three. A five sigma discovery is equivalent to there being a one in 3.5 million probability that observed data come from background only.

This tool can also be used to find the expected reach of the analysis. The expected reach of the analysis is defined as the signal cross-section for which there is a 50% chance of being able to claim a discovery. This is of particular interest when designing the analysis to determine optimum thresholds on the selection

114

variables.

Another tool returns the expected and observed limits on the signal cross-section. The tool is passed the different sources of background with their uncertainties, the signal efficiency with its uncertainty, and finally the integrated luminosity with its uncertainty. The tool then proceeds to calculate the cross section limits with a hybrid CL_s approach [55] using a profile likelihood technique [56] with the predicted background, signal efficiency, and integrated luminosity as nuisance parameters using lognormal pdfs [53, 54]. The uncertainty on the predicted background was discussed in Section 5.7 and the signal efficiency uncertainty is discussed in Section 5.10. The uncertainty on integrated luminosity is 4.4% [57].

5.9   Cut Optimization

All of the analyses calculate the predicted and observed number of tracks for numerous different sets of thresholds on the selection variables. Some of the sets of thresholds have only a small number of tracks in the control regions which are used to make the background prediction. Low statistics in the control region can make the background prediction unreliable and potentially biased if signal tracks make up a large portion of the control region. To prevent this, only thresholds that have at least 25 tracks in all control regions are considered.

The number of predicted and observed events for a few sets of thresholds for the *muon only* and *muon+track* analyses are shown in Figure 5.37. Similar plots are shown for the *track only* and *multiple charge* analyses in Figure 5.38. The observed and predicted mass spectrum with a loose thresholds of $p_T > 55$ GeV, $I_{as} > 0.05$ and $1/\beta > 1.05$ is shown in Figure 5.39 (left) for the *muon+track* analysis. Figure 5.39 (right) shows the same for the *track only* analysis with
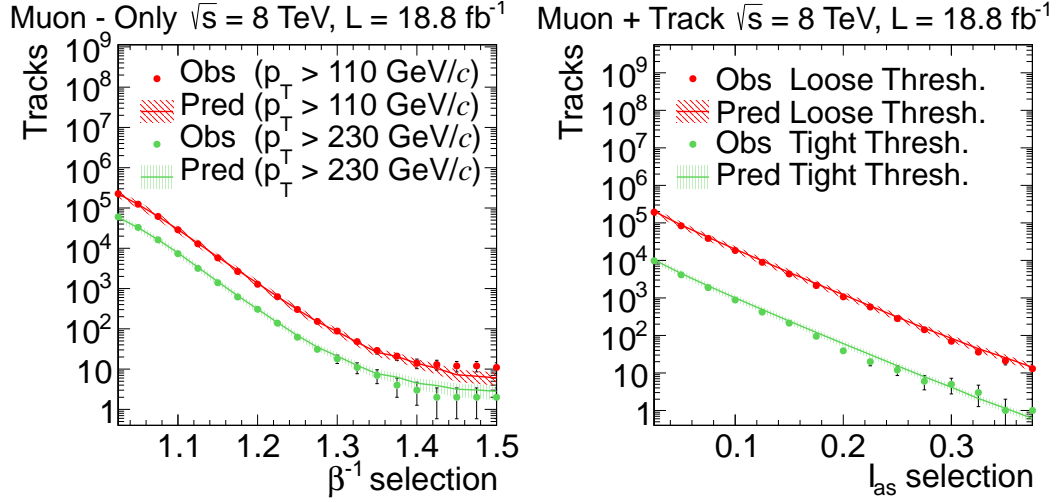
Figure 5.37: Number of predicted and observed events for two different thresholds. Left: For the *muon only* analysis. Threshold for β^{-1} set by X-axis. Right: For the *muon+track* analysis. The loose threshold is defined as $p_T > 55$ GeV/c and $\beta^{-1} > 1.075$. The tight threshold is defined as $p_T > 80$ GeV/c and $\beta^{-1} > 1.125$. Threshold for I_{as} set by X-axis.

thresholds of $p_T > 55$ GeV and $I_{as} > 0.1$.

The thresholds on the selection variables are set trying to optimize two quantities: the expected reach and cross-section limit. The two variables give the power of the analysis for two different hypotheses. Expected reach is concerned with the likelihood of finding a signal if it does exist, while the expected limit is concerned with excluding the signal if it does not exist.

When optimizing the expected reach it is necessary to be careful not to optimize to a region with very small predicted background at the expense of signal efficiency. The reason is that for very small predicted background it is possible to have a five sigma significance with only one or two observed events. For example, one observed event will give a five sigma significance for a predicted background
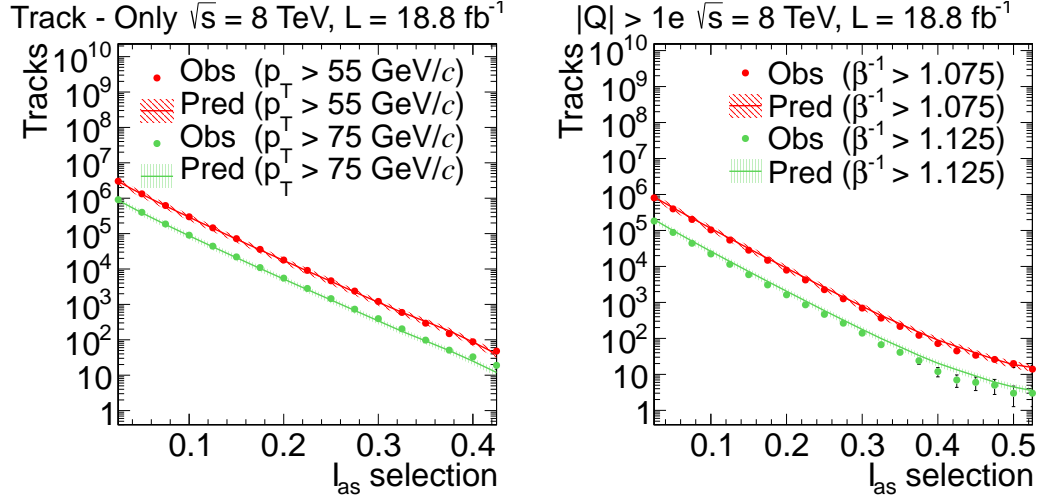
Figure 5.38: Number of predicted and observed events for two different p_T thresholds. Threshold for I_{as} set by X-axis. Left: For the *track only* analysis. Right: For the *multiple charge* analysis.
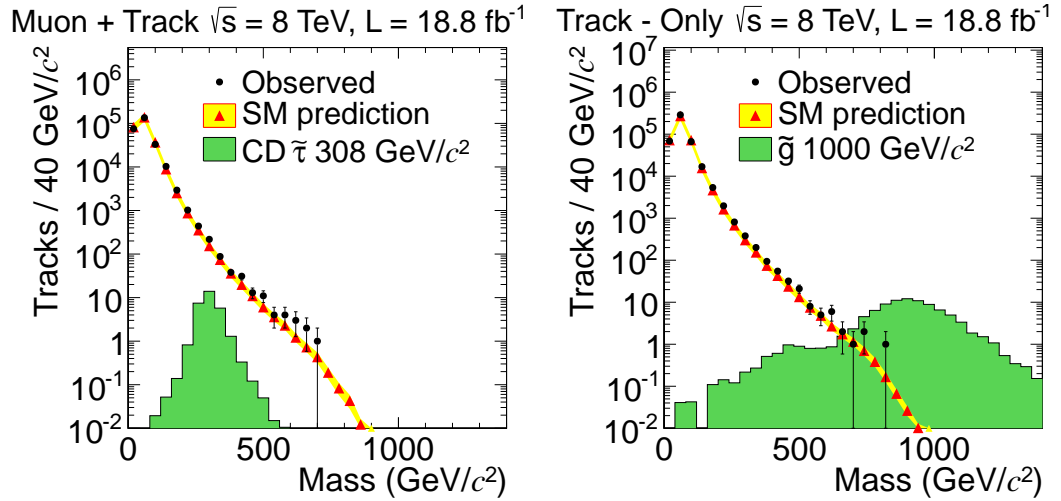
Figure 5.39: Observed and predicted mass spectrum for tracks in the D region with loose thresholds. Left: For the *muon+track* analysis with thresholds of $p_T > 55$ GeV, $I_{as} > 0.05$ and $1/\beta > 1.05$. Right: For the *track only* analysis with thresholds of $p_T > 55$ GeV and $I_{as} > 0.1$ The error bands are only statistical.

of 2.87×10^{-7}. However, a single event is normally not enough to claim discovery of new physics. To protect against this, the definition of the expected reach is modified to be at least as large as the cross-section which is expected to give at least five events, as recommended by the CMS statistics committee.

Most of the time, the two variables agree as to which thresholds are better however in some conditions the variables will disagree. One such case is analyses that have little predicted background and high efficiency for the signal to pass the thresholds on the selection variables. This is the case for high mass samples in the *muon+track* and *track only* analyses. Once the expected cross-section limit falls below the point where more than 50% of the time zero events would be observed in the background only hypothesis, the expected cross-section limit no longer improves by decreasing the expected background. Any loss of efficiency caused by raising the threshold on the selection variables will cause the expected cross-section limit to be optimized at this crossover point. The crossover occurs at approximately 0.6 predicted events with the uncertainties used in the analyses.

The expected reach continues to improve by making the predicted background smaller until a five sigma significance would be found with fewer than five events. At this point the requirement that at least five events be found for a discovery sets the expected reach. This occurs at approximately 0.1 predicted events.

Thus how low the predicted background can be is set differently when optimizing for discovery or limit setting. When the optimization for the best expected reach is used for these cases, the effect on the expected cross-section limit is usually small as the signal efficiency does not decrease much when raising the thresholds. However when the optimization from the expected limit is used, the expected reach can get noticeably worse as more events are needed to claim a discovery. For this reason, combined with the fact that the main goal of these

analyses is to discover new physics, priority is given to the expected reach when trying to optimize the threshold values.

The thresholds are optimized in a two step process. First the set of thresholds which give the best expected reach for each mass/model point is determined. However, this leads to numerous different selections being used which are often very similar and give about the same discriminating power. This is troublesome for two reasons.

The first is that using multiple different selections increases the risk of a statistical fluctuation of the background causing a spurious signal. To account for this a correction must be applied to the obtained local significance such that the value is correctly set to the probability of finding the signal in any of the used sets of thresholds. This means that the global expected reach could be improved by using fewer sets of thresholds even if it comes with the price of making the local expected reach worse.

The second reason is that the analysis becomes much more difficult to understand as there are multiple different sets of thresholds being used as well as multiple predicted and observed events. This complexity brings with it little additional gain in the expected reach or cross section limit and unnecessary complexity is not something that is desired in an analysis. No matter how robust an analysis is, if it can not be understood by others then it can not have an impact on the scientific community at large.

For these reasons a second step is taken attempting to make the thresholds the same for the various mass/model points. If the harm to mass/model points in having the same thresholds is too large, then using more than one set of thresholds is possible. However this was found not to be necessary and a single cut value is used in all analyses.

Table 5.9: Results of the final selections for predicted background and observed number of events. Results for representative mass cuts are given for the *track only* and *muon+track* analyses. Uncertainties are statistical and systematic.

	Selection criteria				Number of events	
	p_T (GeV/c)	I_{as}	β^{-1}	Mass GeV/c^2	Pred.	Obs.
muon only	> 230	-	> 1.40	-	5.6 ± 2.9	3
muon+track	> 70	> 0.125	> 1.225	> 0	43.5 ± 8.7	42
				> 100	5.6 ± 1.1	7
				> 200	0.56 ± 0.11	0
				> 300	0.090 ± 0.02	0
track only	> 70	> 0.4	—	> 0	32.5 ± 6.5	41
				> 100	26.0 ± 5.2	29
				> 200	3.1 ± 0.6	3
				> 300	0.55 ± 0.11	1
				> 400	0.15 ± 0.03	0
$|Q| > 1e$	> 45	> 0.500	> 1.200	—	0.52 ± 0.11	1

The final thresholds used as well as the number of observed and predicted events is shown in Table 5.9. The number of observed events is found to be consistent with the expected background. The largest excess for any of the selections shown in the table is 1.0 sigma in the *track only* analysis with no mass cut. The predicted and observed mass distributions for the *track only* and *muon+track* analyses with the final thresholds are shown in Figure 5.40.
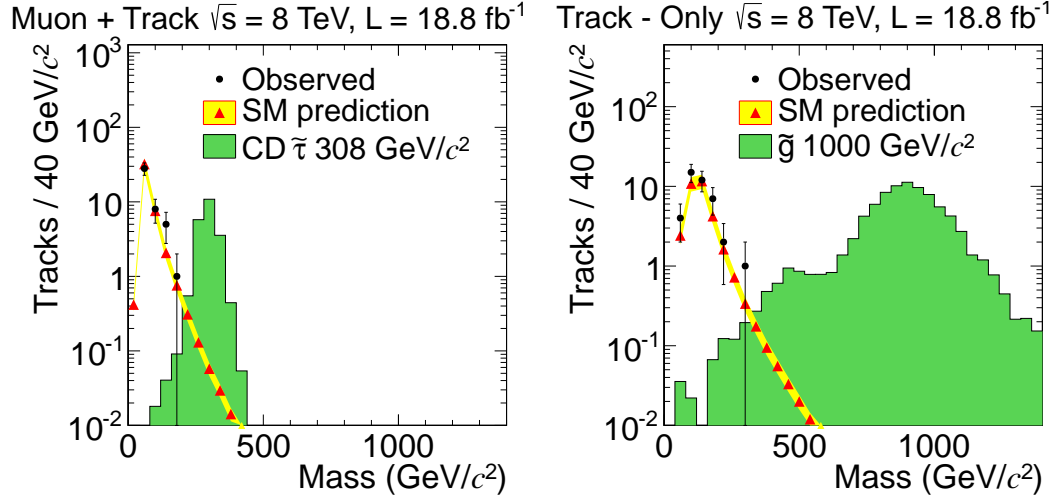
Figure 5.40: Observed and predicted mass spectrum for tracks in the D region in the *muon+track* analysis with the tight selection. The error bands are only statistical. Left: For the *muon+track* analysis. Right: For the *track only* analysis.

5.10 Signal Efficiency Systematic Uncertainties

The signal efficiency for all the analyses is determined from MC. To assess how well MC matches data, numerous studies were performed using control samples.

5.10.1 Trigger Efficiency Uncertainty

The uncertainty on the muon trigger efficiency can come from numerous different effects. A 5% difference in the muon trigger efficiency has been observed between data and MC [19]. An additional uncertainty important to slow moving particles is the timing synchronization in the muon system. As an HSCP arrives in the muon system closer to the switching of the assigned bunch crossing window, a discrepancy in the modeling of the timing synchronization in MC would have a larger effect than for SM particles. The timing of the trigger system is set at the

local system level with the exact segmentation differing between the three muon subsystems.

To determine the size of the effect, the average and RMS of the synchronization of the trigger timing components with respect to the LHC clock for each subsystem was measured. A normalized gaussian distribution was then created for each subsystem with the mean and width equal to the measured values. Then, each trigger timing component was assigned a shift value drawn from the gaussian representing the muon subsystem to which it belongs. The simulation of the detector electronics was then repeated for signal MC samples, with the time of the simulated hits in the detector shifted by the value associated with the portion of the detector the hit is in. Then the reconstruction and trigger simulation steps were redone. Multiple samples were evaluated including the highest mass samples which would have the largest effect. The largest efficiency change was 4% and this is taken as the uncertainty for all samples that use the muon trigger.

Also contributing to the trigger uncertainty is the accuracy of PFMET in the trigger in MC. The uncertainty on the PFMET is dominated by the uncertainty on the measurement of jet energies. A group within CMS studies the agreement between data and MC for jets. For both data and MC, the group releases corrections to the energy scale of jets (JEC) which can be applied after reconstruction to give the best measurement of the energy of the jet. The corrections come with corresponding uncertainties (JEU). The jets used for calculating the PFMET at trigger level are not corrected.

To determine the systematic uncertainty, the jets in the signal MC are adjusted by both the JEC and JEU and the MET is recalculated. The jets are corrected by the MC JEC and then by the inverse of the data JEC. This results in the MC jets having the same properties as uncorrected jets in data. The JEU

are applied by decreasing the energy of each jet by its uncertainty. The JEC are found to increase the efficiency slightly while the JEU decrease it by approximately 1%. Conservatively, no scale factor is applied on the trigger efficiency and a 1% uncertainty is taken on the MET trigger for all samples.

The total systematic uncertainty on trigger efficiency is found by combining the above effects. The muon trigger is dominant for all samples except for the charge suppressed samples where the muon trigger does not have any efficiency. For those samples, the trigger efficiency uncertainty comes only from the MET uncertainty.

5.10.2 Uncertainty on Selection Variables

The uncertainty on the β^{-1} measurement is studied using muons from the decay of Z bosons. Muons are required to pass a tight selection provided by the muon POG to give a pure muon sample. Additionally the event must have a pair of oppositely charged muons with an invariant mass of $M_Z \pm 10$ GeV. Only the two muons forming the combination are used. If more than one such pair exists, the pair with invariant mass closest to M_Z is used. An uncertainty of 0.005 is taken on the β^{-1} measurement from the disagreement between data and MC. This uncertainty is evaluated separately for all samples and is found to be less than 7% for all considered signals.

The uncertainty due to the p_T measurement is determined by varying the $1/p_T$ value by a prescription from the muon POG [19]. For the *muon only* analysis the $1/p_T$ of the muon system track is shifted up by 10%, this means that the p_T will decrease. For the other analyses the $1/p_T$ of the inner track is adjusted by the Equation

$$\frac{1}{p_T\prime} = \frac{1}{p_T} + \delta_{K_T}(q, \phi, \eta) \tag{5.13}$$

$$\delta_{K_T}(q, \phi, \eta) = A + B\eta^2 + qC\sin(\phi - \phi_0) \tag{5.14}$$

where A = 0.236 TeV^{-1}, B = -0.135 TeV^{-1}, C = 0.282 TeV^{-1}, and $\phi_0 = 1.337$. The shifts were found to have a less than 10% effect on the efficiency to pass the final selection for all signals.

The effect of the uncertainty on dE/dx was evaluated with low momentum protons. Protons with p less than about 2 GeV will have speed appreciably lower than the speed of light and thus will appear similar to signal particles. A comparison of data and MC yields an uncertainty of 0.05 on I_{as} and 5% on I_h. When propagated to the final selection for singly charged particles, these uncertainties give efficiency changes of less than 13% for low mass samples and less than 7% for masses above 200 GeV/c^2. Multiply charged particles have sufficient separation between signal and background that the uncertainty is negligible.

5.10.3 Other Uncertainties on Signal Efficiency

The systematic uncertainty on muon [19] and track [58] reconstruction were both found to be less than 2%. A 1% uncertainty recommended by the muon POG is applied on the correction factors used in the *muon only* analysis described in Section 5.6.5.

The uncertainty on the number of proton-proton collisions per bunch crossing is found by varying by 6% the proton-proton cross-section used to determine the weights for MC events (see end of Sec. 5.3). This leads to an uncertainty of less than 4% for all samples.

Multiply charged particles deposit a large amount of energy in the calorimeter and if the particle does not have enough energy it may come to a stop in the calorimeter. This is particularly important for high charge, low mass samples, because if the particle has enough energy to pass through the calorimeter then it will be traveling at a high speed and be unlikely to pass the threshold on β^{-1}. Uncertainty on the amount of detector material, determined mostly by the HCAL, affects the number of HSCP that will stop. There is a conservative 5% uncertainty on the material budget as measured by energy loss of cosmic ray muons passing through CMS [59]. Shifting the material density by this amount for a few signal samples has at most a 20% effect. This 20% uncertainty is conservatively taken for all multiply charged samples.

5.10.4   Total Signal Efficiency Uncertainty

The total systematic uncertainty for each signal point is found by adding the above effects in quadrature. Figure 5.41 shows the different sources of signal efficiency systematic uncertainty and their quadratic sum for the various signal models considered in the *muon only* analysis. Figure 5.42 and 5.43 shows the same for the *muon+track* analysis for stau and $R - hadron$ models, respectively. Figure 5.44 shows the sources of systematic uncertainty for a few of the samples in the *track only* and *multiple charge* analyses.

The total signal efficiency uncertainty for all considered models is shown in Figure 5.45 for the four analyses. The signal efficiency uncertainty used for each signal point is what is shown in this figure. For all analyses except for the *multiple charge* analysis, the uncertainty is less than 15% for all signal points and less than 10% for a large majority of signal points. The large uncertainty on the amount of detector material results in the uncertainty for the multiply charged particles

125

to be between 20% and 30%.

5.11 Final Results

As discussed in Section 5.9, the observed data were found to be consistent with the expected background. Therefore, limits are placed on the production rate of various models of new physics. The statistical method used to determine the limits is discussed in Section 5.8. Figure 5.46 shows the cross-section limit at 95% confidence level (CL) for all considered models in the *muon only* and *muon+track* analyses. Figure 5.47 shows the same for the *track only* and *multiple charge* analyses.

The CMS results for all the analyses except for *muon only* combine the 8 TeV data collected in 2012 with 7 TeV data collected in 2011. The combined result places limits on the relative signal strength, σ/σ_{th}. The 7 TeV results are simply added here without further description. The limits on the relative cross-section for the *muon only* and *muon+track* analyses is shown in Figure 5.48. For the *muon only* analysis the limit on signal strength uses only 8 TeV data. The limits on the relative cross-section for the *track only* and *multiple charge* analyses is shown in Figure 5.49.

Table 5.10 has the observed and expected limits for all the signal points in the *muon only* analysis as well as the signal efficiency. Table 5.11 shows the same for the *muon+track* analysis. Tables 5.12 and 5.13 show the efficiency and observed and expected limits for some of the signal points in the *track only* and *multiple charge* analyses, respectively.

126

Table 5.10: Summary table of results for all the considered signal points for the *muon only* analysis. The signal efficiency and observed and expected limits on the cross section (in *pb*) at $\sqrt{s} = 8$ TeV are presented. Also the observed and expected limits on the signal strength at $\sqrt{s} = 8$ TeV.

Mass	$\sigma(pb)$			$\mu = \sigma/\sigma_{TH}$	
(GeV/c^2)	$\sqrt{s} = 8TeV$			$\sqrt{s} = 8$ TeV	
	Eff.	Obs.	Exp.	Obs.	Exp.
Gluino 100% $\tilde{g}g$ - *muon only* analysis					
300	0.05	0.0075	0.007	7.3×10^{-5}	6.8×10^{-5}
400	0.07	0.0057	0.005	3.1×10^{-4}	2.7×10^{-4}
500	0.09	0.0044	0.0037	0.00098	8.4×10^{-4}
600	0.10	0.0028	0.0034	0.0022	0.0026
700	0.10	0.0027	0.0032	0.0063	0.0075
800	0.11	0.0025	0.003	0.017	0.02
900	0.11	0.0024	0.0029	0.041	0.049
1000	0.11	0.0022	0.003	0.094	0.12
1100	0.11	0.0025	0.003	0.25	0.3
1200	0.10	0.0026	0.0032	0.6	0.73
1300	0.10	0.0027	0.0032	1.4	1.7
1400	0.09	0.003	0.0036	3.4	4.1
1500	0.09	0.0031	0.0037	7.9	9.5
Gluino 50% $\tilde{g}g$ - *muon only* analysis					

Table 5.10 – *Continued from previous page*

Mass (GeV/c^2)	σ (pb) $\sqrt{s} = 8 TeV$			$\mu = \sigma/\sigma_{TH}$ $\sqrt{s} = 8$ TeV	
	Eff.	Obs.	Exp.	Obs.	Exp.
300	0.06	0.0065	0.006	6.3×10^{-5}	5.8×10^{-5}
400	0.08	0.0048	0.0041	2.6×10^{-4}	2.2×10^{-4}
500	0.10	0.0037	0.0032	8.3×10^{-4}	7.2×10^{-4}
600	0.11	0.0024	0.0028	0.0019	0.0022
700	0.12	0.0022	0.0026	0.0051	0.0062
800	0.13	0.0021	0.0025	0.014	0.017
900	0.14	0.002	0.0024	0.034	0.041
1000	0.13	0.002	0.0024	0.085	0.1
1100	0.13	0.002	0.0024	0.2	0.24
1200	0.13	0.0021	0.0025	0.48	0.58
1300	0.12	0.0022	0.0026	1.1	1.4
1400	0.12	0.0023	0.0028	2.6	3.2
1500	0.11	0.0024	0.003	6.2	7.5
Gluino 10% $\tilde{g}g$ - *muon only* analysis					
300	0.06	0.0058	0.0054	5.7×10^{-5}	5.3×10^{-5}
400	0.09	0.0042	0.0037	2.3×10^{-4}	2.0×10^{-4}
500	0.11	0.0034	0.0029	7.6×10^{-4}	6.6×10^{-4}
600	0.13	0.0022	0.0026	0.0017	0.002
700	0.14	0.0019	0.0023	0.0044	0.0055
800	0.15	0.0019	0.0022	0.012	0.015
900	0.15	0.0017	0.0021	0.029	0.036
1000	0.15	0.0018	0.0021	0.074	0.089

Continued on next page

Mass (GeV/c^2)	σ (pb) $\sqrt{s} = 8TeV$			$\mu = \sigma/\sigma_{TH}$ $\sqrt{s} = 8$ TeV	
	Eff.	Obs.	Exp.	Obs.	Exp.
1100	0.15	0.0018	0.0021	0.18	0.21
1200	0.15	0.0018	0.0022	0.41	0.51
1300	0.14	0.0019	0.0023	0.97	1.2
1400	0.14	0.002	0.0024	2.3	2.8
1500	0.13	0.0021	0.0026	5.3	6.5
Stop - *muon only* analysis					
100	0.01	0.073	0.063	1.4×10^{-4}	1.2×10^{-4}
200	0.02	0.016	0.014	8.9×10^{-4}	7.8×10^{-4}
300	0.05	0.0052	0.0066	0.0027	0.0034
400	0.08	0.0035	0.0042	0.01	0.012
500	0.10	0.0027	0.0033	0.032	0.039
600	0.12	0.0022	0.0027	0.09	0.11
700	0.14	0.002	0.0024	0.25	0.3
800	0.15	0.0017	0.0021	0.6	0.75
900	0.17	0.0016	0.002	1.5	1.8
1000	0.18	0.0015	0.0019	3.5	4.4

Table 5.11: Summary table of results for all the considered signal points for the *muon+track* analysis. The signal efficiency and observed and expected limits on the cross section (in *pb*) at $\sqrt{s} = 8$ TeV. Also the observed and expected limits on the signal strength at $\sqrt{s} = 7 + 8$ TeV.

Mass (GeV/c^2)	Mass Req. (GeV/c^2)	σ (pb) $\sqrt{s} = 8TeV$			$\mu = \sigma/\sigma_{TH}$ $\sqrt{s} = 7 + 8$ TeV	
		Eff.	Obs.	Exp.	Obs.	Exp.
CD Stau - *muon+track* analysis						
100	> 20	0.16	0.0062	0.0063	0.0023	0.0025
126	> 40	0.25	0.0042	0.0042	0.0065	0.0074
156	> 70	0.32	0.0024	0.0017	0.017	0.013
200	> 110	0.41	0.0012	7.7×10^{-4}	0.056	0.031
247	> 150	0.50	8.1×10^{-4}	4.4×10^{-4}	0.15	0.068
308	> 190	0.56	2.8×10^{-4}	2.9×10^{-4}	0.21	0.16
370	> 240	0.60	2.7×10^{-4}	2.6×10^{-4}	0.4	0.38
432	> 290	0.64	2.5×10^{-4}	2.3×10^{-4}	0.92	0.86
494	> 330	0.66	2.5×10^{-4}	2.3×10^{-4}	1.9	1.9
DP - *muon+track* analysis						
100	> 20	0.17	0.0056	0.0062	0.099	0.11
126	> 40	0.24	0.0043	0.0044	0.16	0.18
156	> 60	0.28	0.0027	0.0024	0.23	0.21
200	> 100	0.34	0.0013	0.001	0.42	0.26

Table 5.11 – *Continued from previous page*

Mass	Mass	σ (pb)			$\mu = \sigma/\sigma_{TH}$	
(GeV/c^2)	Req.	$\sqrt{s} = 8 TeV$			$\sqrt{s} = 7 + 8$ TeV	
	(GeV/c^2)	Eff.	Obs.	Exp.	Obs.	Exp.
247	> 140	0.40	0.00099	5.8×10^{-4}	0.85	0.37
308	> 190	0.46	3.5×10^{-4}	3.5×10^{-4}	0.66	0.62
370	> 240	0.53	3.0×10^{-4}	2.9×10^{-4}	1.4	1.2
432	> 280	0.57	2.9×10^{-4}	2.6×10^{-4}	2.5	2.4
494	> 330	0.61	2.6×10^{-4}	2.5×10^{-4}	5	4.7
Gluino 50% $\tilde{g}g$ - *muon+track* analysis						
300	> 110	0.07	0.0044	0.0041	5.0×10^{-5}	3.1×10^{-5}
400	> 190	0.08	0.0021	0.002	9.6×10^{-5}	9.3×10^{-5}
500	> 260	0.09	0.0021	0.0016	2.8×10^{-4}	3.1×10^{-4}
600	> 330	0.09	0.0018	0.0016	0.0012	0.0011
700	> 400	0.09	0.0018	0.0018	0.0037	0.0034
800	> 480	0.08	0.0019	0.0019	0.011	0.01
900	> 530	0.08	0.0021	0.002	0.031	0.029
1000	> 610	0.07	0.0023	0.0023	0.085	0.082
1100	> 660	0.06	0.0028	0.0026	0.24	0.23
1200	> 710	0.05	0.0034	0.0032	0.69	0.66
1300	> 750	0.04	0.0041	0.0039	1.9	1.8
1400	> 800	0.03	0.0054	0.0051	5.7	5.3
1500	> 830	0.02	0.0069	0.0066	17	16
Gluino 10% $\tilde{g}g$ - *muon+track* analysis						
300	> 110	0.14	0.0024	0.0022	2.6×10^{-5}	1.7×10^{-5}

Table 5.11 – *Continued from previous page*

Mass (GeV/c^2)	Mass Req. (GeV/c^2)	σ (pb) $\sqrt{s} = 8 TeV$			$\mu = \sigma/\sigma_{TH}$ $\sqrt{s} = 7 + 8$ TeV	
		Eff.	Obs.	Exp.	Obs.	Exp.
400	> 190	0.15	0.0011	0.0011	5.6×10^{-5}	5.1×10^{-5}
500	> 260	0.16	0.0011	8.7×10^{-4}	1.6×10^{-4}	1.8×10^{-4}
600	> 330	0.17	8.7×10^{-4}	9.1×10^{-4}	6.0×10^{-4}	6.0×10^{-4}
700	> 410	0.16	0.00096	0.001	0.0021	0.0017
800	> 480	0.15	0.0011	0.001	0.0058	0.0057
900	> 540	0.14	0.0012	0.0011	0.017	0.016
1000	> 610	0.12	0.0013	0.0012	0.046	0.045
1100	> 660	0.11	0.0015	0.0014	0.13	0.12
1200	> 710	0.09	0.0018	0.0017	0.37	0.35
1300	> 750	0.07	0.0022	0.0021	1	0.99
1400	> 800	0.06	0.0029	0.0027	2.9	2.8
1500	> 830	0.04	0.0037	0.0035	8.6	8.1
Stop - *muon+track* analysis						
100	> 0	0.06	0.019	0.019	3.0×10^{-5}	2.8×10^{-5}
200	> 0	0.12	0.0088	0.0085	4.0×10^{-4}	2.6×10^{-4}
300	> 20	0.15	0.0068	0.0069	0.0024	0.0019
400	> 80	0.16	0.0039	0.0028	0.0072	0.0055
500	> 140	0.17	0.0022	0.0013	0.019	0.013
600	> 210	0.18	8.8×10^{-4}	9.1×10^{-4}	0.031	0.031
700	> 290	0.17	9.4×10^{-4}	8.8×10^{-4}	0.099	0.094
800	> 370	0.17	0.00097	9.1×10^{-4}	0.29	0.27
900	> 450	0.15	0.0011	0.001	0.84	0.79

Table 5.11 – *Continued from previous page*

Mass (GeV/c^2)	Mass Req. (GeV/c^2)	σ (pb) $\sqrt{s} = 8 TeV$			$\mu = \sigma/\sigma_{TH}$ $\sqrt{s} = 7 + 8$ TeV	
		Eff.	Obs.	Exp.	Obs.	Exp.
1000	> 530	0.13	0.0012	0.0012	2.5	2.3
DY Q = 1e - *muon+track* analysis						
100	> 40	0.15	0.0068	0.0069	0.011	0.012
200	> 120	0.36	0.0013	7.7×10^{-4}	0.04	0.019
300	> 190	0.48	3.3×10^{-4}	3.4×10^{-4}	0.06	0.046
400	> 270	0.53	3.0×10^{-4}	2.9×10^{-4}	0.15	0.14
500	> 340	0.56	2.9×10^{-4}	2.8×10^{-4}	0.44	0.41
600	> 400	0.56	2.9×10^{-4}	2.8×10^{-4}	1.2	1.1
700	> 470	0.55	3.0×10^{-4}	2.8×10^{-4}	3.1	3
800	> 530	0.52	3.1×10^{-4}	3.0×10^{-4}	8.1	7.5
900	> 590	0.49	3.3×10^{-4}	3.2×10^{-4}	20	19
1000	> 650	0.45	3.6×10^{-4}	3.4×10^{-4}	49	48

Table 5.12: Summary table of results for some of the considered signal points for the *track only* analysis. The signal efficiency and observed and expected limits on the cross section (in *pb*) at $\sqrt{s} = 8$ TeV. Also the observed and expected limits on the signal strength at $\sqrt{s} = 7 + 8$ TeV.

Mass (GeV/c^2)	Mass Req. (GeV/c^2)	σ (pb) $\sqrt{s} = 8TeV$			$\mu = \sigma/\sigma_{TH}$ $\sqrt{s} = 7 + 8$ TeV	
		Eff.	Obs.	Exp.	Obs.	Exp.
Gluino 50% $\tilde{g}g$ - *track only* analysis						
300	> 100	0.08	0.01	0.01	8.4×10^{-5}	7.3×10^{-5}
500	> 230	0.10	0.002	0.0022	4.6×10^{-4}	4.0×10^{-4}
700	> 360	0.11	0.0015	0.0015	0.003	0.0031
900	> 460	0.09	0.0017	0.0016	0.025	0.025
1100	> 530	0.08	0.0021	0.0019	0.18	0.18
1300	> 540	0.06	0.0028	0.0026	1.4	1.3
1500	> 520	0.04	0.004	0.0039	9.8	9.3
Gluino 10% $\tilde{g}g$ - *track only* analysis						
300	> 100	0.15	0.0055	0.0055	4.6×10^{-5}	4.0×10^{-5}
500	> 240	0.19	0.001	0.0011	2.1×10^{-4}	2.1×10^{-4}
700	> 370	0.19	8.4×10^{-4}	8.1×10^{-4}	0.0018	0.0017
900	> 470	0.17	9.5×10^{-4}	8.9×10^{-4}	0.014	0.014
1100	> 540	0.14	0.0011	0.001	0.1	0.098
1300	> 550	0.11	0.0015	0.0014	0.74	0.68
1500	> 530	0.07	0.0022	0.0021	5.2	5.1

Table 5.12 – *Continued from previous page*

Mass (GeV/c^2)	Mass Req. (GeV/c^2)	σ (pb) $\sqrt{s} = 8TeV$			$\mu = \sigma/\sigma_{TH}$ $\sqrt{s} = 7 + 8$ TeV	
		Eff.	Obs.	Exp.	Obs.	Exp.
Gluino Charge Suppressed 10% $\tilde{g}g$ - *track only* analysis						
300	> 130	0.05	0.013	0.013	1.2×10^{-4}	1.1×10^{-4}
500	> 240	0.07	0.0027	0.0028	5.8×10^{-4}	6.4×10^{-4}
700	> 340	0.08	0.0021	0.002	0.0043	0.0044
900	> 400	0.07	0.0022	0.0021	0.035	0.034
1100	> 410	0.06	0.0026	0.0025	0.25	0.24
1300	> 400	0.05	0.0034	0.0033	1.6	1.7
1500	> 340	0.04	0.0045	0.0045	11	11
Stop - *track only* analysis						
200	> 0	0.18	0.005	0.0051	2.9×10^{-4}	2.6×10^{-4}
400	> 60	0.23	0.0058	0.0041	0.0098	0.0076
600	> 190	0.24	0.0024	0.0013	0.075	0.043
800	> 330	0.22	7.3×10^{-4}	7.2×10^{-4}	0.22	0.21
200	> 0	0.05	0.026	0.02	0.0015	0.0011
Stop Charge Suppressed - *track only* analysis						
200	> 0	0.05	0.026	0.02	0.0015	0.0011
400	> 50	0.09	0.015	0.01	0.03	0.023
600	> 170	0.10	0.0055	0.0036	0.18	0.12
800	> 270	0.10	0.0023	0.0019	0.73	0.62
1000	> 360	0.08	0.0019	0.0019	4	3.8

Table 5.13: Summary table of results for some of the considered signal points for the *multiple charge* analysis. The signal efficiency and observed and expected limits on the cross section (in *pb*) at $\sqrt{s} = 8$ TeV. Also the observed and expected limits on the signal strength at $\sqrt{s} = 7 + 8$ TeV.

Mass (GeV/c^2)	σ (pb) $\sqrt{s} = 8TeV$			$\mu = \sigma/\sigma_{TH}$ $\sqrt{s} = 7 + 8$ TeV	
	Eff.	Obs.	Exp.	Obs.	Exp.
DY Q = 1e - *multiple charge* analysis					
300	0.34	7.1×10^{-4}	4.8×10^{-4}	0.085	0.06
600	0.47	5.1×10^{-4}	3.5×10^{-4}	2	1.5
900	0.44	5.5×10^{-4}	3.7×10^{-4}	31	22
DY Q = 2e - *multiple charge* analysis					
300	0.47	5.0×10^{-4}	3.5×10^{-4}	0.015	0.011
600	0.58	4.1×10^{-4}	2.8×10^{-4}	0.42	0.29
900	0.53	4.4×10^{-4}	3.0×10^{-4}	6.6	4.7
DY Q = 3e - *multiple charge* analysis					
300	0.32	7.4×10^{-4}	5.2×10^{-4}	0.0096	0.0071
600	0.48	4.9×10^{-4}	3.4×10^{-4}	0.23	0.16
900	0.47	4.9×10^{-4}	3.4×10^{-4}	3.4	2.4
DY Q = 4e - *multiple charge* analysis					
300	0.18	0.0013	9.0×10^{-4}	0.0099	0.0072
600	0.35	6.7×10^{-4}	4.7×10^{-4}	0.17	0.12

Table 5.13 – *Continued from previous page*

Mass (GeV/c^2)	σ (pb) $\sqrt{s} = 8 TeV$			$\mu = \sigma/\sigma_{TH}$ $\sqrt{s} = 7 + 8$ TeV	
	Eff.	Obs.	Exp.	Obs.	Exp.
900	0.36	6.5×10^{-4}	4.5×10^{-4}	2.5	1.7
DY Q = 5e - *multiple charge* analysis					
300	0.08	0.0029	0.002	0.015	0.01
600	0.22	0.0011	7.4×10^{-4}	0.18	0.13
900	0.24	0.00099	6.7×10^{-4}	2.4	1.7
DY Q = 6e - *multiple charge* analysis					
300	0.03	0.007	0.0047	0.026	0.018
600	0.13	0.0018	0.0012	0.21	0.15
900	0.15	0.0016	0.0011	2.6	1.9
DY Q = 7e - *multiple charge* analysis					
300	0.01	0.018	0.012	0.049	0.035
600	0.08	0.003	0.0021	0.26	0.19
900	0.10	0.0024	0.0017	3.2	2.2
DY Q = 8E- - *multiple charge* analysis					
300	0.01	0.047	0.032	0.1	0.073
600	0.05	0.0052	0.0035	0.36	0.26
900	0.06	0.0039	0.0027	3.8	2.7

Mass limits are placed on the various models by all analyses. The mass limit is found by where the limit on the relative signal strength crosses one. The *muon only* analysis gives mass limits of 1258, 1283, and 1300 GeV/c^2 for gluino

production with the fraction, f, of $\tilde{g}g$ set to $f = 100\%$, $f = 50\%$, and $f = 10\%$, respectively. The mass limit on stop production is placed at 853 GeV/c^2. The *muon+track* analysis sets a mass limit on gluino production with $f = 50\%$ ($f = 10\%$) of 1224 (1291) GeV/c^2. The limit on stop production is placed at 910 GeV/c^2. A limit of 435 and 339 GeV/c^2 is placed on the CS and DP stau scenarios, respectively. Drell-Yan production of Q=1e particles has a limit set at 574 GeV/c^2.

The *track only* analysis excludes $f = 10\%$ gluino production for masses below 1320 (1239) GeV/c^2 in the cloud interaction (charge suppression) model. The mass limit on stop production is placed at 934 (820) GeV/c^2 for the cloud interaction (charge suppression) model. The *multiple charge* analysis sets limits on Q= 1e, 2e, 3e, 4e, 5e, 6e, 7e, and 8e production at 517, 685, 752, 793, 796, 781, 757, and 737 GeV/c^2, respectively.

The mass limits for the various signals and electric charges can be seen in Fig. 5.50 as well as limits from previously published searches by CMS and others. The mass limit obtained with the *multiple charge* analysis for Drell–Yan like production of particles with non-unit charge in the range $1e < |Q| \leq 8e$ can be parametrized as $M^{95\%}(Q) = 404.9 + 154.6|Q/e| - 14.8|Q/e|^2$ GeV/c^2

As can be seen the limits presented here are the most stringent in the world to date. These limits put important constraints on many versions of supersymmetry and the production of multiply charged particles as discussed in Section 2.3. The results also apply to a wide range of other theories not directly considered here that can include the production of long-lived charged particles.

5.12 Conclusion

Four analyses were performed searching for heavy long-lived charged particles in proton-proton collision data collected by CMS. One search only requires the particle be found in the outer muon system allowing it to be sensitive to particles produced neutral and only becoming charged by interacting with the detector. The second analysis looks for particles reconstructed in both the inner tracker and the muon system. This analysis is especially powerful for lepton-like long-lived particles which will always be charged during the entirety of their passage through the CMS detector. The third search only requires particles be found in the inner tracker of CMS making it sensitive to particles becoming neutral before reaching the muon system. The last search is optimized to look for particles with electric charge greater than that of an electron.

The signatures of new long-lived charged particles, long time of flight, high momentum, and large ionization energy loss, are used to separate the signal from the large background of SM particles. A data-driven procedure is used to estimate the SM background in the final selection region. The efficiency for signal particles to be accepted in the selection region is evaluated by numerous studies in control regions. Data are found to agree with the predicted background and limits are placed on the production rates of various models of new physics that predict the existence of long-lived particles. All of the limits are the best produced to date and put important constraints on physics beyond the Standard Model.
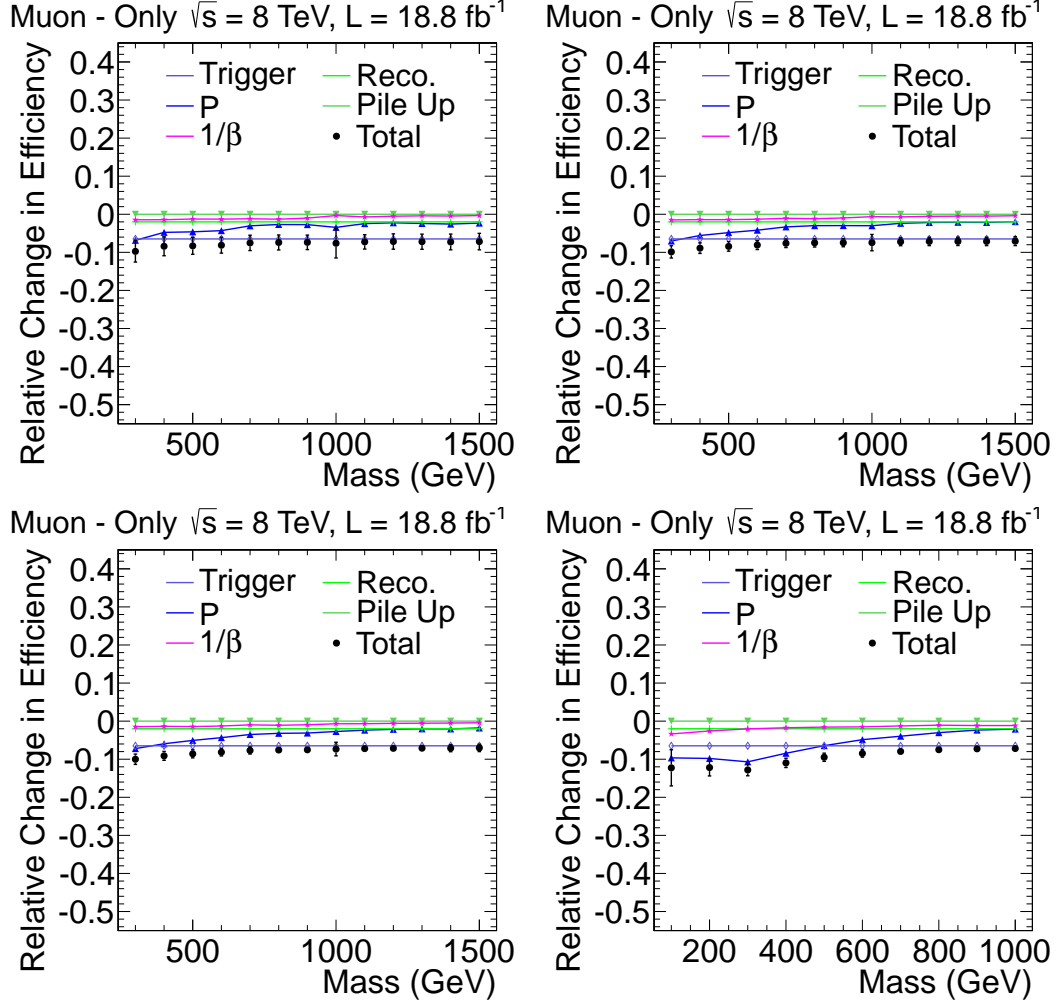
Figure 5.41: Relative signal efficiency change seen for the various sources of uncertainty in the *muon only* analysis. Top row: Gluino with $f = 1.0$ (left) and $f = 0.5$ (right). Bottom row: Gluino with $f = 0.1$ (left) and stop (right)
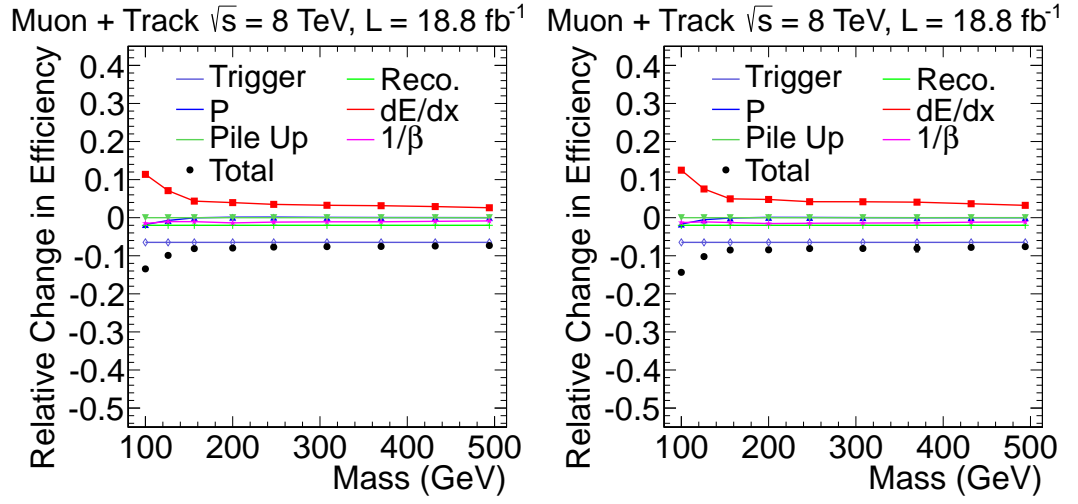
Figure 5.42: Relative signal efficiency change seen for the various sources of uncertainty for stau models in the *muon+track* analysis. CD (left) and DP (right) models.
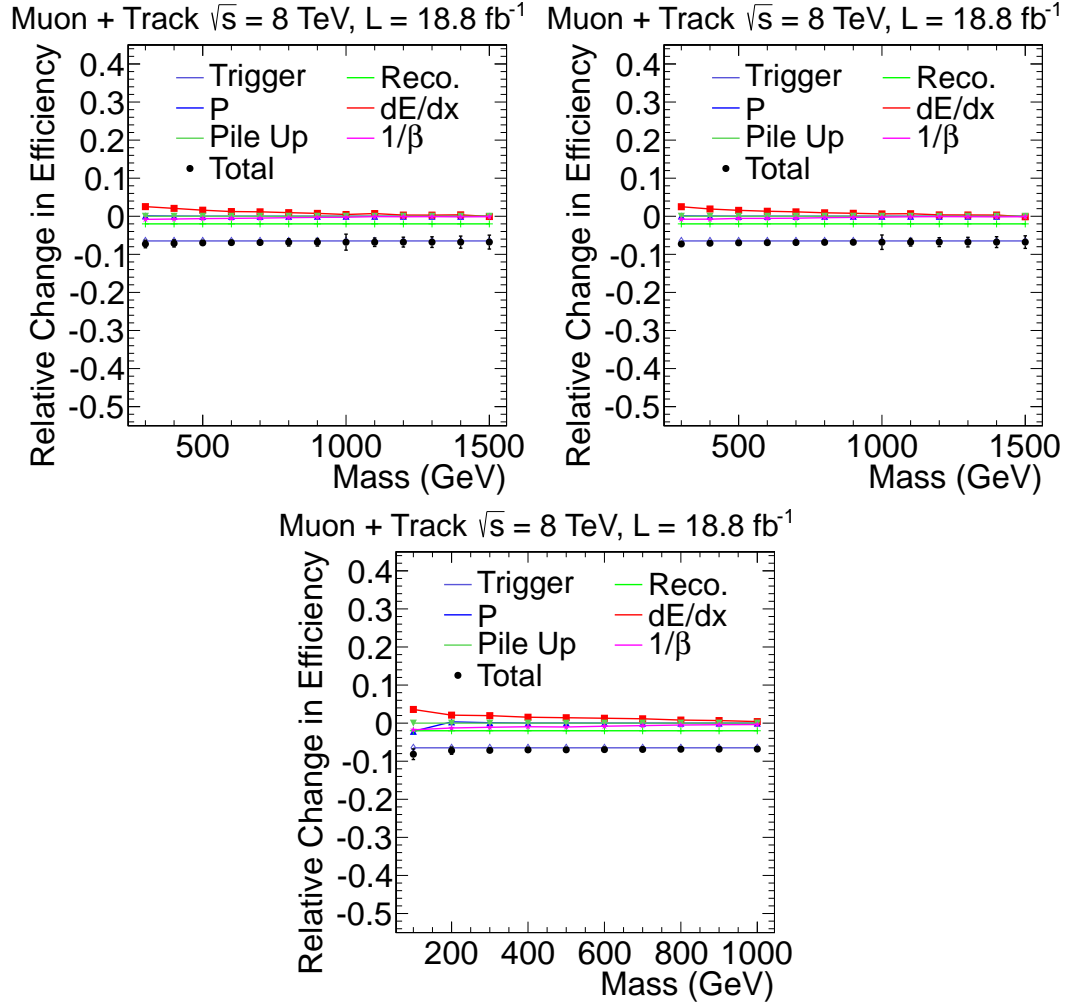
Figure 5.43: Relative efficiency change seen for the various sources of uncertainty for $R-hadron$ models in the $muon+track$ analysis. Top row: Gluino with $f = 0.5$ (left) and $f = 0.1$ (right). Bottom row: Stop
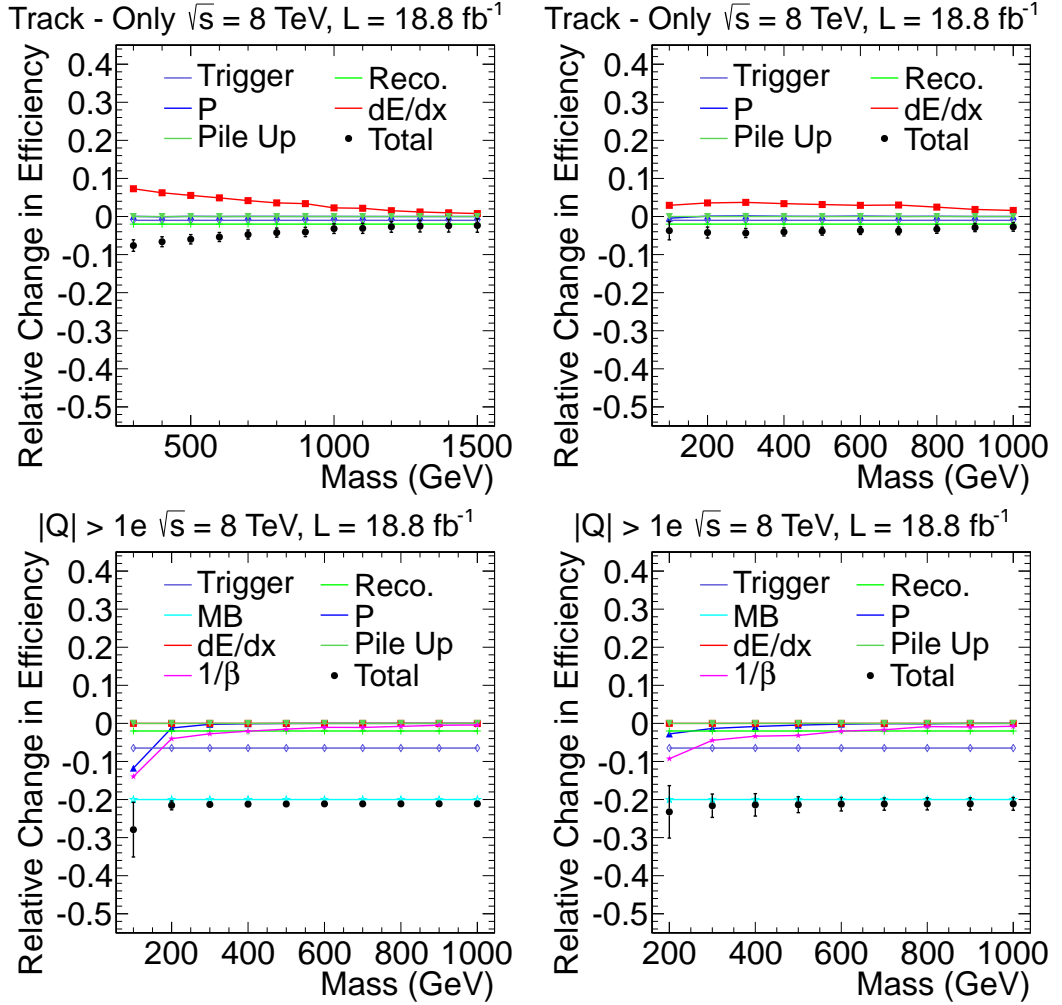
Figure 5.44: Relative signal efficiency change seen for the various sources of uncertainty. Top row: Charge suppressed Gluino with $f = 0.1$ (left) and charge suppressed stop (right) in the *track only* analysis. Bottom row: Q = 4e (left) and 7e (right) in the *multiple charge* analysis.
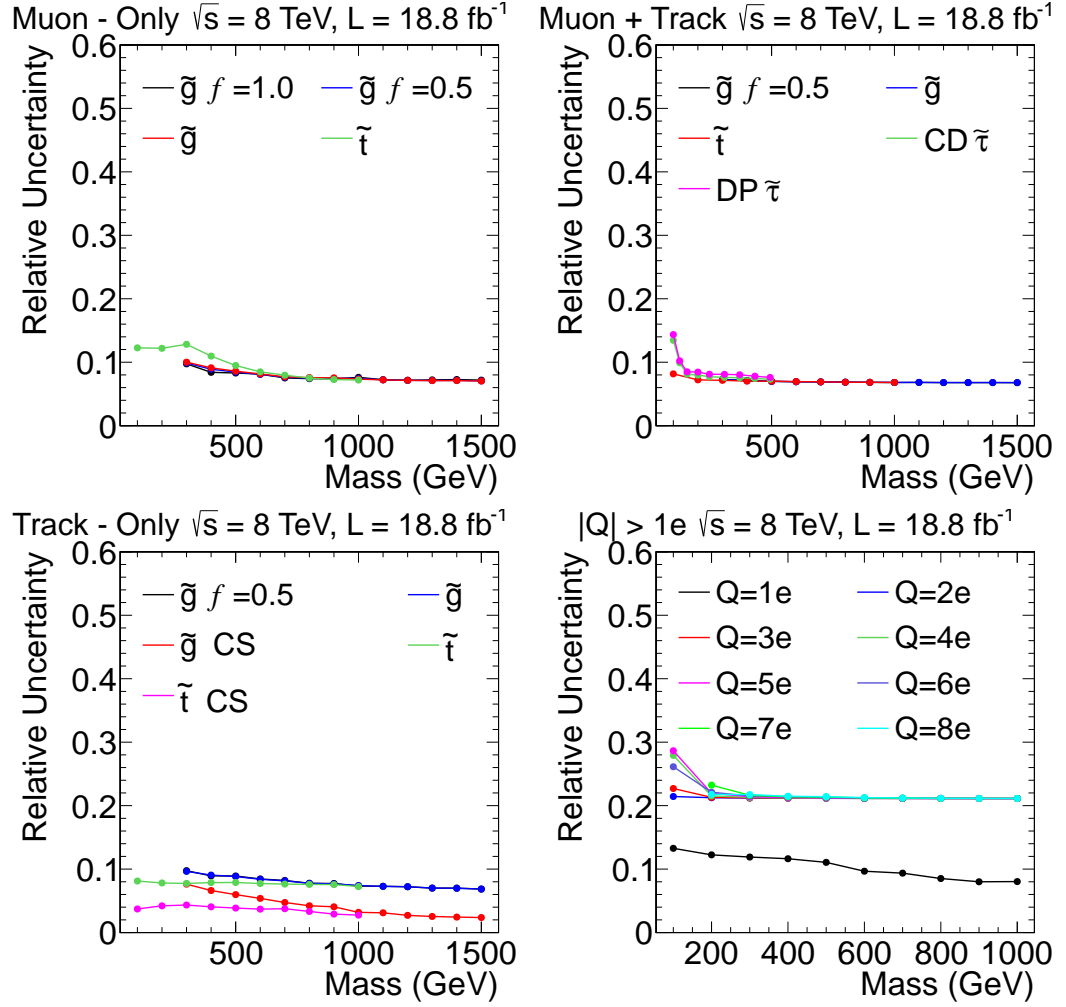
Figure 5.45: Total signal efficiency uncertainty for all considered models. Top: For the *muon only* (left) and *muon+track* (right) analyses. Bottom: For the *track only* (left) and *multiple charge* (right) analyses.
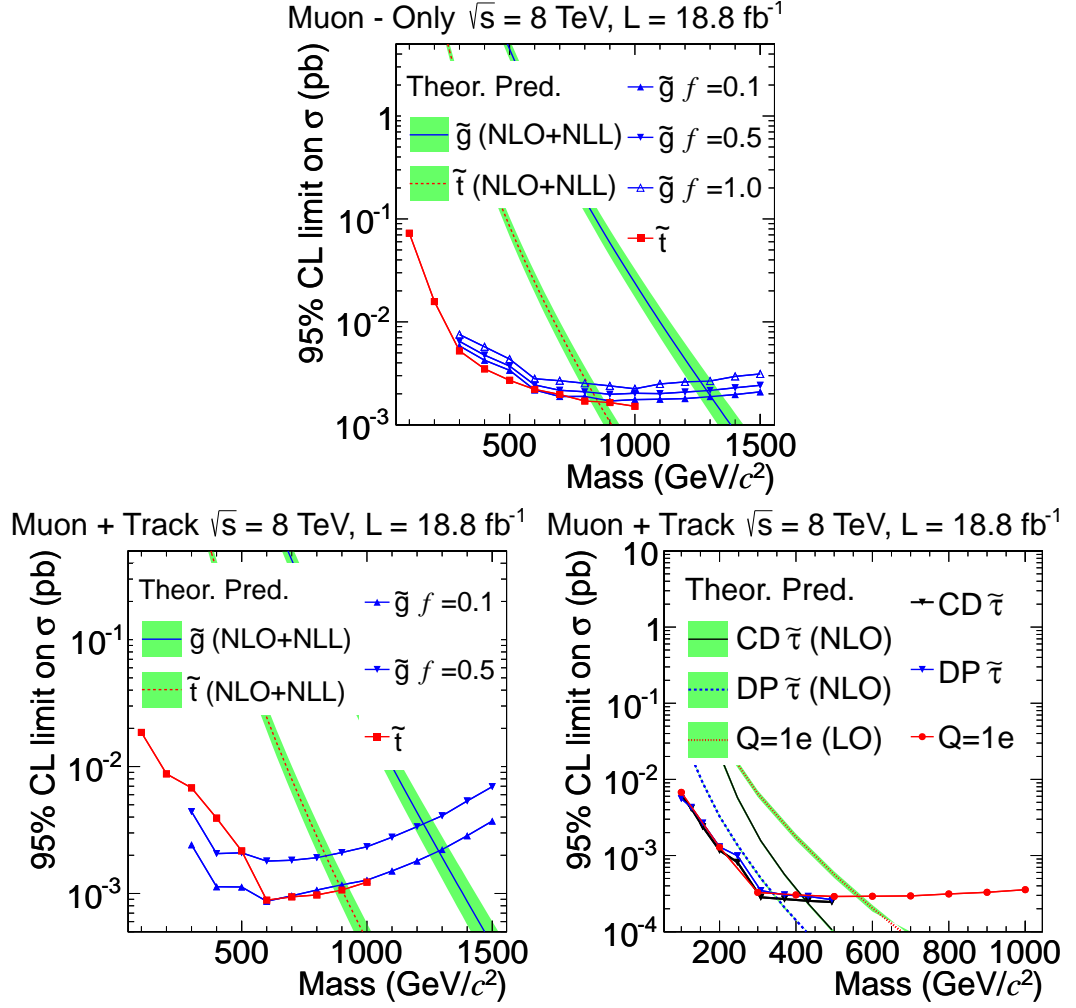
Figure 5.46: Cross-section limits obtained from 8 TeV data for all considered models in the *muon only* (top) and *muon+track* (bottom) analyses. The bottom left plot shows the limits for the *muon+track* analysis for hadron-like HSCP while the bottom right plot shows the limits for lepton-like HSCP.
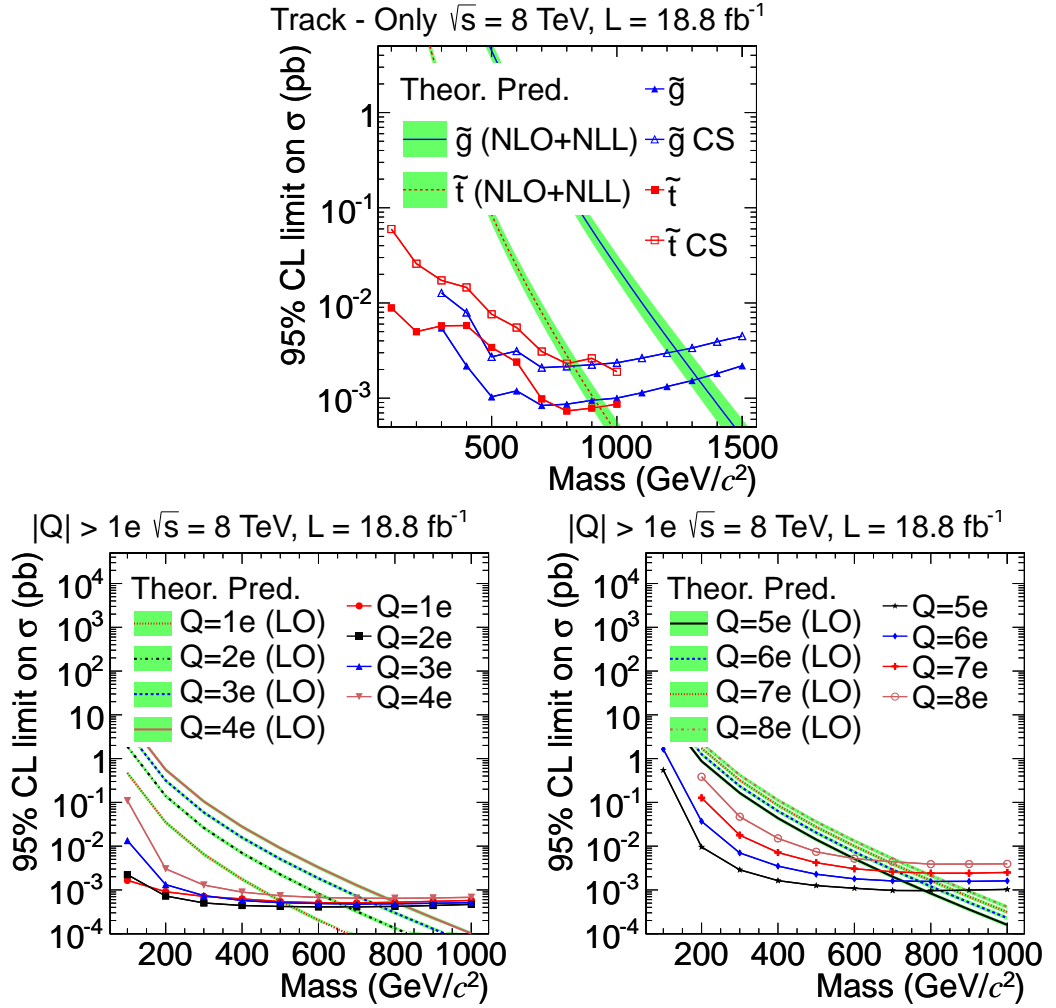
Figure 5.47: Cross-section limits obtained from 8 TeV data for all considered models in the *track only* (top) and *multiple charge* analyses. The bottom left plot shows the limits for the *multiple charge* analysis for charges <= 4e while the bottom right plot shows the limits for charges > 4e.
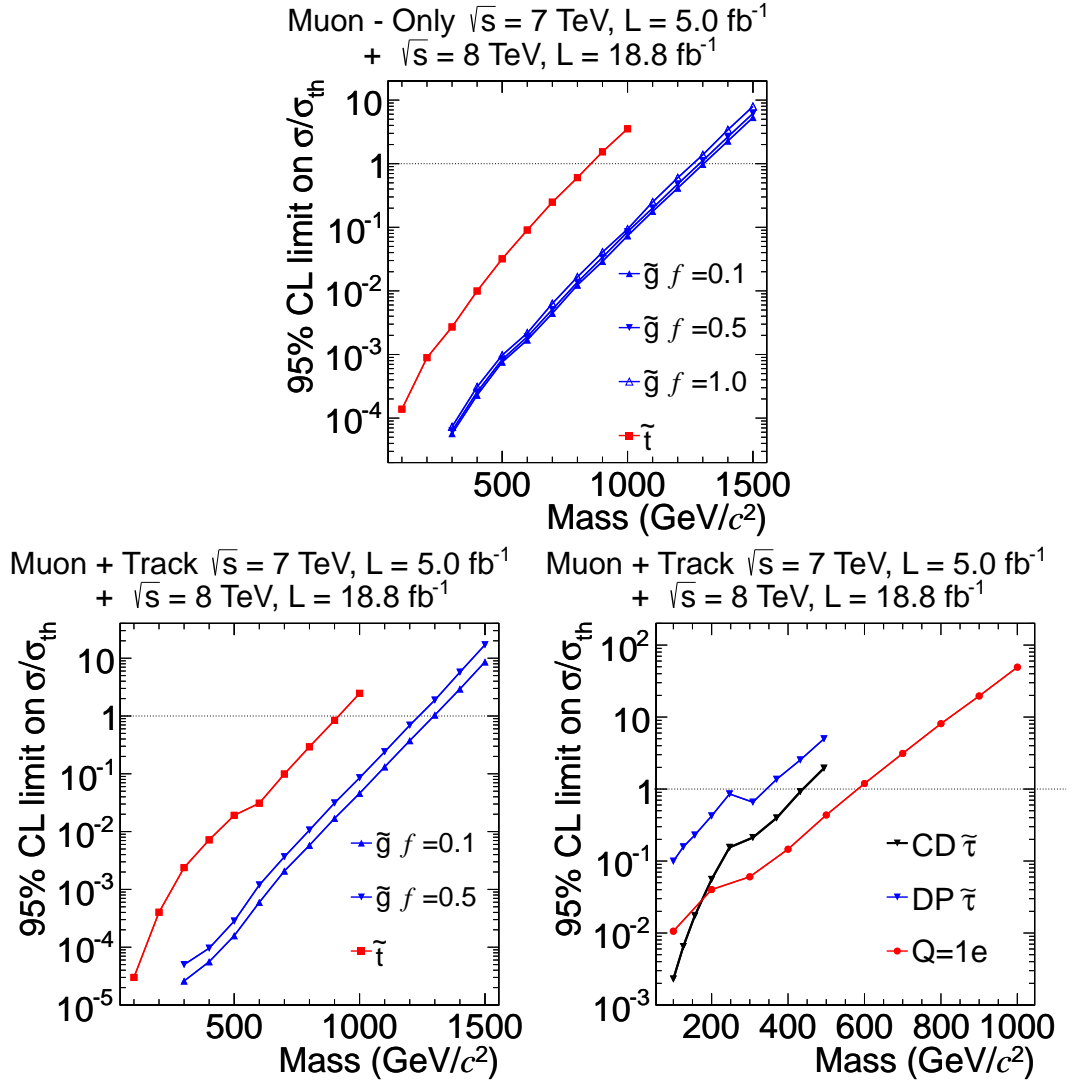
Figure 5.48: Limits on the relative signal strength, σ/σ_{th}, set by the *muon only* (top) and *muon+track* (bottom) analyses. The bottom left plot shows the limits for the *muon+track* analysis for hadron-like HSCP while the bottom right plot shows the limits for lepton-like HSCP.
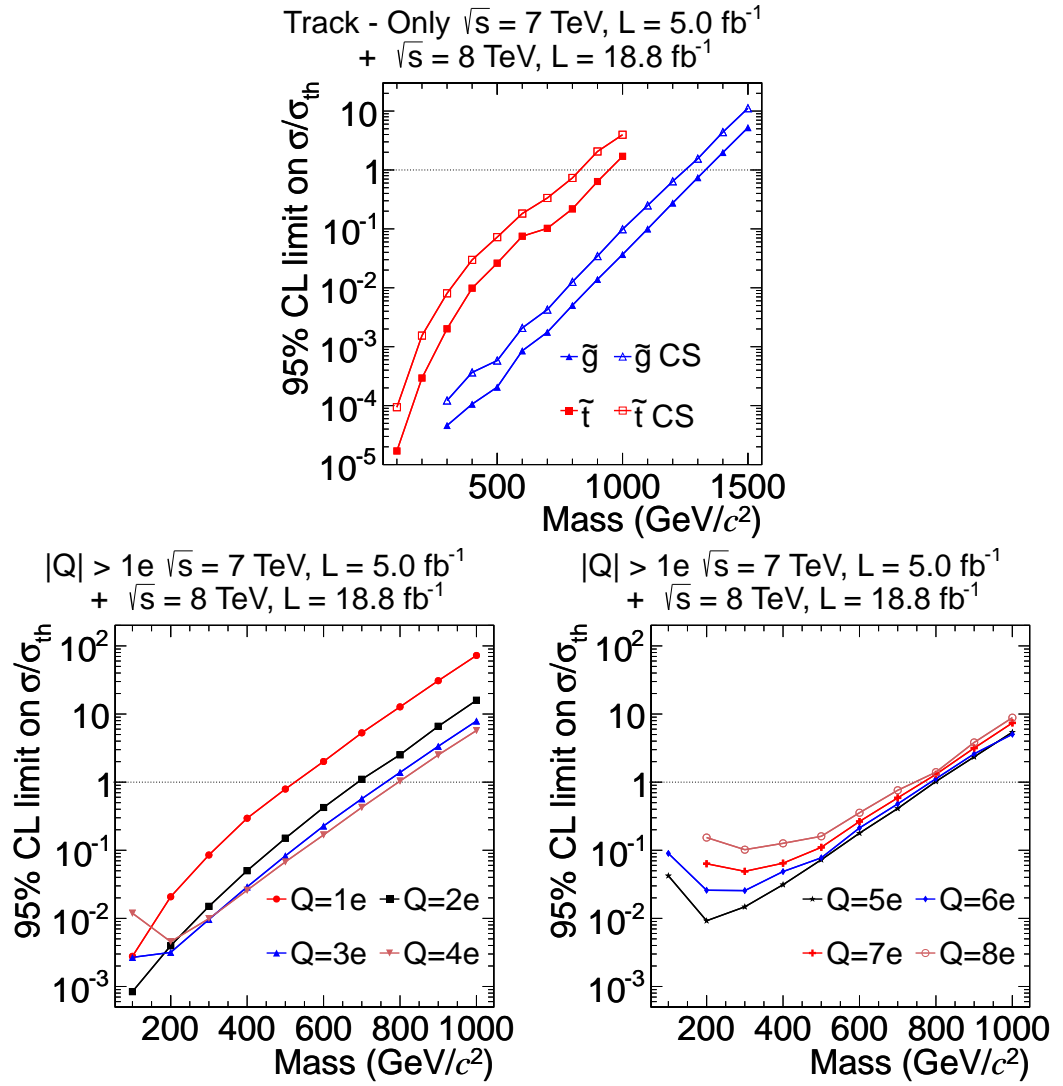
Figure 5.49: Limits on the relative signal strength, σ/σ_{th}, set by the *track only* (top) and *multiple charge* analyses. The bottom left plot shows the limits for the *multiple charge* analysis for charges $<= 4e$ while the bottom right plot shows the limits for charges $> 4e$.
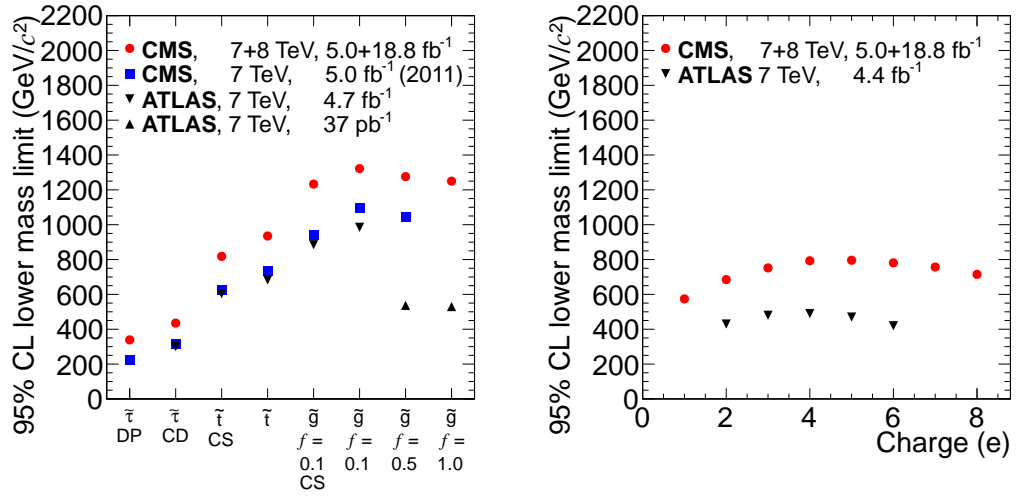
Figure 5.50: Lower mass limits at 95% CL on various SUSY models compared with previously published results [34, 33, 32, 37, 38, 31, 36]. The model type is defined by the x-axis (left). Mass limits for Drell–Yan like production of multiply charged particles versus electric charge (right).

CHAPTER 6

Conclusion

The measurement of the arrival time of hits in the CMS muon system is important for two reasons. The first is to quickly associate hits in the muon system with the appropriate LHC bunch crossing so that the data in the other subdetectors about this collision can be read out. A method was developed to measure the time offset of CSC chambers with respect to a determined optimal time that would give the best performance. The efficiency for chambers to correctly identify the right bunch crossing was brought to 99%, exceeding the design requirement of 92%. The second reason timing is important is to help identify different types of particles.

One of the particles timing can help identify is new heavy long-lived charged particles which would live long enough to interact directly with CMS and would be traveling at an appreciably slower speed than muons. Four searches were performed looking for particles of this type, each being sensitive to different signatures HSCP could have inside of CMS. The searches were performed by looking for tracks with some combination of high momentum, late arrival time in the muon system, or large ionization energy loss in the inner tracker. Backgrounds to the searches were muons form the collisions and in one of the searches muons from cosmic rays. The background in the signal region was predicted using control regions in data and the robustness of the prediction was checked by looking in the control region where particles would be traveling faster than the speed of light.

No excess above the expected background from SM processes was found in any of the four searches. Limits were placed on the production of long-lived charged particles created in many different theories, including versions of supersymmetry. These limits place important bounds on the theories of physics beyond the SM. While no discovery of new long-lived charged particles was found in the data searched there may be other signs of new physics present. Careful study of the recently discovered Higgs Boson-like particle is underway and many other searches are ongoing looking for the production of new particles. In addition, after a two year shutdown, the LHC will restart operations at a higher collision energy and rate which will allowing for probing the production of new physics at even smaller rates. Thus, a major discovery to reshape particle physics may be not far out of reach.

REFERENCES

[1] D. Griffiths. *Introduction to Elementary Particles*. Physics Textbook. Wiley, 2008.

[2] Lyndon Evans and Philip Bryant. Lhc machine. *Journal of Instrumentation*, 3(08):S08001, 2008.

[3] Serguei Chatrchyan et al. Observation of a new boson with mass near 125 GeV in pp collisions at sqrt(s) = 7 and 8 TeV. 2013.

[4] Georges Aad et al. Observation of a new particle in the search for the Standard Model Higgs boson with the ATLAS detector at the LHC. *Phys.Lett.*, B716:1–29, 2012.

[5] Stephen P. Martin. A Supersymmetry primer. 1997.

[6] Xerxes Tata. What is supersymmetry and how do we find it? 1997.

[7] Mark Srednicki. *Quantum Field Theory*. Cambridge University Press, 1 edition, February 2007.

[8] Serguei Chatrchyan et al. Observation of a new boson at a mass of 125 GeV with the CMS experiment at the LHC. *Phys.Lett.*, B716:30–61, 2012.

[9] M. Fairbairn, A.C. Kraan, D.A. Milstead, T. Sjostrand, Peter Z. Skands, et al. Stable massive particles at colliders. *Phys.Rept.*, 438:1–63, 2007.

[10] Rasmus Mackeprang and David Milstead. An Updated Description of Heavy-Hadron Interactions in GEANT-4. *Eur.Phys.J.*, C66:493–501, 2010.

[11] Aafke Christine Kraan. Interactions of heavy stable hadronizing particles. *Eur.Phys.J.*, C37:91–104, 2004.

[12] Rasmus Mackeprang and Andrea Rizzi. Interactions of Coloured Heavy Stable Particles in Matter. *Eur.Phys.J.*, C50:353–362, 2007.

[13] G.F. Giudice and R. Rattazzi. Theories with gauge mediated supersymmetry breaking. *Phys.Rept.*, 322:419–499, 1999.

[14] Paul Langacker and Gary Steigman. Requiem for an FCHAMP? Fractionally CHArged, Massive Particle. *Phys.Rev.*, D84:065040, 2011.

[15] J. Beringer et al. Review of Particle Physics (RPP). *Phys. Rev.*, D 86:010001, 2012.

[16] CMS Collaboration. CMS Luminosity — Public Results. `https://twiki.cern.ch/twiki/bin/view/CMSPublic/LumiPublicResults`. Accessed: 2013-05-16.

[17] S. Chatrchyan et al. The CMS experiment at the CERN LHC. *JINST*, 3:S08004, 2008.

[18] G. Bayatian et al. *CMS Physics: Technical Design Report Volume 1: Detector Performance and Software.* Technical Design Report CMS. CERN, Geneva, 2006. There is an error on cover due to a technical problem for some items.

[19] The CMS Collaboration. Performance of CMS muon reconstruction in pp collision events at $\sqrt{s} = 7$ TeV. *Journal of Instrumentation*, 7:2P, October 2012.

[20] D. Acosta et al. A 3-d track-finding processor for the cms level-1 muon trigger. *ArXiv Physics e-prints*, June 2003.

[21] A Rizzi et al. Search for heavy stable charged particles with 100 pb^{-1} and 1 fb^{-1} at cms experiment. 2007. CMS AN2007/049.

[22] R. Barate et al. Search for pair production of longlived heavy charged particles in e^+e^- annihilation. *Phys. Lett. B*, 405:379, 1997.

[23] P. Abreu et al. Search for heavy stable and longlived particles in e^+e^- collisions at $\sqrt{s} = 189$GeV. *Phys. Lett. B*, 478:65, 2000.

[24] P. Achard et al. Search for heavy neutral and charged leptons in e^+e^- annihilation at LEP. *Phys. Lett. B*, 517:75, 2001.

[25] G. Abbiendi et al. Search for stable and longlived massive charged particles in e^+e^- collisions at $\sqrt{s} = 130$GeV to 209GeV. *Phys. Lett. B*, 572:8, 2003.

[26] A. Aktas et al. Measurement of anti-deuteron photoproduction and a search for heavy stable charged particles at HERA. *Eur. Phys. J. C*, 36:413, 2004.

[27] V. M. Abazov et al. Search for long-lived charged massive particles with the D0 detector. *Phys. Rev. Lett.*, 102:161802, 2009.

[28] T. Aaltonen et al. Search for long-lived massive charged particles in 1.96TeV $\bar{p}p$ collisions. *Phys. Rev. Lett.*, 103:021802, 2009.

[29] V.M. Abazov et al. A search for charged massive long-lived particles. *Phys. Rev. Lett.*, 108:121802, 2012.

[30] Victor Mukhamedovich Abazov et al. Search for charged massive long-lived particles at $\sqrt{s}$=**1.96** TeV. *Phys. Rev. D*, 87:052011, 2013.

[31] Vardan Khachatryan et al. Search for heavy stable charged particles in pp collisions at $\sqrt{s} = 7$TeV. *JHEP*, 03:024, 2011.

[32] Georges Aad et al. Search for Massive Long-lived Highly Ionising Particles with the ATLAS Detector at the LHC. *Phys.Lett.*, B698:353–370, 2011.

[33] Georges Aad et al. Search for stable hadronising squarks and gluinos with the ATLAS experiment at the LHC. *Phys.Lett.*, B701:1–19, 2011.

[34] Georges Aad et al. Search for Heavy Long-Lived Charged Particles with the ATLAS detector in *pp* collisions at $\sqrt{s} = 7$ TeV. *Phys.Lett.*, B703:428–446, 2011.

[35] Serguei Chatrchyan et al. Search for fractionally charged particles in *pp* collisions at $\sqrt{s} = 7$TeV. 2012.

[36] Serguei Chatrchyan et al. Search for heavy long-lived charged particles in *pp* collisions at $\sqrt{s} = 7$ TeV. *Phys.Lett.*, B713:408–433, 2012.

[37] Georges Aad et al. Searches for heavy long-lived sleptons and R-Hadrons with the ATLAS detector in *pp* collisions at $\sqrt{s} = 7$ TeV. *Phys. Lett. B*, 720:277, 2013.

[38] Georges Aad et al. Search for long-lived, multi-charged particles in pp collisions at $\sqrt{s} = 7$TeV using the ATLAS detector. 2013.

[39] Carola F. Berger, James S. Gainer, JoAnne L. Hewett, and Thomas G. Rizzo. Supersymmetry Without Prejudice. *JHEP*, 02:023, 2009.

[40] Matthew W. Cahill-Rowley, JoAnne L. Hewett, Ahmed Ismail, and Thomas G. Rizzo. More energy, more searches, but the pMSSM lives on. 2012.

[41] Nima Arkani-Hamed and Savas Dimopoulos. Supersymmetric unification without low energy supersymmetry and signatures for fine-tuning at the LHC. *JHEP*, 0506:073, 2005.

[42] G.F. Giudice and A. Romanino. Split supersymmetry. *Nucl.Phys.*, B699:65–89, 2004.

[43] Torbjorn Sjostrand, Stephen Mrenna, and Peter Z. Skands. A Brief Introduction to PYTHIA 8.1. *Comput.Phys.Commun.*, 178:852–867, 2008.

[44] B.C. Allanach, M. Battaglia, G.A. Blair, Marcela S. Carena, A. De Roeck, et al. The Snowmass points and slopes: Benchmarks for SUSY searches. *Eur.Phys.J.*, C25:113–123, 2002.

[45] Frank E. Paige, Serban D. Protopopescu, Howard Baer, and Xerxes Tata. ISAJET 7.69: A Monte Carlo event generator for pp, anti-p p, and e+e- reactions. 2003.

[46] Torbjorn Sjostrand, Stephen Mrenna, and Peter Z. Skands. PYTHIA 6.4 Physics and Manual. *JHEP*, 0605:026, 2006.

[47] V. Khachatryan, A. M. Sirunyan, A. Tumasyan, W. Adam, T. Bergauer, M. Dragicevic, J. Erö, C. Fabjan, M. Friedl, R. Frühwirth, and et al. CMS tracking performance results from early LHC operation. *European Physical Journal C*, 70:1165–1192, December 2010.

[48] Jet Performance in pp Collisions at 7 TeV. 2010.

[49] Met performance in 8 tev data. Technical Report CMS-PAS-JME-12-002, CERN, Geneva, 2013.

[50] Thomas Wangler and KR Crandall. Beam halo in proton linac beams. In *Linac 2000 Conference Proceedings, Monterey California*, 2000.

[51] G Abbiendi et al. Muon reconstruction in the cms detector.

[52] Loic Quertenmont and Giacomo Bruno. *Search for Heavy Stable Charged Particles with the CMS detector at the LHC*. PhD thesis, Louvain U., 2010. presented Oct 2010.

[53] W. T. Eadie, D. Drijard, F. E. James, M. Roos, and B. Sadoulet. *Statistical methods in experimental physics*. North Holland, Amsterdam, 1971.

[54] F. James. *Statistical methods in experimental physics*. World Scientific, Singapore, 2006.

[55] A L Read. Modified frequentist analysis of search results (the cl_s method). (CERN-OPEN-2000-205), 2000.

[56] Glen Cowan, Kyle Cranmer, Eilam Gross, and Ofer Vitells. Asymptotic formulae for likelihood-based tests of new physics. *Eur.Phys.J.*, C71:1554, 2011.

[57] CMS Collaboration. Absolute calibration of the luminosity measurement at CMS: Winter 2012 update. CMS Physics Analysis Summary CMS-PAS-SMP-12-008, CMS, 2012.

[58] Measurement of tracking efficiency. Technical Report CMS-PAS-TRK-10-002, CERN, 2010. Geneva, 2010.

[59] CMS Collaboration. Precise mapping of the magnetic field in the CMS barrel yoke using cosmic rays. *Journal of Instrumentation*, 5:3021, March 2010.